

Summer 7-2017

Design of Variable Stiffness Composite Panels for Maximum Strength

Joel P. Hurley
Embry-Riddle Aeronautical University

Follow this and additional works at: <https://commons.erau.edu/edt>



Part of the [Structures and Materials Commons](#)

Scholarly Commons Citation

Hurley, Joel P., "Design of Variable Stiffness Composite Panels for Maximum Strength" (2017). *Doctoral Dissertations and Master's Theses*. 366.

<https://commons.erau.edu/edt/366>

This Thesis - Open Access is brought to you for free and open access by Scholarly Commons. It has been accepted for inclusion in Doctoral Dissertations and Master's Theses by an authorized administrator of Scholarly Commons. For more information, please contact commons@erau.edu.

DESIGN OF VARIABLE STIFFNESS COMPOSITE PANELS
FOR MAXIMUM STRENGTH

A Thesis

Submitted to the Faculty

of

Embry-Riddle Aeronautical University

by

Joel P. Hurley

In Partial Fulfillment of the

Requirements for the Degree

of

Master of Science in Aerospace Engineering

July 2017

Embry-Riddle Aeronautical University

Daytona Beach, Florida

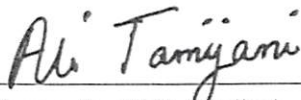
DESIGN OF VARIABLE STIFFNESS COMPOSITE PANELS
FOR MAXIMUM STRENGTH

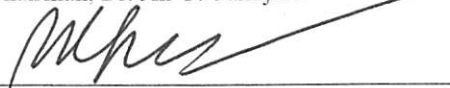
by


Joel P. Hurley

A Thesis prepared under the direction of the candidate's committee chairman, Dr. Ali Y. Tamijani, Department of Aerospace Engineering, and has been approved by the members of the thesis committee. It was submitted to the School of Graduate Studies and Research and was accepted in partial fulfillment of the requirements for the degree of Master of Science in Aerospace Engineering.


THESIS COMMITTEE



Chairman, Dr. Ali Y. Tamijani



Member, Dr. Marwan Al-Haik

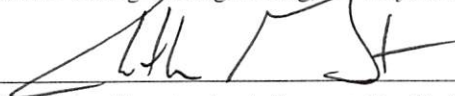

Member, Dr. Frank Radosta

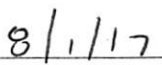

Aerospace Engineering Department Chair, Dr. Tasos Lyrintzis


Date


Dean of College of Engineering, Dr. Maj Mirmirani


Date


Vice Chancellor, Academic Support, Dr. Christopher Grant


Date

ACKNOWLEDGMENTS

I would like to thank my advisor, Dr. Ali Y. Tamijani, for his careful advice, guidance, and dedication throughout the past 18 months. I believe the work he has asked of me, though difficult and rigorous, has prepared me for the engineering challenges I face ahead. I hope to carry his lessons into my future career.

I must thank Prof. Glenn Greiner for all he has done for me (and for letting me steer his boat). Your friendship and advice throughout my time at Embry-Riddle is greatly appreciated.

I must acknowledge Ms. Pam Daniels and my friend Kimber McDaniel for their assistance editing this manuscript.

Finally, I would like to thank the colleagues from my research group for all their assistance in helping me reach my goals. I genuinely enjoyed working with you all and I am grateful to call you friends.

DEDICATION

To my parents and my brother, Sean. This manuscript is a product of your love and support.

TABLE OF CONTENTS

ACKNOWLEDGMENTS	iii
DEDICATION	iv
TABLE OF CONTENTS	v
LIST OF TABLES	vii
LIST OF FIGURES	viii
SYMBOLS	xi
ABBREVIATIONS	xiii
ABSTRACT	xiv
1. INTRODUCTION	1
1.1. Load Path Determination	1
1.2. Variable Stiffness Composites	4
1.3. 3D Printed Carbon Fiber Reinforced Polymer Composites	7
2. DETERMINATION OF STRUCTURAL LOAD PATHS	10
2.1. Methodology	10
2.2. Results	17
2.2.1. Plate under uniform pressure	17
2.2.2. Roof structure subjected to body load	20
2.2.3. Skin panel subjected to aerodynamic loading	23
2.2.4. Palazzetto dello Sport upper dome structure	27
2.3. Discussion	30
3. VARIABLE STIFFNESS COMPOSITES	30
3.1. Methodology	31
3.1.1. Strain method	32
3.1.2. Stress method	33
3.1.3. Energy method	34
3.1.4. Dominant Load path method	36
3.1.5. Weighted load path method	37
3.1.6. Fiber filtering	38
3.2. Results	39
3.2.1. Plate loaded in shear	39
3.2.2. Pin-loaded plate	48
3.2.3. Fighter wing under aerodynamic load	55
3.3. Discussion	62
4. CONSIDERATIONS FOR 3D PRINTED COMPOSITES	63

4.1.	Modeling	64
4.2.	Results	66
4.3.	Discussion	73
5.	CONCLUSION	75
6.	SUGGESTIONS FOR FUTURE WORK	77
	REFERENCES	78
	APPENDIX A: MICHELL TRUSS STRUCTURES	80
a.	Introduction.....	80
b.	Analytical solution to the ground structure.....	80
c.	Structural solution and sizing optimization	85

LIST OF TABLES

Table 3.1 Comparison of the overall compliance of the converged solutions.....	44
Table 3.2 Comparison of the overall compliance of each solution using fiber filtering. .	48
Table 3.3 Comparison of the overall compliance of the converged solutions.....	55
Table 3.4 Comparing the compliance between the initial and final design.	62
Table 4.1 Material data for the carbon fiber reinforced and nylon regions	67
Table 4.2 FEA failure stresses for the Type 4 model	69
Table 4.3. Relationship between number of concentric rings and total fiber volume fraction.	70
Table A1 Comparison of primal volumes for each layout order.	87

LIST OF FIGURES

Fig. 2.1 The change in ψ between two consecutive level sets is equivalent to the change in force between them.	13
Fig. 2.2 The projection of shell forces onto the x - y plane.....	15
Fig. 2.3 A plate subjected to a uniform pressure, pz , with (a) simply-supported edges and (b) clamped edges.	19
Fig. 2.4 The (a) potential function contours and (b) the iso-lines of total moment for a simply-supported plate under uniform pressure, pz	19
Fig. 2.5 The (a) potential function contours and (b) the iso-lines of total moment for a clamped plate under uniform pressure, pz	20
Fig. 2.6 The geometry of (a) a quarter-panel and (b) the full surface of a hyperbolic-paraboloid roof structure.....	21
Fig. 2.7 The projected shell forces from Eq. (23) showing (a) N_x , (b) N_y , and (c) N_{xy}	21
Fig. 2.8 Load paths in (a) x -direction and (b) y -direction for the membrane forces of a hyperbolic-paraboloid roof under its own weight.....	22
Fig. 2.9 Potential function contours for (a) x -direction and (b) y -direction membrane forces of a hyperbolic-paraboloid roof under its own weight.....	22
Fig. 2.10 Arbitrary wing skin panel subjected to aerodynamic loading.	24
Fig. 2.11 Demonstrating the decomposition of the stress field, (a) the total force, (b) the self-equilibrated component, (c) the irrotational component, (d) the verification that they add to zero.....	25
Fig. 2.12 Verifying that the self-equilibrated components are divergence-free and that irrotational components are curl-free for (a) x -direction, (b) y -direction, and (c) z -dir forces.....	26
Fig. 2.13 Load paths in (a) x -direction, (b) y -direction, and (c) z -direction for a skin panel subjected to aerodynamic loading.....	26
Fig. 2.14 Potential function contours in (a) x -direction, (b) y -direction, and (c) z -direction for a skin panel subjected to aerodynamic loading.....	27
Fig. 2.15 Side view of the Palazzetto dello Sport (Cutrì, 2015).	28
Fig. 2.16 Geometry of the dome of the Palazzetto dello Sport arena.	28
Fig. 2.17 Load paths in (a) x -direction, (b) y -direction, and (c) z -direction for the dome of the Palazzetto dello Sport arena under its own weight.	28
Fig. 2.18 Potential function contours in (a) x -direction, (b) y -direction, and (c) z -direction for the dome of the Palazzetto dello Sport arena under its own weight.	29
Fig. 3.1 Arbitrary domain, Ω , showing a design cell and its rotation angle, θe	31
Fig. 3.2 Rectangular plate subjected to a shear load.....	40

Fig. 3.3 A 20x40 element FEM mesh.	40
Fig. 3.4 Converged solution using the strain method.	41
Fig. 3.5 Converged solution using the stress method.	42
Fig. 3.6 Converged solution using the energy method.	42
Fig. 3.7 Converged solution using the dominant load path method.	43
Fig. 3.8 Converged solution using the weighted load path method.	43
Fig. 3.9 Convergence history of each method through 200 design iterations.	44
Fig. 3.10 Converged solution of the strain method using fiber filtering.	45
Fig. 3.11 Converged solution of the stress method using fiber filtering.	46
Fig. 3.12 Converged solution of the energy method using fiber filtering.	46
Fig. 3.13 Converged solution of the dominant load path method using fiber filtering.	46
Fig. 3.14 Converged solution of the weighted load path method using fiber filtering.	47
Fig. 3.15 Convergence history of the five methods using a filtering scheme.	48
Fig. 3.16 Pin-loaded plate subjected to a bearing load on the interior edge of the hole. ...	49
Fig. 3.17. FEM mesh consisting of 2,128 elements.	50
Fig. 3.18 Converged solution using the strain method.	51
Fig. 3.19 Converged solution using the stress method.	51
Fig. 3.20 Converged solution using the energy method.	51
Fig. 3.21 Converged solution using the dominant load path method.	52
Fig. 3.22 Converged solution using the weighted load path method.	52
Fig. 3.23 Stable solution using the strain method showing the fiber trajectories.	53
Fig. 3.24 Stable solution using the stress method showing the fiber trajectories.	53
Fig. 3.25 Stable solution using the dominant load path method showing the fiber trajectories.	53
Fig. 3.26 Convergence history of the five solution methods.	54
Fig. 3.27 Wing planform geometry and dimensions.	56
Fig. 3.28 Aerodynamic pressure distribution at $\alpha = 1$ deg and Mach 0.8.	57
Fig. 3.29 FEM mesh comprised of 2,194 elements.	58
Fig. 3.30 Initial fiber design showing elemental fiber angles (red) and load function contours (blue).	59
Fig. 3.31 Converged fiber design showing elemental fiber angles (red) and load function contours (blue).	60
Fig. 3.32 Convergence history of the solution method showing marginal stability after 10 iterations.	61

Fig. 4.1 Part printed at ASTM D638-14 Type 4 standard used for tensile testing. 63

Fig. 4.2 a) Geometry and fiber layout of an ASTM D638-14/Type 4 3D printed part, b) Finite element mesh using CQUAD4 shell elements, c) The regions depicted in red specify areas of the part with only nylon filler material. 65

Fig. 4.3 The fiber orientation angles mapped onto the centroids of each element. 66

Fig. 4.4 σ_1 normal stress [MPa] at failure load 68

Fig. 4.5 τ_{12} shear stress [MPa] at failure load 68

Fig. 4.6 Tsai-Wu failure indices for the Type 4 model at failure load. 68

Fig. 4.7 Fractured sample exhibiting matrix failure. Box contains longitudinal matrix crack and arrows point to crack initiation points. 69

Fig. 4.8 σ_1 normal stress [MPa] at failure load for with 6 concentric rings ($V_f = 0.3$) 70

Fig. 4.9 τ_{12} shear stress [MPa] at failure load for with 6 concentric rings ($V_f = 0.3$) 70

Fig. 4.10 Tsai-Wu failure indices for the Type 1 model at failure load. 70

Fig. 4.11 Tensile elastic modulus and strength of specimens as a function of total carbon fiber volume fraction..... 71

Fig. 4.12 Comparison of failure stresses at different fiber volume fraction, a) σ_1 [MPa] for $V_f = 0.3$, b) σ_1 [MPa] for $V_f = 0.15$, c) τ_{12} [MPa] for $V_f = 0.3$, d) τ_{12} [MPa] for $V_f = 0.15$ 72

Fig. 4.13 The relationship between the maximum stresses at failure and the total fiber volume fraction. 73

Fig. A1 Design domain of a cantilever structure. 82

Fig. A2 Ground structures for a cantilever beam generated analytically using Michell's optimality criteria..... 85

Fig. A3 FEA model of the ground structure (black) showing deflections (red) of the trusses after sizing optimization..... 86

Fig. A4 Results of the sizing optimization..... 87

SYMBOLS

α	energy factor or angle-of-attack
α, β	curvilinear coordinate system
A, B, D, E	solution coefficients for sensitivity equations
a, b	length and width dimensions or composite material parameters
C	unrotated stiffness matrix
\bar{C}	rotated stiffness matrix
C_p	pressure coefficient
c, d	composite material parameters
D	plate stiffness constant
ϵ_e	elemental strain vector
$\epsilon_x, \epsilon_y, \gamma_{xy}$	strains in the Cartesian coordinate frame
$\epsilon_1, \epsilon_2, \gamma_{12}$	strains in the material coordinate frame
E_1, E_2	elastic moduli in the material coordinate frame.
F_r	force in the radial direction
G_{12}	shear moduli in the material coordinate frame
g	gravitational acceleration
l	length of the truss member
M_x, M_y	moment resultants
M	total moment sum
m, n	Fourier series indices
n	unit vector normal to the boundary or number of elements
N_x, N_y, N_{xy}	in-plane force resultants
$\bar{N}_x, \bar{N}_y, \bar{N}_{xy}$	in-plane shell forces projected onto the xy -plane
N	axial force in the truss member
Ω	design domain or weight function
ν	Poisson's ratio
p_x, p_y, p_z	surface tractions in the Cartesian coordinate frame
$\bar{p}_x, \bar{p}_y, \bar{p}_z$	surface tractions projected onto the xy -plane
Φ	potential function associated with the body-force components
Φ_x, Φ_y, Φ_z	potential functions in the Cartesian coordinate frame
ϕ	shell rotation angle
Ψ	load function associated with the self-equilibrated components.
Ψ_x, Ψ_y, Ψ_z	load functions in the Cartesian coordinate frame
Q_x, Q_y	transverse shear force resultants
\bar{Q}_x, \bar{Q}_y	transverse shear force resultants projected onto the xy -plane
q_∞	free-stream
r	search radius
r_i	distance to query element
R^b	body-force components of the stress field
R^s	self-equillibrated components of the stress field

R_1, R_2, R_3	load vectors associated with the x, y, and z equilibrium equations
ρ	density
S	unrotated compliance matrix
\bar{S}	rotated compliance matrix
s_{01}, s_{02}, s_{03}	composite material constants
$\bar{\sigma}$	fictitious traction force
σ_e	elemental stress vector
$\sigma_1, \sigma_2, \tau_{12}$	stresses in the material coordinate frame
$\sigma_x, \sigma_y, \tau_{xy}$	stresses in the Cartesian coordinate frame
t	plate, shell or lamina thickness
T	transformation matrix
θ	fiber orientation angle or shell rotation angle
θ_e	elemental fiber orientation
u_e	elemental strain energy
V^*	primal volume
V	volume of the truss design
V_f	total fiber volume fraction of the structure
V_x, V_y	traction forces in the Cartesian coordinate frame.
w	plate transverse deflection
w_x, w_y	weight functions

ABBREVIATIONS

ABS	acrylonitrile butadiene styrene
AFP	automated fiber placement
ASEMlab	Advanced Structural and Energy Materials Laboratory
CFRP	carbon fiber reinforced polymer
ERAU	Embry-Riddle Aeronautical University
FEM	finite element method
NACA	National Advisory Committee for Aeronautics
QUAD4	four node quadrilateral shell element
RBE2	rigid body element
RTM	resin transfer molding
SAnD	Structural Analysis and Design Laboratory
UNM	University of New Mexico

ABSTRACT

Hurley, Joel P. MSAE, Embry-Riddle Aeronautical University, July 2017. Design of Variable Stiffness Composite Panels for Maximum Strength

The purpose of this research is to explore the design of variable stiffness composites and develop an automated framework to model, analyze and optimize these structures. Variable stiffness composites have been shown to exhibit increased strength and stiffness over traditional constant stiffness composites by tailoring fiber orientations for specific load conditions. This is achieved by allowing the fiber orientation to vary spatially across the design domain. Motivation for new design methods is driven by the recent advancements in composite additive manufacturing, such as automated fiber placement machines, which allow fiber reinforcements to be placed along prescribed trajectories during manufacturing. Through this research the problem of optimized orthotropic material orientation will be investigated. A new methodology is proposed that uses the concept of structural load flow to determine fiber trajectories. Fiber designs using the load path method are compared to the classical approaches such as the strain, stress, and energy methods. The load path function method is also expanded upon to solve the problem of non-homogenous equilibrium equations. This method allows load paths to be determined for more complicated loads such as aerodynamic pressures, thermal and inertial loads. Additionally, the design considerations for 3D printed composites are addressed. Experimental validation of the finite element codes used to model 3D printed composite structures is presented.

1. INTRODUCTION

Implementation of variable stiffness composites has been shown to increase the performance of structures subjected to a known load case. The purpose of this research is to explore methods for finding optimized fiber orientation using the concept of structural load paths. This work is organized into three topics which draw upon each other. The first topic on the load path determination expands previous theory to plate and shell bending and includes a method to address the presence of non-conservative body loads in equilibrium equations. The second topic investigates the design of optimized variable stiffness composites and compares classical methods with solutions found using the load path function method. The third and last section discusses the design considerations of 3D printed composite structures. A finite element framework to model additively manufactured composites with curvilinear (steered) fibers is presented along with experimental validation.

1.1. Load Path Determination

Understanding how load flows through a structure may provide valuable knowledge as to the performance and efficiency of the structure and could provide the engineer with an additional tool to measure the functionality of a design. Various proposed methods in literature have their own definitions and characterizations as to the exact definition of a “load path”. For the purpose of this research, load paths are defined as curves that bound regions of constant load flow.

Initial work on the theory of load paths sought to utilize major and minor principle stress angles as a means to describe the direction of load flow through the structure (Marhadi & Venkataraman, 2009). Principle stress angles are easily calculated

and can be readily found using standard finite element method (FEM) software.

However, load paths and principle stress angles vary in definitions. Firstly, principle stress angles describe the angle at which no shear exists on an element. For an area of the structure with high shear stresses, the difference between a vector tangent to the load path and the principle stress angle could be as much as 45 degrees (Waldman, Heller, Kaye, & Rose, 2002). Secondly, principle stress angles could not be used to describe a path of constant load flow because they only represent direction at localized points and give no information on the amount of load carried in a particular region.

Kelly et al. introduced load path pointing vectors in the dominant and complementary directions using stress resultants (1995). Load paths are defined as tubes of constant force bounded by contours with variable lateral spacing. In the case of the x-direction load paths, the equilibrium condition implies that the normal and shear stresses tangent to the boundary of the path do not contribute to the overall equilibrium in the x-direction. Using the Runge-Kutta method to determine the load path contours by solving an ODE using the traction vectors defined at nodal locations expanded on this method (D. W. Kelly, Reidsema, & Lee, 2011). Further work presented examples of the application of load paths to topology optimization in the initial design phase of various projects (D. Kelly, Reidsema, Bassandeh, Pearce, & Lee, 2011).

Takahashi presented a method to determine internal load transfer by finding the change of compliance energy inside a structure (Takahashi, 2001). The initial strain energy at each node is found using the displacement method. By sequentially constraining individual nodes then enforcing the same displacements that were found initially, new strain energies can be found at those specific locations. The change in

compliance energy at a point is the difference between the new strain energy and the original strain energy found at that location. The load path can be found by taking the gradient of the compliance energy scalar field then finding the resulting contour with the smallest gradient. Sakurai et al. expanded on the compliance energy method by introducing methods to reduce the computation time (Sakurai, Takahashi, Kawakami, & Abe, 2007).

Harasaki and Arora introduced the concept of load transfer and potential load transfer to determine load flow through a structure (Harasaki & Arora, 2001). For any system of connected elements subjected to applied loads, the load transfer through any element can be found. This is done by first finding the displacements and corresponding reaction forces for the structure. Then by setting the stiffness of the element in question to zero and applying the same displacements found initially, a new set of reaction forces can be found. By taking the difference in reaction forces the load transfer through the unstiffened element can be found. This process is repeated for each element until the load transfer in all the elements is found. Potential load transfer is a similar concept, except it is used to measure the effectiveness of applying additional stiffness to the structure.

Experimental tests have been undertaken that use load path visualization to map continuous fiber reinforcements onto composite laminates. Li et al. used this methodology to align individual fibers along the load path trajectories of a bolted composite joint (Li, Kelly, Crosky, Schoen, & Smollich, 2006). Experimental testing showed a 33% increase in ultimate failure strength and twofold increase in joint efficiency. Tosh and Kelly performed tests on open-hole and pin-loaded laminates manufactured with trajectorial fiber steering (Tosh & Kelly, 2000). Fibers were mapped

based on principle stress angles, load path trajectories and a hybrid method that combined both aforementioned methods. Using load path trajectories resulted in an increase in specific failure loads and outperformed the laminates mapped using principle stress angles.

In recent years, physical descriptions of load paths have been defined and used to synthesize optimal compliant mechanisms (Santer & Pellegrino, 2009). The load paths in compliant mechanisms are defined using geometric descriptions for the connectivity of the point of application and point of support. Optimization of the compliant mechanism uses binary variables to indicate the presence or absence of a load path. This method may have a limited range of applications due to the difficulties in presenting the load paths by connectivity for continuum structures (Venkataraman, Marhadi, & Haney, 2009).

The research introduced by Tamijani et al. uses the load path function method to determine load flow in plane elasticity (2016). The orthogonal load path functions are derived from 2D equilibrium equations. The Galerkin method is used to solve the equilibrium equations and load path functions are found from the resulting Galerkin linear system. The load paths can be visualized by taking contours of the load path functions.

1.2. Variable Stiffness Composites

The growth and proliferation of automated fiber placement (AFP) machines has generated a renewed interest into the problem of optimal fiber layout for composite structures. AFP machines can place composite tapes or tows along prescribed trajectories which introduces the possibility of designing structures with varying fiber angles.

Incorporating steered fibers into laminates has been shown to increase stiffness, strength,

and buckling stability for specific load cases (Wu, 2008). There is great emphasis on methods to determine optimized fiber paths to take advantage of this technology.

A number of methods have been proposed to solve the problem of optimized orientation for orthotropic materials when using compliance as the objective function. Focus will be made on the classical methods, such as the strain, stress, and energy methods. These methods use FEM to discretize the structure into individual design cells and the optimal orientation angle is determined by finding the angle which produces the lowest strain energy for each element.

The strain based method uses the existing strain field to determine the orientation in which the strain energy is minimized (Pedersen, 1989). The stress based method uses a similar approach, except with the stress field (Diaz & Bendsøe, 1992). These methods tend to converge to the orientations of the dominant principle strain and stress, respectively, and both have been shown to produce acceptable results. Both methods assume the orientation angle has no effect on the resultant stress and strain field which could potentially lead to two different orientations representing the global minima (Gea & Luo, 2004). An energy based method was offered as an implicit approximation to model the effect of how varying the orientation angle affects the existing stress and strain field (Luo & Gea, 1998). The energy method has been shown to produce better results than the strain and stress based methods.

However, these methods have drawbacks. The compliance is minimized on each element not on the whole structure; this leads to local convergence, not global convergence. There is no way to take into account how varying the angle on one element affects the compliance of adjacent elements or the structure as a whole. This limits how

much an element can change its orientation during each iteration for fear of the solution becoming unstable. Second, the converged solution may not be manufacturable because fibers may be discontinuous between elements, or the curvature of the fiber paths may exceed the limits of what the AFP machine can create (Setoodeh, Abdalla, IJsselmuiden, & Gürdal, 2009). Frameworks have been proposed to filter the fiber angles by averaging fiber orientations in subdomains, but this approach is associated with a drop in compliance (Kiyono, Silva, & Reddy, 2017). The converged solutions for the strain, stress, and energy method are sensitive to the initial design. The possibility of entire structure converging to a local minima increases if a poor initial design is selected, or if the change in orientation angle between two iterations is too large (Thomsen, 1991).

Recently, other methods have been proposed as well. Brampton et al. introduced a level set method to determine optimized fiber lay outs (Brampton, Wu, & Kim, 2015). Implementation of the level set method is advantageous because it can generate constant level set contours of continuous and equally spaced fiber trajectories. This helps address the concerns with implementing manufacturing constraints into orthotropic optimization schemes. Legrand et al. used a genetic algorithm framework in conjunction with FEM to determine optimum orientation of material by using the primary material axis of each element as the design variable (Legrand, Kelly, Crosky, & Crépin, 2006). This method was determined to be computationally intensive and was improved by Bardy et al. (2012) by adjusting the genetic algorithm parameters and by replacing the stress-based fitness criterion with a strain-based criterion.

1.3. 3D Printed Carbon Fiber Reinforced Polymer Composites

The structural advantages of using carbon fiber reinforced polymers (CFRP) is the primary reason for their increased usage in aerospace and performance applications (Park, Choi, & Lee, 1995). Many manufacturing methods exist for producing CFRP parts. The method chosen can be based off of cost, final quality of the part, production run, and size of the structure (Ning, Cong, Qiu, Wei, & Wang, 2015). The open layup method, where the resin is applied to dry fibers in a mold, is a low-cost and low-tech fabrication practice for small production runs but generally leads to poorer structural properties. Pre-preg fabrics, where the optimal resin content is preimpregnated into the fabric, is cured under heat and pressure using either a vacuum bag/oven or autoclave. The structural properties of pre-preg composites are superior, but are labor intensive, produce excess waste, and lead to high cost. Closed mold methods, like injection, infusion, and resin transfer molding (RTM), are appropriate for large production runs and lead to very consistent parts (Mazumdar, 2001). Automated fiber placement (AFP) machines have been used for open mold applications where specific fiber placement is desired.

Recently, a new class of CFRP 3D printers has entered in the market. These printers utilize a thermoplastic, normally nylon, which is reinforced with carbon fiber tows. One of the most common CFRP 3D printers is the MarkForged desktop printer which was commercialized in 2015. The printer builds composites using a layering scheme, starting with the bottom layer and progressing building to the top. From a performance standpoint, the printer can produce parts that fall between metals and traditional polymers, and when divided by weight, are comparable to 3D printed metals. The printer uses dual nozzles to print nylon and carbon reinforcement simultaneously. A

layer of nylon matrix is placed on all the exterior edges of the part. These exterior layers are called the floor, wall, and ceiling layers. This ensures the carbon reinforcement is completely encased inside the nylon matrix. The MarkForged software suite allows only limited design when determining the fiber orientation inside the printed part. The most common design method is the automatic concentric fill option, which places fibers concentrically around the periphery of the part. For areas where the software cannot find a solution for fiber placement, pure nylon material can be placed instead. The biggest drawback from a design standpoint is that the software does not allow full customization of fiber orientation.

There are structural limitations to 3D printing technology. Most 3D printers, regardless of material, produce structures with anisotropy and contain thermal residual stresses due to the layered buildup of the part. The concerns with material anisotropy increase when continuous carbon tows are introduced into the structure. Other mechanical factors that contribute to the performance of 3D printed composites include the distribution of continuous fiber within the thermoplastic matrix, consistency of fiber volume fraction, and the chemical cohesion between the nylon matrix and carbon fiber. Part geometry and fiber orientation angle heavily influence the structural properties and must be taken into consideration during design.

In this research, FEM is utilized to predict the failure load and determine the mode of failure of 3D printed continuous CFRPs. To account for the orientation of the fibers, each element was given its own independent material property that corresponds to the local fiber orientation at the element position. The innovative variable orientation continuous fiber design requires the construction of hundreds to thousands of elements

with various material properties, which is not practical unless an automated modeling process is applied. Thus, an automated modeling framework is developed using an object-oriented script written in Matlab/Python that interfaces MSC.PATRAN and NASTRAN to model a 3D printed continuous CFRP and perform finite element analysis and return the weight, displacements, stresses, and local failure.

2. DETERMINATION OF STRUCTURAL LOAD PATHS

In this section, the load path function method will be extended to include plate and shell structures subjected to out-of-plane loads and non-conservative body loads. A concept will be introduced to decompose the stress field into a self-equilibrated component and an auxiliary body-force component. The purpose of this research is to use the contours of the load path function, which represent regions of constant load flow, as trajectories for fiber steered composites. The methodology to determine the load path function will be presented followed by a set of examples showing possible applications.

2.1. Methodology

The load path function method has the potential to be a powerful tool for the design engineer and could be used as a basis for topology optimization and fiber placement. Previous research on the load function formulation assumed two-dimensional structures loaded in a state of plane stress and was derived from the equilibrium equations in terms of stresses. The stresses were written in terms of the load functions and the load flow was calculated using the load function contours. The load functions were defined using Gurtin's representation. However, in several industrial applications the loads are out-of-plane, which creates varying stresses through the thickness of the structure due to bending moments. A problem is raised; if the stress varies with thickness so would the load paths, i.e. multiple load paths through the thickness would exist. Therefore, it would be challenging to utilize the Gurtin's decomposition directly to thin-walled structures. This problem is remedied by writing the equilibrium equations based on the stress resultant equilibrium equations, introduced in Eq.(1).

$$\begin{aligned}
\frac{\partial N_x}{\partial x} + \frac{\partial N_{xy}}{\partial y} + p_x &= 0 \\
\frac{\partial N_{xy}}{\partial x} + \frac{\partial N_y}{\partial y} + p_y &= 0 \\
\frac{\partial Q_x}{\partial x} + \frac{\partial Q_y}{\partial y} + p_z &= 0
\end{aligned} \tag{1}$$

Next, the load field with respect to a rectangular frame is defined as,

$$\begin{aligned}
R_1 &= N_x i + N_{xy} j \\
R_2 &= N_{xy} i + N_y j \\
R_3 &= Q_x i + Q_y j
\end{aligned} \tag{2}$$

Using this definition, the equilibrium equations can be written as,

$$\nabla \cdot R + p = 0 \tag{3}$$

where $R = [R_1 \ R_2 \ R_3]$, and $p = [p_x \ p_y \ p_z]$. The load vector field is decomposed into divergence-free and curl-free components using the Helmholtz-Hodge decomposition,

$$R = \nabla \Phi + \nabla \times \psi \tag{4}$$

In Eq.(4) the first component ($\nabla \Phi$) is the irrotational component (R^b), and the second component ($\nabla \times \psi$) is self-equilibrated or solenoidal component (R^s). The solenoidal vector field admits a load function ($\psi = [\psi_x \ \psi_y \ \psi_z]$) and accompanying load paths. The changes in ψ between their two constant paths equals to the constant load flow of the totally self-equilibrated stress resultants ΔR^s that is transferred between those two paths. Using the Helmholtz-Hodge decomposition first the divergence-free component (R^s) is solved for the given boundary conditions and then the curl-free component is determined as the residual ($R^b = R - R^s$). Given a stress resultant field, Eq.(4) can be

written as,

$$\nabla \times R = \nabla(\nabla \cdot \psi) - \Delta \psi \quad (5)$$

By using the weighted residual method, Eq.(5) can be written as,

$$-\int_{\Omega} \Delta \psi v d\Omega = \int_{\Omega} \nabla \times R v d\Omega \quad (6)$$

where v is the weight function, and the boundary condition associated with Eq.(6) is,

$$\frac{\partial \psi}{\partial n} = -R \times n \quad (7)$$

Using the boundary conditions, and integration by parts, Eq.(6) can be written as,

$$\int_{\Omega} \nabla \psi \nabla v d\Omega = \int_{\Omega} R \nabla \times v d\Omega \quad (8)$$

The field lines of solenoidal components (R^s) are the level sets of ψ . After obtaining ψ , then solenoidal components can be written as,

$$R^s = \nabla \times \psi \quad (9)$$

by using the irrotational components (R^b), Φ can be found,

$$\nabla \Phi = R^b = R - R^s \quad (10)$$

The integration of total differential of each load function, *e.g.* ψ_x , between two consecutive paths (paths 1 and 2) give,

$$\Delta \Psi_x = \int_1^2 \left(\frac{\partial \Psi_x}{\partial x} dx + \frac{\partial \Psi_x}{\partial y} dy \right) = \int_1^2 (-N_{xy}^s dx + N_x^s dy) = \Delta F_x^s \quad (11)$$

If the differential of load function is evaluated on its constant lines, then $\Delta F_x^s = 0$, which means the solenoidal component of a load vector field in a Helmholtz-Hodge representation does not pass through the level sets of load function (Fig. 2.1).

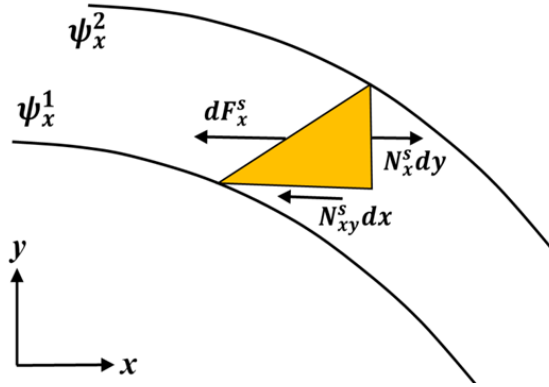


Fig. 2.1 The change in ψ between two consecutive level sets is equivalent to the change in force between them.

Next, this theory is extended to 3D thin-shell structures, such as the wing or fuselage skin of an aircraft, where the normal stress through the thickness is negligible. The goal is to find a function, ψ , that represents a constant flow of in-plane and transverse load from application to support. For general shell structures, where the shell mid-surface is $z = f(x, y)$, the method to find load function follows the presented load function procedure. In order to satisfy the equilibrium in the x and y directions, first the resultant loads per unit length (i.e. $N_{xy}, N_x, N_y, Q_x, Q_y$) and applied tractions (p_x, p_y, p_z) must be projected to the x - y plane (i.e. $\bar{N}_{xy}, \bar{N}_x, \bar{N}_y, \bar{Q}_x, \bar{Q}_y, \bar{p}_x, \bar{p}_y, \bar{p}_z$), as shown in Fig. 2.2. For a general shell of form $z = f(x, y)$, the angles of θ and Φ can be written as follows,

$$\tan \phi = \frac{\partial z}{\partial x}, \quad \text{and} \quad \tan \theta = \frac{\partial z}{\partial y} \quad (12)$$

Next, the projected forces on x - y plane are found,

$$\begin{aligned} \bar{N}_{xy} &= (N_{xy} \cos \theta - Q_x \sin \theta \cos \phi) / \cos \theta \\ \bar{N}_{yx} &= (N_{yx} \cos \phi - Q_y \sin \phi \cos \theta) / \cos \phi \\ \bar{N}_x &= (N_x \cos \phi - Q_x \sin \phi \cos \theta) / \cos \theta \\ \bar{N}_y &= (N_y \cos \theta - Q_y \sin \theta \cos \phi) / \cos \phi \\ \bar{Q}_x &= (Q_x \cos \phi \cos \theta + N_x \sin \phi + N_{yx} \sin \theta) / \cos \theta \\ \bar{Q}_y &= (Q_y \cos \phi \cos \theta + N_y \sin \theta + N_{xy} \sin \phi) / \cos \phi \end{aligned} \quad (13)$$

The equilibrium equations based on the projected forces on the x - y plane are,

$$\begin{aligned} \frac{\partial \bar{N}_x}{\partial x} + \frac{\partial \bar{N}_{xy}}{\partial y} + \bar{p}_x &= 0 \\ \frac{\partial \bar{N}_{yx}}{\partial x} + \frac{\partial \bar{N}_y}{\partial y} + \bar{p}_y &= 0 \\ \frac{\partial \bar{Q}_x}{\partial x} + \frac{\partial \bar{Q}_y}{\partial y} + \bar{p}_z &= 0 \end{aligned} \quad (14)$$

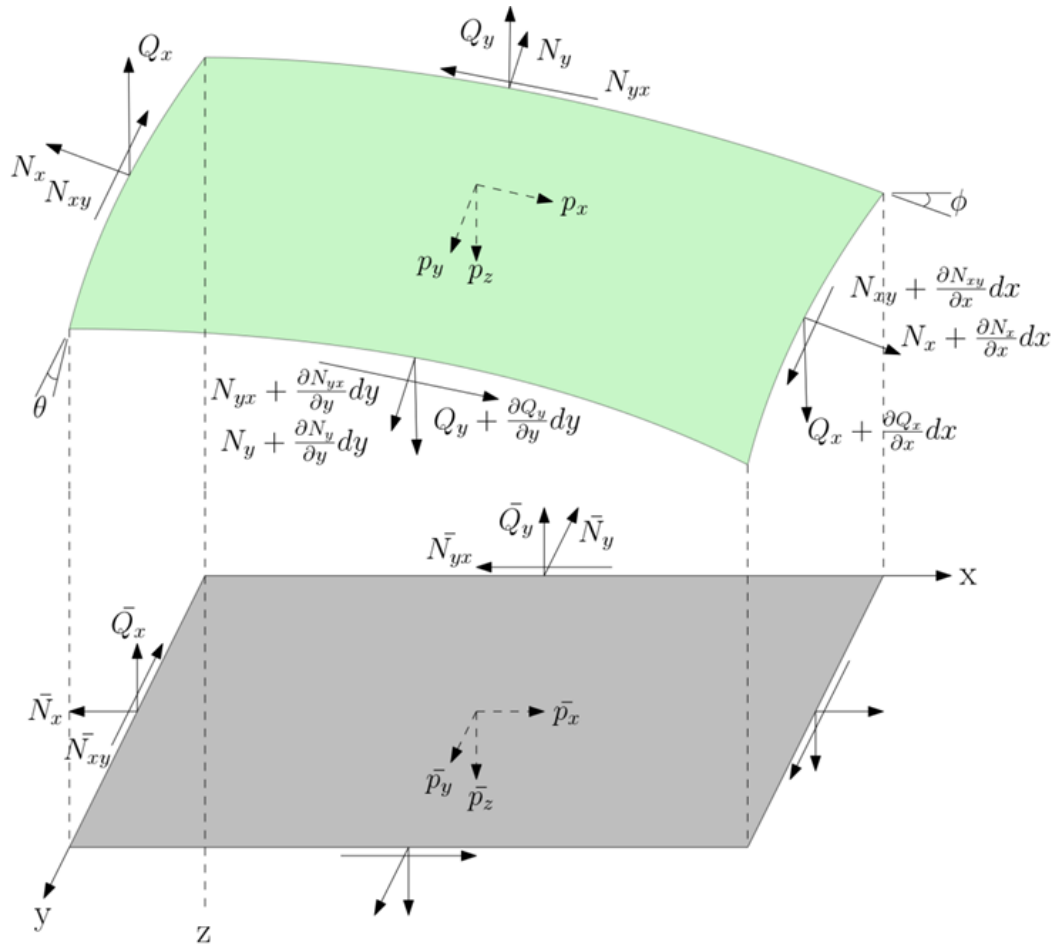


Fig. 2.2 The projection of shell forces onto the x - y plane.

By using the projected forces in Eq.(13), the load field can be defined as

$$\begin{aligned}
 R_1 &= \bar{N}_x i + \bar{N}_{xy} j \\
 R_2 &= \bar{N}_{xy} i + \bar{N}_y j \\
 R_3 &= \bar{Q}_x i + \bar{Q}_y j
 \end{aligned} \tag{15}$$

Then, similar to Eq.(4), the irrotational and solenoidal components as well as load function can be obtained. For the special case of a flat plate, where the surface $f(x, y) = 0$, the shear force field $(Q_x i + Q_y j)$ decomposed as,

$$\vec{Q} = \nabla \cdot \Phi_z + \nabla \times \Psi_z \tag{16}$$

By comparing Eq.(4), the shear force components can be written as

$$\begin{aligned} Q_x &= \left(\frac{\partial \Phi_z}{\partial x} + \frac{\partial \Psi_z}{\partial y} \right) \\ Q_y &= \left(\frac{\partial \Phi_z}{\partial y} - \frac{\partial \Psi_z}{\partial x} \right) \end{aligned} \quad (17)$$

When Eq.(17) is inserted into the equilibrium equation Eq.(1), the following expression is yielded,

$$\frac{\partial^2 \Phi_z}{\partial x^2} + \frac{\partial^2 \Phi_z}{\partial y^2} = -p_z \quad (18)$$

It can be seen that above equation is similar to the plate moment equilibrium equation

$$\frac{\partial^2 M}{\partial x^2} + \frac{\partial^2 M}{\partial y^2} = -p_z, \quad \text{where } M = \frac{M_x + M_y}{1 + \nu} \quad (19)$$

By comparing Eqs. (18) and (19) it can be shown that the potential function, Φ_z , is mathematically equivalent to the moment. Therefore, the values of M_x and M_y can be used as boundary conditions for solving Eq.(18). In this situation, the contours of Φ_z are similar to the iso-lines of moment.

2.2. Results

A series of examples are presented to demonstrate the load path methodology including the decomposition procedure to solve for the load paths of the self-equilibrated force field. The first two examples use analytical force fields for classical structures. The last two examples use force fields found using FEM.

2.2.1. Plate under uniform pressure

Assume two isotropic plates subjected to a uniform pressure, p_z , one with simply-supported edges and the other with clamped edges (Fig. 2.3). Edges lengths a and b are set equal to 1. By assuming Kirchoff-Love plate theory, we can utilize Navier's plate solution for the lateral deflection, w , of the simply-supported plate as,

$$w = \frac{16p_z}{D\pi^6} \sum_{n=1,3,5}^{\infty} \sum_{m=1,3,5}^{\infty} \frac{\sin\left(\frac{m\pi x}{a}\right) \sin\left(\frac{n\pi y}{b}\right)}{mn \left(\left(\frac{m}{a}\right)^2 + \left(\frac{n}{b}\right)^2\right)^2} \quad (20)$$

Where D , the plate stiffness constant, is nondimensionalized to a value of 1. The solution terms are summed up to $m, n = 101$ terms. The transverse shear resultants can be found as,

$$\begin{aligned} Q_x &= -D \frac{\partial w}{\partial x} \left(\frac{\partial^2 w}{\partial x^2} + \frac{\partial^2 w}{\partial y^2} \right) \\ &= \frac{16p_z}{\pi^4} \sum_{n=1,3,5}^{\infty} \sum_{m=1,3,5}^{\infty} \frac{\left(\frac{m\pi}{a}\right) \cos\left(\frac{m\pi x}{a}\right) \sin\left(\frac{n\pi y}{b}\right)}{mn \left(\left(\frac{m}{a}\right)^2 + \left(\frac{n}{b}\right)^2\right)} \\ Q_y &= -D \frac{\partial w}{\partial y} \left(\frac{\partial^2 w}{\partial x^2} + \frac{\partial^2 w}{\partial y^2} \right) \\ &= \frac{16p_z}{\pi^4} \sum_{n=1,3,5}^{\infty} \sum_{m=1,3,5}^{\infty} \frac{\left(\frac{n\pi}{b}\right) \sin\left(\frac{m\pi x}{a}\right) \cos\left(\frac{n\pi y}{b}\right)}{mn \left(\left(\frac{m}{a}\right)^2 + \left(\frac{n}{b}\right)^2\right)} \end{aligned} \quad (21)$$

Additionally, the total moment sum, M , can be found as,

$$\begin{aligned}
 M &= \frac{M_x + M_y}{1 + \nu} = -D \left(\frac{\partial^2 w}{\partial x^2} + \frac{\partial^2 w}{\partial y^2} \right) \\
 &= \frac{16p_z}{\pi^4} \sum_{n=1,3,5}^{\infty} \sum_{m=1,3,5}^{\infty} \frac{\sin\left(\frac{m\pi x}{a}\right) \sin\left(\frac{n\pi y}{b}\right)}{mn \left(\left(\frac{m}{a}\right)^2 + \left(\frac{n}{b}\right)^2 \right)} \quad (22)
 \end{aligned}$$

By using the transverse shear resultants of Eq.(21), we can see that $\nabla \times \mathbf{R}_3 = 0$, which means the load function Ψ_z is also zero. It can then be concluded that the stress field, \mathbf{R}_3 , only has an irrotational component, \mathbf{R}^b . The potential function can be found by solving Eq.(10) by allowing $\mathbf{R}^b = \mathbf{R}_3$, and $\mathbf{R}^s = 0$. Fig. 2.4(a) shows the potential functions contours compared to Fig. 2.4(b), the isolines of moment. The change in Φ_z between two contours, ($\Delta\Phi_z$), is $0.01229p_z$, and the ΔM is $0.01227p_z$.

Again, by utilizing Eq.(10), the potential function for plate with clamped boundary conditions can be determined. Fig. 2.5(a) shows the potential function contours compared to Fig. 2.5(b), the iso-lines of moment. The contours of Φ_z represent lines of constant curl-free force. The $\Delta\Phi_z$ between consecutive sets of contours is $0.01430p_z$ and the ΔM is $0.01406p_z$.

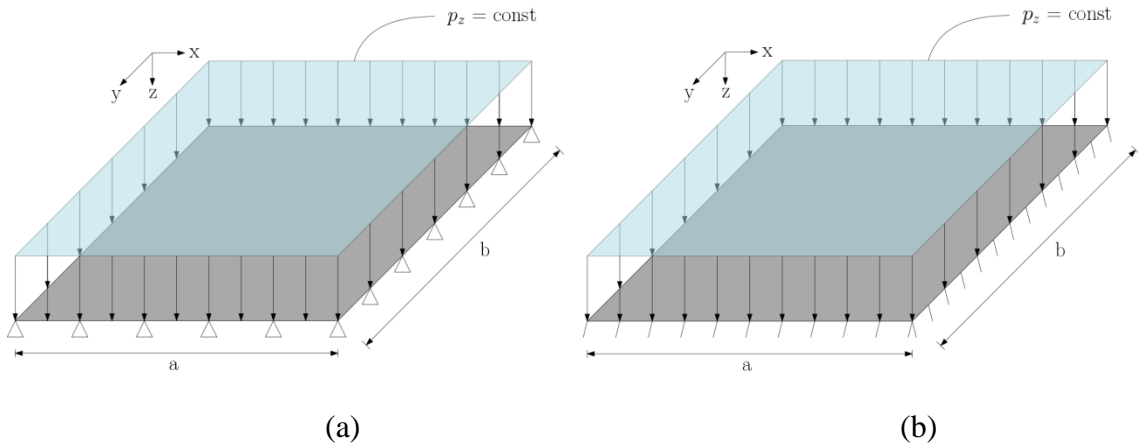


Fig. 2.3 A plate subjected to a uniform pressure, p_z , with (a) simply-supported edges and (b) clamped edges.

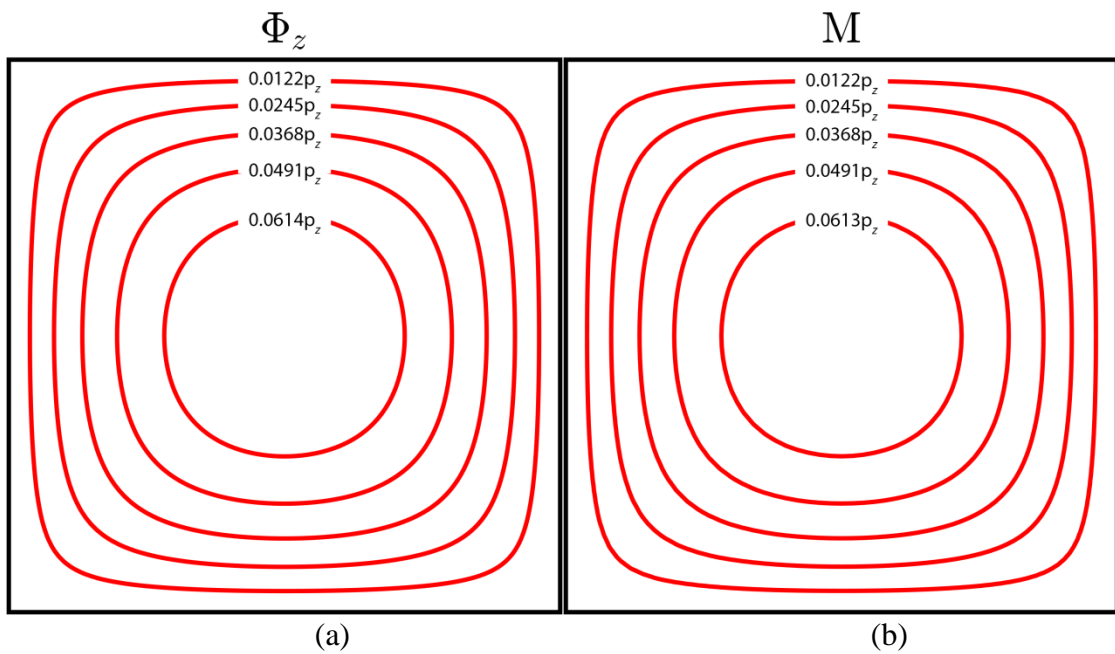


Fig. 2.4 The (a) potential function contours and (b) the iso-lines of total moment for a simply-supported plate under uniform pressure, p_z

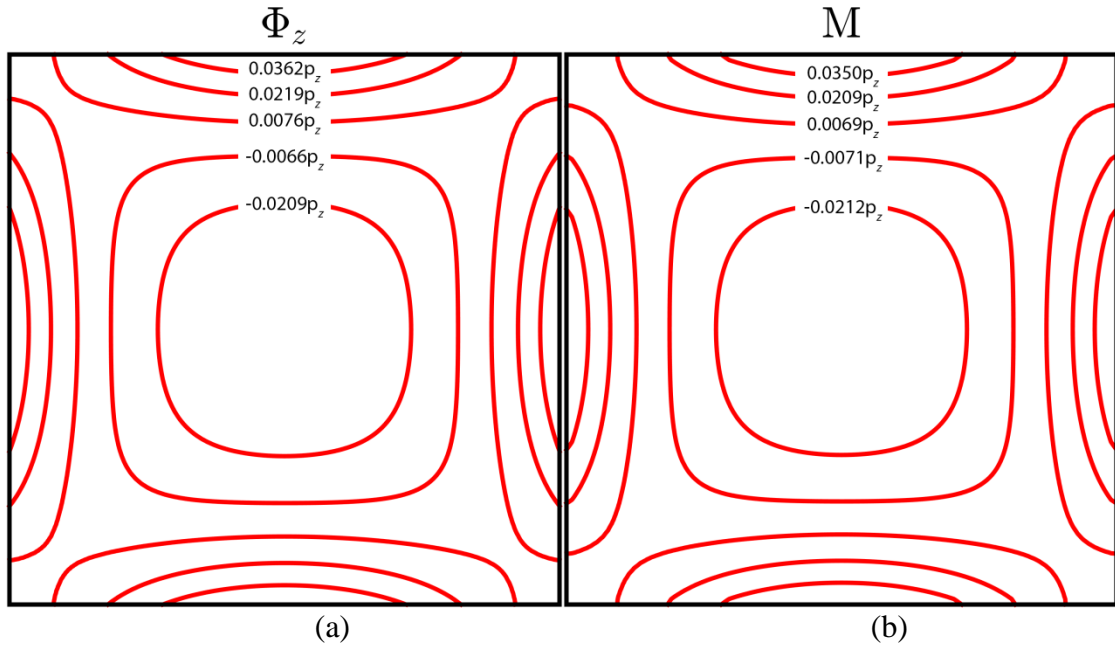


Fig. 2.5 The (a) potential function contours and (b) the iso-lines of total moment for a clamped plate under uniform pressure, p_z .

This example shows that the body force component of the transverse shear resultants is related to the total moment of the structure.

2.2.2. Roof structure subjected to body load

A set of panels following the form of a hyperbolic-paraboloid are pieced together to form a membrane roof structure. Fig. 2.6 shows the geometry of stitched roof panel. The roof is subjected to its own weight, $p_z = \rho g$. The projected membrane forces can be described using a nondimensionalized stress function as (Ugural, 2009),

$$\begin{aligned}
 \bar{N}_x &= -\frac{\rho g y}{2} \ln \frac{x + \sqrt{x^2 + y^2 + c^2}}{\sqrt{y^2 + c^2}} \\
 \bar{N}_y &= -\frac{\rho g y}{2} \ln \frac{x + \sqrt{x^2 + y^2 + c^2}}{\sqrt{y^2 + c^2}} \\
 \bar{N}_{xy} &= \frac{\rho g}{2} \sqrt{x^2 + y^2 + c^2}
 \end{aligned} \tag{23}$$

Where $c = \frac{a^2}{h}$. The projected forces are plotted onto the geometry in Fig. 2.7.

Using Eq.(8), the load functions for the divergence-free membrane forces can be found.

Fig. 2.8 shows the load paths for the load functions Ψ_x and Ψ_y respectively. Fig. 2.9

shows the contours of the potential functions Φ_x and Φ_y representing lines of constant curl-free membrane force.

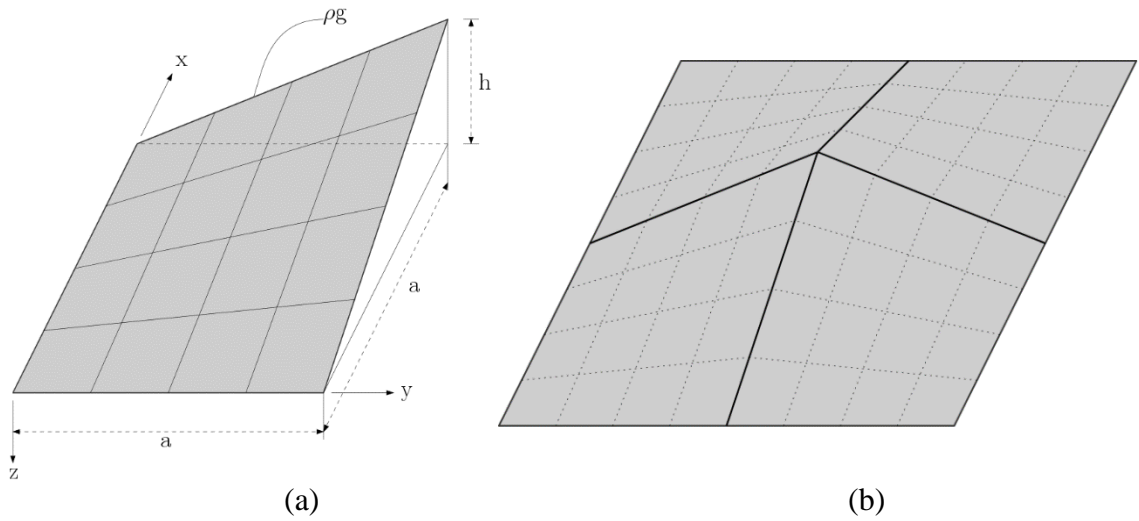


Fig. 2.6 The geometry of (a) a quarter-panel and (b) the full surface of a hyperbolic-paraboloid roof structure.

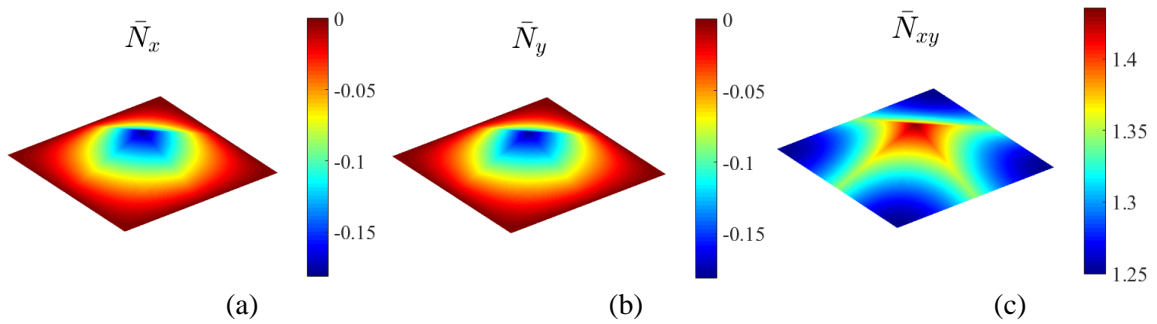


Fig. 2.7 The projected shell forces from Eq. (23) showing (a) \bar{N}_x , (b) \bar{N}_y , and (c) \bar{N}_{xy}

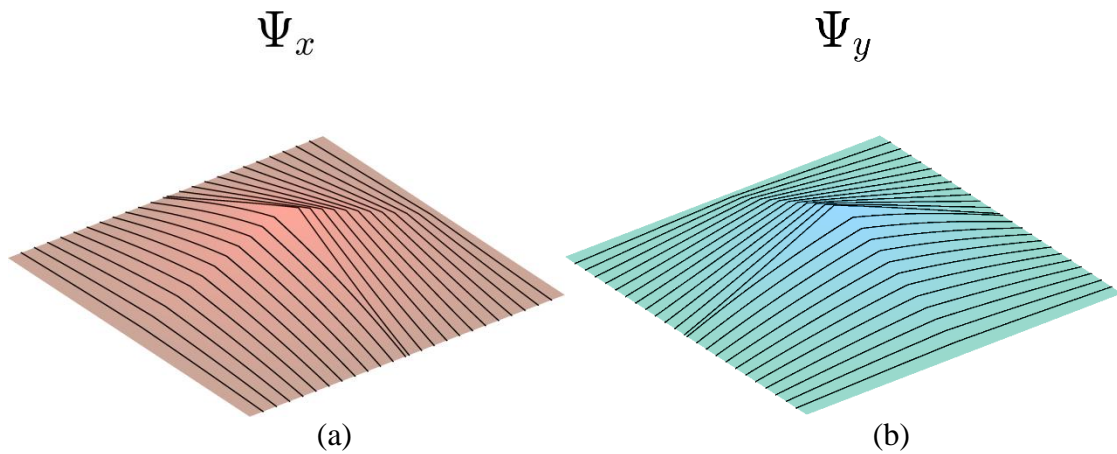


Fig. 2.8 Load paths in (a) x -direction and (b) y -direction for the membrane forces of a hyperbolic-paraboloid roof under its own weight.

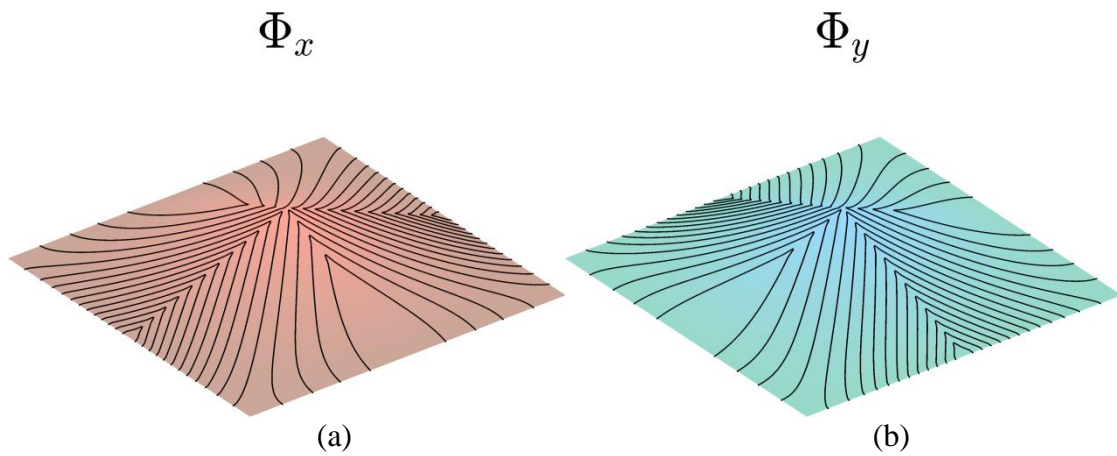


Fig. 2.9 Potential function contours for (a) x -direction and (b) y -direction membrane forces of a hyperbolic-paraboloid roof under its own weight.

The contours of the two load functions show the transfer, or flow, of the load in the x and y directions, respectively. The nature of the body load requires load paths to arc over the entire frame of the structure.

2.2.3. Skin panel subjected to aerodynamic loading

Assume an arbitrary isotropic wing skin panel, capable of supporting bending and membrane loads, subjected to an aerodynamic pressure load acting normal to the surface. The geometry and pressure distribution are shown in Fig. 2.10. This numerical example, and those that follow, also show how the present formulation can be incorporated into numerical structural methods, such as finite element methods. Furthermore, it demonstrates that the formulation can be used regardless of the specific loading or boundary conditions which include the possibility of internal and external loads from thermal, mechanical, and aerodynamic loads. This example will also be used as a validation to show that the stress field has been decomposed into curl-free and divergence-free components. The structural solution was solved using FEM (MSC.Nastran) using a pressure distribution found from vortex-lattice codes. The material selected has an elastic modulus of 10×10^6 Psi and a Poisson's ratio of 0.3.

The load functions Ψ_x , Ψ_y , and Ψ_z can be found by solving equation Eq.(8) using the stress field \mathbf{R} from FEM. The derivatives of load functions represent the solenoidal component of the stress field \mathbf{R}^s . Helmholtz-Hodge decomposition implies that the curl-free forces can be found by subtraction ($\mathbf{R}^b = \mathbf{R} - \mathbf{R}^s$). Fig. 2.11 shows the decomposition of the (a) stress field (\mathbf{R}) into the (b) solenoidal (\mathbf{R}^s) and (c) curl-free (\mathbf{R}^b) components. Furthermore, it can be shown in Fig. 2.11(d) that the decomposed stress field is equivalent to the total stress field $\mathbf{R} - (\mathbf{R}^b + \mathbf{R}^s) = 0$. An additional validation of the decomposition is to take the curl of curl-free forces ($\nabla \times \mathbf{R}^b$) and the divergence of the divergence-free forces ($\nabla \cdot \mathbf{R}^s$) to ensure they are zero (Fig. 2.12). The load paths of Ψ_x , Ψ_y , and Ψ_z are presented in Fig. 2.13 and the potential function contours of Φ_x , Φ_y , and Φ_z are presented in Fig. 2.14.

Φ_x are presented in Fig. 2.14.

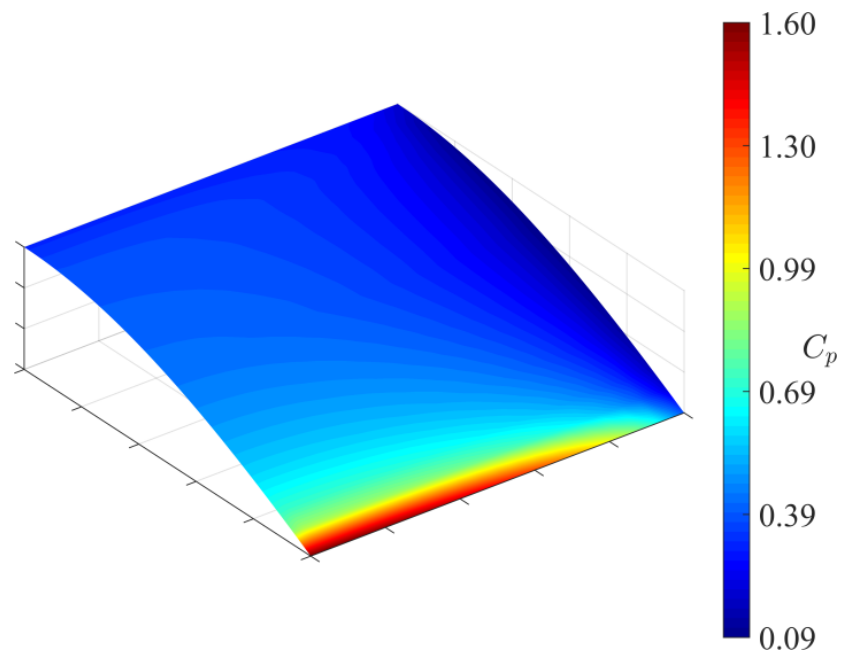


Fig. 2.10 Arbitrary wing skin panel subjected to aerodynamic loading.

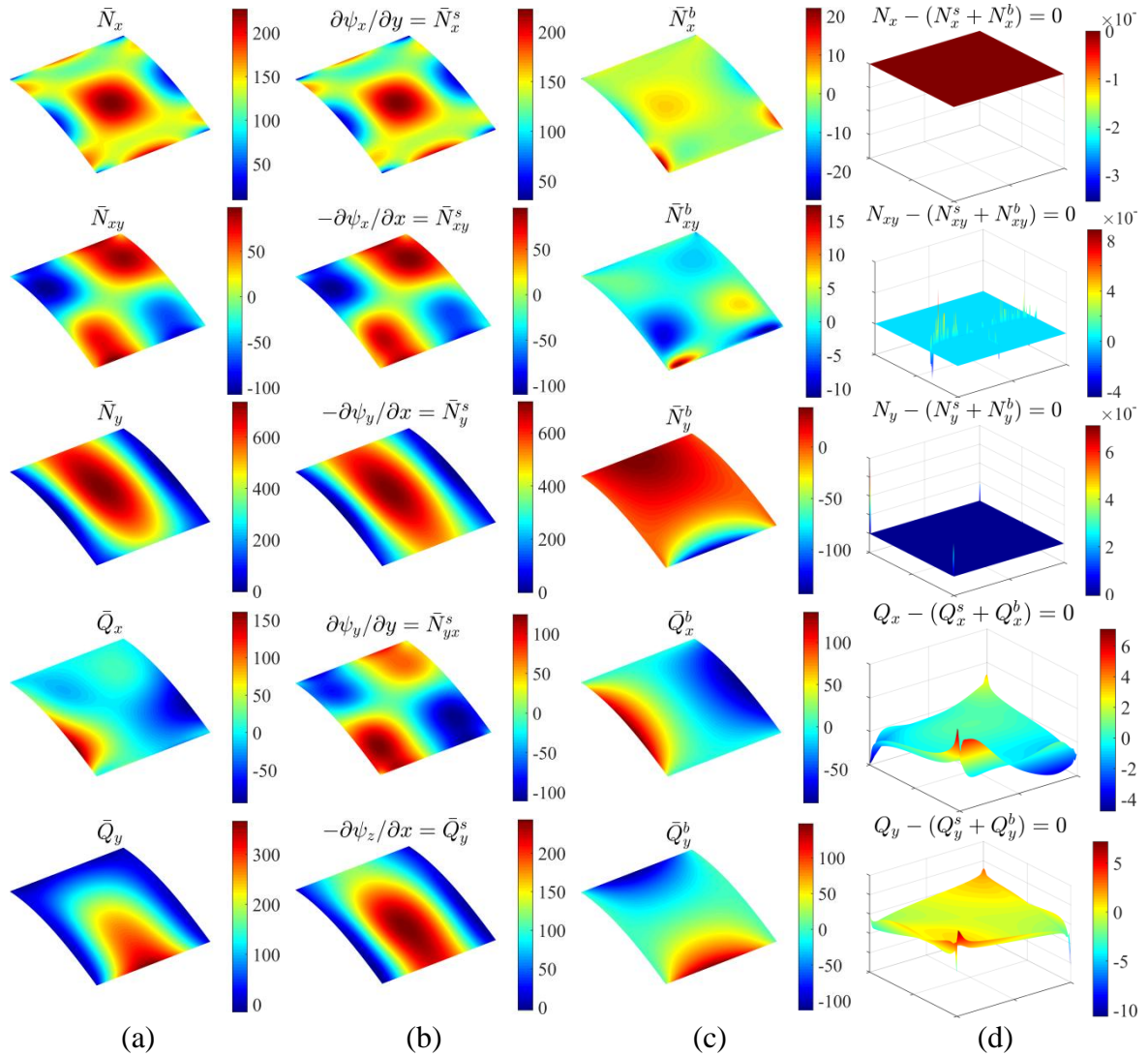


Fig. 2.11 Demonstrating the decomposition of the stress field, (a) the total force, (b) the self-equilibrated component, (c) the irrotational component, (d) the verification that they

add to zero.

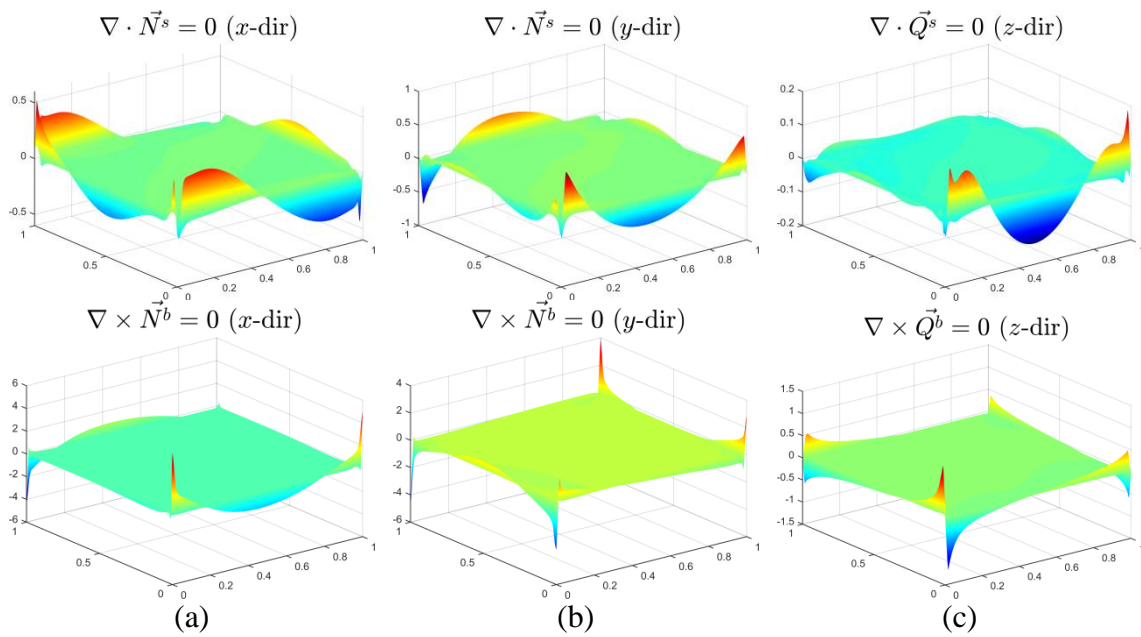


Fig. 2.12 Verifying that the self-equilibrated components are divergence-free and that irrotational components are curl-free for (a) *x*-direction, (b) *y*-direction, and (c) *z*-dir forces.

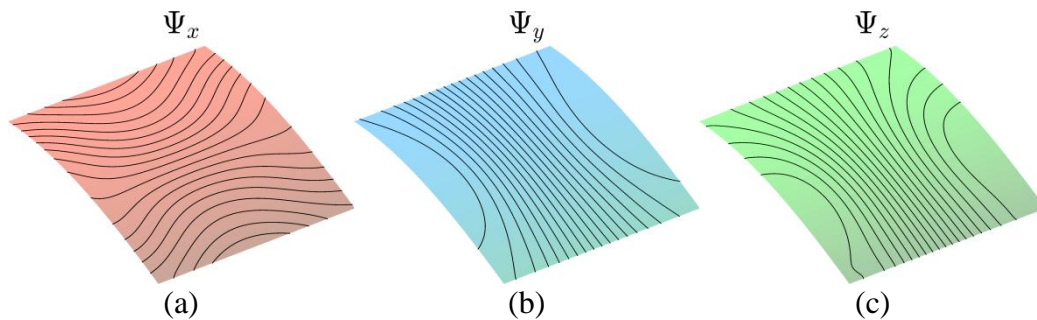


Fig. 2.13 Load paths in (a) *x*-direction, (b) *y*-direction, and (c) *z*-direction for a skin panel subjected to aerodynamic loading.

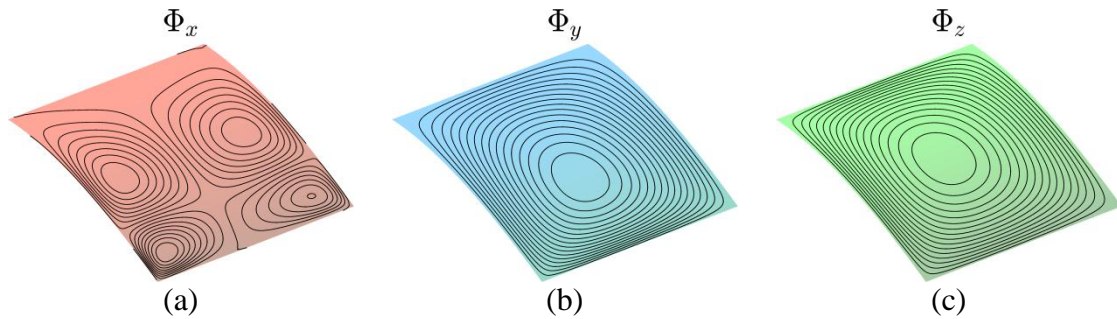


Fig. 2.14 Potential function contours in (a) x -direction, (b) y -direction, and (c) z -direction for a skin panel subjected to aerodynamic loading.

The load functions describe the membrane loads in x and y directions and also the transfer of load of the transverse shear resultants. The membrane load paths show how the forces from the x and y -direction equilibrium equations are being transferred from application to support. The potential functions are also presented for the x and y -direction equilibrium forces but their meaning is unclear. The potential function for the z -direction equilibrium equation is similar mathematically to the contours of moment.

2.2.4. Palazzetto dello Sport upper dome structure

The Palazzetto dello Sport, shown in (Fig. 2.15), was designed as an indoor sporting arena by Pier Luigi Nervi for the 1960 Olympic games in Rome, Italy (Hoogenboom). The upper dome structure was engineered as a thin-shell made of reinforced concrete with the inner surface overlaid with a lattice of concrete stiffeners in a radial pattern (Hoogenboom). The structure is modeled as a thin shell dome of constant thickness, omitting the stiffeners, and supporting its own weight (Fig. 2.16). A tensile modulus of 6×10^6 psi and a Poisson's ratio of 0.15 were used as material properties to model the concrete. The load paths of the functions of Ψ are shown in Fig. 2.17 and the

contours of the potential functions Φ are shown in Fig. 2.18.

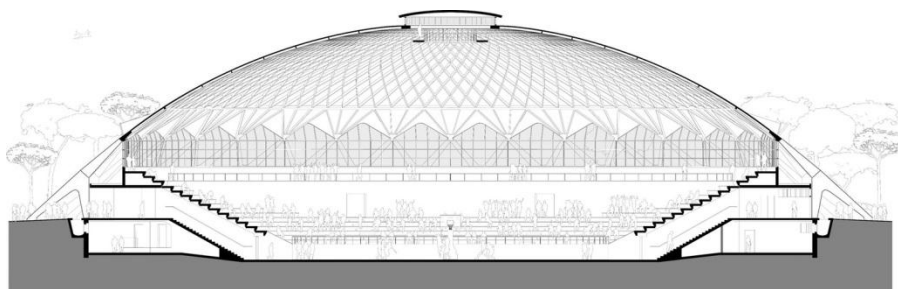


Fig. 2.15 Side view of the Palazzetto dello Sport (Cutrì, 2015).

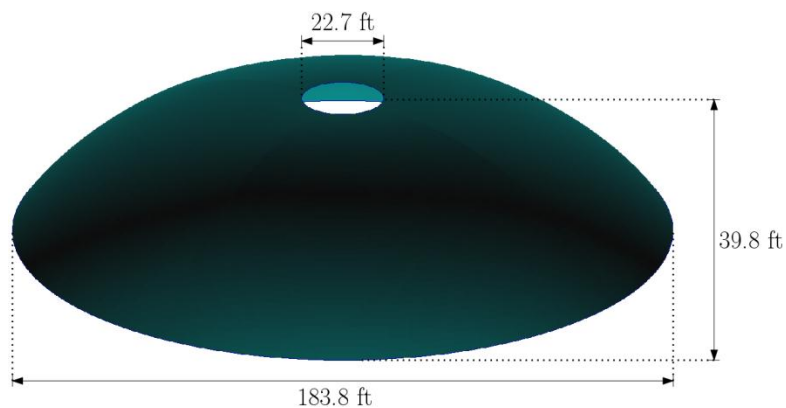


Fig. 2.16 Geometry of the dome of the Palazzetto dello Sport arena.

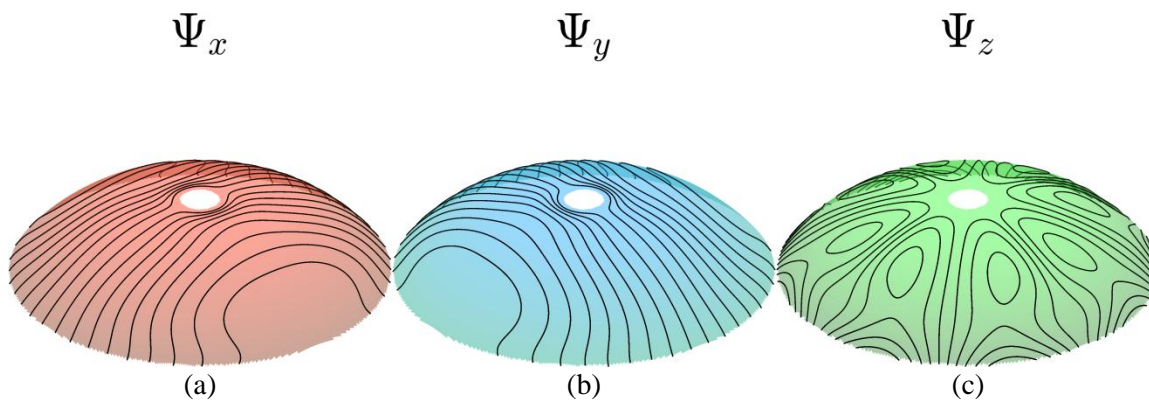


Fig. 2.17 Load paths in (a) x -direction, (b) y -direction, and (c) z -direction for the dome of the Palazzetto dello Sport arena under its own weight.

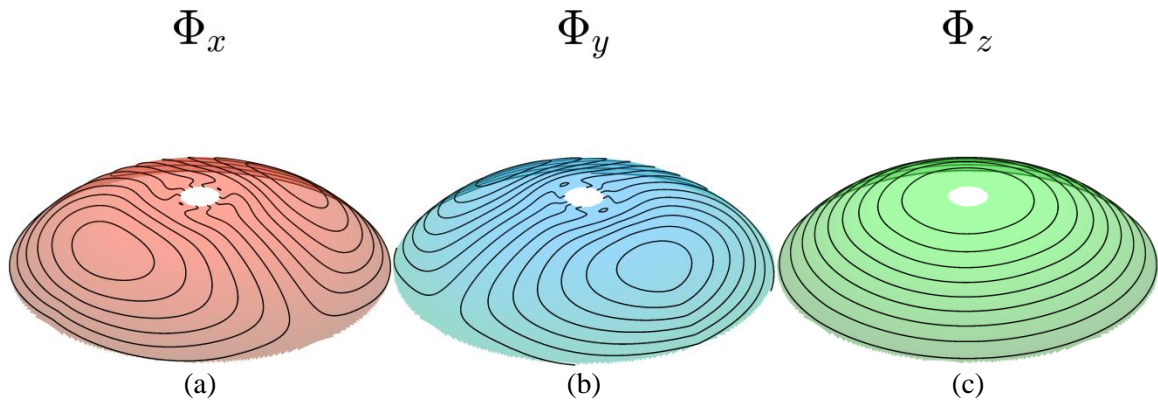


Fig. 2.18 Potential function contours in (a) x -direction, (b) y -direction, and (c) z -direction

for the dome of the Palazzetto dello Sport arena under its own weight.

The contours of the x and y -direction load functions show the transfer of the membrane forces. The contours of the load function for the transverse shear resultants show the transfer of the bending loads from application to support. Inspection of Fig. 2.17(c) shows that the contours of the load function are similar to the stiffener reinforcement scheme selected by Nervi during design (Cutrì, 2015).

2.3. Discussion

By expanding on the load path functions for 2D elasticity, the load path functions for load flow in shells is derived and the potential function method is introduced for the special case of a flat plate. The load path functions were proven to represent the load flow in the plate and shell structures. The formulations to determine the directional load paths from force equilibrium have been derived, and the numerical procedure to solve the resulting Poisson's equation has been discussed. Load paths were determined in examples with plates and shells subjected to different boundary conditions, loadings, and material properties, including structures with orthotropic materials. The results verify the assumptions of the load path function method, which is based on the relationship between derivative of load path function and resultant forces. Since the majority of structural parts used in the aerospace industry are composed of plates and shells, such as wings and fuselages, understanding and optimizing these structures are of utmost importance to increase performance. Analysis and interpretation of the load paths has the potential to be an important tool for determination of reinforcements in any structure. Additionally, the load path function method increases the possibility of using load paths for layout and topology optimization as well as trajectories for fiber-steered composites.

3. VARIABLE STIFFNESS COMPOSITES

The determination of optimized fiber orientations for variable stiffness composites will now be investigated. Classical methods of optimized design will be compared against methods proposed that utilize structural load paths. The methodology of each process will be explained; then examples showing comparisons between global

compliance, convergence history, solution stability, and fiber continuity will be presented. Additionally, a method for fiber filtering is included as a possible remedy to fix discontinuous and unstable fiber solutions.

3.1. Methodology

The goal is to minimize the compliance for the structure by minimizing the strain energy on each design cell, e . The objective function is written as,

$$\min_{\Omega} u_e = \epsilon_e^T \bar{C}(\theta_e) \epsilon_e = \epsilon_e^T T^{-1} C T \epsilon_e \quad (24)$$

$$\text{Where: } -\frac{\pi}{2} \leq \theta_e \leq \frac{\pi}{2} \quad (25)$$

Where C is the unrotated stiffness matrix, T is the transformation matrix, ϵ_e is the strain vector, and θ_e is the design variable representing the fiber orientation angle. Using the elements of FEM as each design cell, we can solve Eq.(24) on each element to determine to the least compliant structure. Fig. 3.1 shows the rotation of a design cell within the design domain.

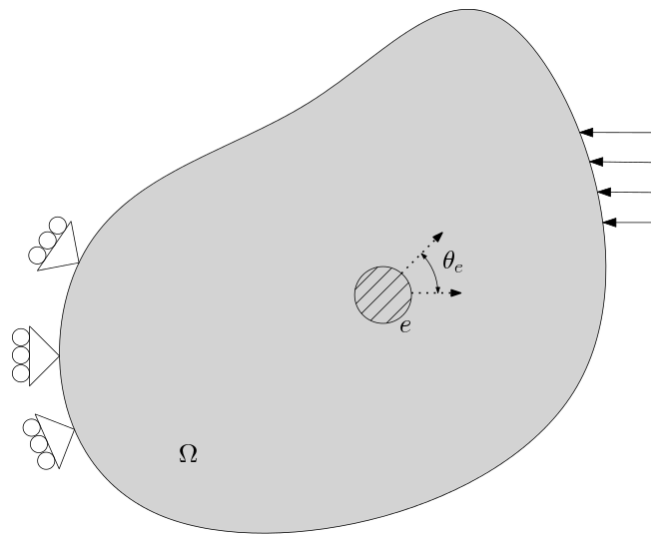


Fig. 3.1 Arbitrary domain, Ω , showing a design cell and its rotation angle, θ_e .

3.1.1. Strain method

The strain method, as documented by (Pedersen, 1989), assumes the strain field is fixed for each element and altering the material orientation has no residual effect on the strain. The sensitivity of the objective function with respect to design variable is,

$$\frac{\partial u_e}{\partial \theta_e} = \frac{\partial}{\partial \theta_e} (\epsilon_e^T \bar{C}(\theta_e) \epsilon_e) = \epsilon_e^T \frac{\partial \bar{C}(\theta_e)}{\partial \theta} \epsilon_e = 0 \quad (26)$$

Where it is assumed the strain is invariant with respect to the orientation, leaving the sensitivity a function of the rotated stiffness matrix, \bar{C} . The strain vector ϵ_e is comprised of ϵ_1 , ϵ_2 and γ_{12} . Expansion of transformation matrices embedded inside of Eq.(26) leads to the expression,

$$\frac{\partial u_e}{\partial \theta_e} = A \sin 2\theta_e + B \cos 2\theta_e + D \sin 4\theta_e + E \cos 4\theta_e = 0 \quad (27)$$

Where the coefficients A, B, D, and E are,

$$\begin{aligned} A &= -2a(\epsilon_2^2 - \epsilon_1^2) \\ B &= -2a\gamma_{12}(\epsilon_2 + \epsilon_1) \\ D &= -2b(\gamma_{12} - (\epsilon_2 - \epsilon_1)^2) \\ E &= -4b\gamma_{12}(\epsilon_1 - \epsilon_2) \end{aligned} \quad (28)$$

The terms a and b are determined by the material properties as,

$$\begin{aligned} a &= \frac{c_{11}^0 - c_{22}^0}{2} \\ b &= \frac{c_{11}^0 - 2c_{12}^0 + c_{22}^0 - 4c_{66}^0}{4} \end{aligned} \quad (29)$$

The values of c_{11}^0 , c_{12}^0 , c_{22}^0 , and c_{66}^0 correspond to entries in the unrotated stiffness

matrix C,

$$C = \begin{bmatrix} c_{11}^0 & c_{12}^0 & 0 \\ c_{12}^0 & c_{22}^0 & 0 \\ 0 & 0 & c_{66}^0 \end{bmatrix} \quad (30)$$

Solutions for Eq.(27) can be found by solving the polynomial,

$$(E - B)x^4 + (2A - 4D)x^3 - 6Ex^2 + (2A + 4D)x + (B + E) = 0 \quad (31)$$

Where x is expressed as $\tan \theta_e$. Solving Eq.(31) should yield 4 roots between $(-\frac{\pi}{2} \leq \theta \leq \frac{\pi}{2})$. The root, or roots, corresponding with minimum strain energy can be found by inserting the roots into,

$$u = -2A \cos 2\theta + 2B \sin 2\theta - D \cos 4\theta + E \sin 4\theta \quad (32)$$

3.1.2. Stress method

The stress based method (Diaz & Bendsøe, 1992) is analogous to the strain method but instead rotates the compliance matrix with respect to a fixed strain field. The sensitivity equation for the strain method, Eq.(26), can be rewritten in terms of stresses as,

$$\frac{\partial u_e}{\partial \theta_e} = \frac{\partial}{\partial \theta_e} (\sigma_e^T \bar{S}(\theta_e) \sigma_e) = \sigma_e^T \frac{\partial \bar{S}(\theta_e)}{\partial \theta} \sigma_e = 0 \quad (33)$$

Just like the strain method, the stress method also assumes the stress field of the element is invariant with respect to the change of orientation. The stress vector, σ_e , is comprised of σ_1 , σ_2 , and τ_{12} , and \bar{S} is the rotated compliance matrix. Solving Eq.(33) on each element follows the same procedure as the strain based method. For the stress based method, the coefficients A, B, D, and E from Eq.(27) can be written as,

$$\begin{aligned}
A &= c(\sigma_2^2 - \sigma_1^2) \\
B &= 2c\tau_{12}(\sigma_2 + \sigma_1) \\
D &= d(4\tau_{12} - (\sigma_1 - \sigma_2)^2) \\
E &= 4d\tau_{12}(\sigma_1 - \sigma_2)
\end{aligned} \tag{34}$$

Where c and d are material property parameters determined by,

$$\begin{aligned}
c &= s_{11}^0 - s_{22}^0 \\
d &= \frac{s_{11}^0 - 2s_{12}^0 + s_{22}^0 - s_{66}^0}{2}
\end{aligned} \tag{35}$$

The values of s_{11}^0 , s_{12}^0 , s_{22}^0 , and s_{66}^0 correspond to entries in the unrotated compliance matrix S ,

$$S = \begin{bmatrix} s_{11}^0 & s_{12}^0 & 0 \\ s_{12}^0 & s_{22}^0 & 0 \\ 0 & 0 & s_{66}^0 \end{bmatrix} \tag{36}$$

3.1.3. Energy method

The energy method (Luo & Gea, 1998) is a first-order approximation of the stress and strain based methods. The stress and strain field is no longer assumed to be fixed and the change in stress and strain due to the rotation of compliance matrix is implicitly quantified. This is done by carefully studying what happens when a design cells orientation changes.

Assume a design cell in the domain Ω . The current strain and stress in the unrotated design cell is $\epsilon_e = \epsilon_0$ and $\sigma_e = C\epsilon_0$. When the cell is rotated by the angle θ_e the stress will change, but the cell's strain must be the same so that the displacements are continuous with the adjacent structure. Therefore, the cell's strain remains $\epsilon_e = \epsilon_0$ and the stress becomes $\sigma_e = \bar{C}\epsilon_0$. The strains are continuous between the design cell and the

adjacent structure; however, the stresses are now discontinuous. To correct this, a fictitious surface traction, $\bar{\sigma}$, is applied on the design cell that is equal and opposite to the change in stress caused by the cell's rotation,

$$\bar{\sigma} = (\bar{C} - C)\epsilon_0 \quad (37)$$

Application of this surface traction will produce new strains and stresses of unknown quantity. The stress and strain of the element now becomes,

$$\begin{aligned} \epsilon_e &= \epsilon_0 + \Delta\epsilon \\ \sigma_e &= \bar{C}\epsilon_0 + \Delta\sigma \end{aligned} \quad (38)$$

Where the values of $\Delta\epsilon$ and $\Delta\sigma$ caused by the applied stress $\bar{\sigma}$ are unknown, they can be approximated using energy factor, α . The energy factor is defined as a ratio that describes how much work the stress $\bar{\sigma}$ performs on the design cell vs. how much work it performs on the surrounding structure. Therefore, $\Delta\epsilon$ and $\Delta\sigma$ can be approximated as,

$$\begin{aligned} \Delta\epsilon &= \alpha\bar{S}(-\bar{\sigma}) \\ \Delta\sigma &= \alpha(-\bar{\sigma}) \end{aligned} \quad (39)$$

Now Eq.(38) can be rewritten as,

$$\begin{aligned} \epsilon_e &= \epsilon_0 + \alpha\bar{S}\bar{\sigma} = \epsilon_0 + \alpha\bar{S}(C - \bar{C})\epsilon_0 \\ \sigma_e &= \sigma_0 + \alpha\bar{\sigma} = \sigma_0 + \alpha(C - \bar{C})\epsilon_0 \end{aligned} \quad (40)$$

By substituting Eq.(40) into Eq.(26), the sensitivity of the strain energy with respect to orientation can be found,

$$\frac{\partial u}{\partial \theta} = (-1 + 2\alpha - \alpha^2)\epsilon_0^T \frac{\partial \bar{C}}{\partial \theta} \epsilon_0 + \alpha^2 \sigma_0^T \frac{\partial \bar{S}}{\partial \theta} \sigma_0 + (2\alpha - 2\alpha^2)\epsilon_0^T \frac{\partial \bar{C}}{\partial \theta} \bar{S} \sigma_0 = 0 \quad (41)$$

Solutions to Eq.(41) can be found by using Eq.(27) with the following coefficients for A, B, D, and E,

$$\begin{aligned}
A &= 2a(-1 + 2\alpha - \alpha^2) (\epsilon_2^{0^2} - \epsilon_1^{0^2}) + c\alpha^2 (\sigma_2^{0^2} - \sigma_1^{0^2}) \\
&\quad + (2\alpha - 2\alpha^2) \left[\left(2as_{01} + bc - \frac{ad}{2} \right) (\epsilon_2^0 \sigma_2^0 - \epsilon_1^0 \sigma_1^0) \right. \\
&\quad \left. + \left(2as_{02} + bc - \frac{ad}{2} \right) (\epsilon_2^0 \sigma_1^0 - \epsilon_1^0 \sigma_2^0) \right] \\
B &= 2a\gamma_{12}^0 (-1 + 2\alpha - \alpha^2) (\epsilon_1^0 + \epsilon_2^0) + 2c\tau_{12}\alpha^2 (\sigma_1^0 + \sigma_2^0) \\
&\quad + (2\alpha - 2\alpha^2) \{ \gamma_{12}^0 [a(s_{01} + s_{02}) + bc] (\sigma_1^0 + \sigma_2^0) \\
&\quad + a\tau_{12}(s_{03} - d) (\epsilon_1^0 + \epsilon_2^0) \} \\
D &= b2a(-1 + 2\alpha - \alpha^2) (4\epsilon_1^0 \epsilon_2^0 - 2\epsilon_1^{0^2} - 2\epsilon_2^{0^2} + 2\gamma_{12}^{0^2}) \\
&\quad + d\alpha^2 (2\sigma_1^0 \sigma_2^0 - \sigma_1^{0^2} - \sigma_2^{0^2} + 4\tau_{12}^{0^2}) \\
&\quad + (2\alpha - 2\alpha^2) \left\{ \left[2b(s_{01} - s_{02}) + \frac{ac}{4} \right] (\epsilon_1^0 - \epsilon_2^0) (\sigma_2^0 - \sigma_1^0) \right. \\
&\quad \left. + \left(2bs_{03} + \frac{ac}{2} \right) \tau_{12}^0 \gamma_{12}^0 \right\} \\
E &= 4b\gamma_{12}^0 (-1 + 2\alpha - \alpha^2) (\epsilon_1^0 - \epsilon_2^0) + 4d\tau_{12}^0 \alpha^2 (\sigma_1^0 - \sigma_2^0) \\
&\quad + (2\alpha - 2\alpha^2) \left\{ \gamma_{12}^0 \left[2b(s_{01} - s_{02}) + \frac{ac}{4} \right] (\sigma_1^0 - \sigma_2^0) \right. \\
&\quad \left. + \tau_{12}^0 \left(2bs_{03} + \frac{ac}{2} \right) (\epsilon_1^0 - \epsilon_2^0) \right\}
\end{aligned} \tag{42}$$

The additional material constants s_{01} , s_{02} and s_{03} are defined as,

$$\begin{aligned}
s_{01} &= \frac{3s_{11}^0 + 2s_{12}^0 + 3s_{22}^0 - s_{66}^0}{8} \\
s_{02} &= \frac{s_{11}^0 + 6s_{12}^0 + s_{22}^0 - s_{66}^0}{8} \\
s_{03} &= \frac{s_{11}^0 - 2s_{12}^0 + s_{22}^0 + s_{66}^0}{2}
\end{aligned} \tag{43}$$

3.1.4. Dominant Load path method

The dominant load path method uses the concept of load paths to determine optimal orientation for the orthotropic material to achieve minimum compliance. This is contrary to the strain, stress, and energy methods for many reasons. Most importantly, it does not solve Eq.(24) directly and instead aligns the orientation tangent to the physical load flow of the structure using the load path function method.

For each design cell, or FEM element, the dominant load path pointing vector is selected as the materials orientation angle. The dominant load path pointing vector is the load path angle associated with the larger of the two traction forces. The load path pointing vector can be found by taking the curl of the load path function at centroid of each element. The corresponding orientation angle, θ_e , can be found by taking the inverse tangent of the resulting vector.

$$\max \begin{cases} V_x \rightarrow \nabla \times \Psi_x = \frac{\partial \Psi_x}{\partial y} \hat{i} - \frac{\partial \Psi_x}{\partial x} \hat{j} = \sigma_x^s \hat{i} + \tau_{xy}^s \hat{j} \rightarrow \theta_e = \tan^{-1} \frac{\tau_{xy}^s}{\sigma_x^s} \\ V_y \rightarrow \nabla \times \Psi_y = \frac{\partial \Psi_y}{\partial y} \hat{i} - \frac{\partial \Psi_y}{\partial x} \hat{j} = \tau_{xy}^s \hat{i} + \sigma_y^s \hat{j} \rightarrow \theta_e = \tan^{-1} \frac{\sigma_y^s}{\tau_{xy}^s} \end{cases} \quad (44)$$

Where the traction forces V_x and V_y are defined as,

$$\begin{aligned} V_x &= \sqrt{\sigma_x^{s2} + \tau_{xy}^{s2}} \\ V_y &= \sqrt{\tau_{xy}^{s2} + \sigma_y^{s2}} \end{aligned} \quad (45)$$

If fiber reinforcement is being designed to resist bending loads, the z-dir load path function, Ψ_z can be used to determine optimal fiber orientations,

$$\nabla \times \Psi_z = \frac{\partial \Psi_z}{\partial y} \hat{i} - \frac{\partial \Psi_z}{\partial x} \hat{j} = Q_x^s \hat{i} + Q_y^s \hat{j} \rightarrow \theta_e = \tan^{-1} \frac{Q_y^s}{Q_x^s} \quad (46)$$

3.1.5. Weighted load path method

The dominant load path method is a binary approach that selects the angle based off the largest traction forces. The weighted load path method considers the proportionality of each traction force to generate a weighted orientation angle. The weighting coefficients are introduced as,

$$\begin{aligned}
 w_x &= \frac{V_x}{V_x + V_y} \\
 w_y &= \frac{V_y}{V_x + V_y}
 \end{aligned}
 \tag{47}$$

The process to determine the orientation angle from Eq.(44) is rewritten as a weighted average as,

$$\theta_e = w_x \tan^{-1} \frac{\tau_{xy}^s}{\sigma_x^s} + w_y \tan^{-1} \frac{\sigma_y^s}{\tau_{xy}^s}
 \tag{48}$$

3.1.6. Fiber filtering

The stress, strain, and energy methods, as well the load path methods, can all produce issues with fiber smoothness and discontinuity and sometimes, the solution methods produce unstable results. To address these issues, two methods of filtering have been proposed. The filter sacrifices overall compliance to achieve better fiber continuity, solution stability, and faster convergence. The two filter schemes average the orientations of the elements within a prescribed search radius, r . The first method is a direct average,

$$\theta_e = \frac{\sum_{i=1}^n \theta_i}{n}
 \tag{49}$$

Where i is the i th element within the search radius and n is the number of elements that fall into that search radius. The radius is measured from the centroid of the element e and searches for all other element centroids. The second approach uses a linearly weighted average described by,

$$\theta_e = \frac{\sum_{i=1}^n \frac{r - r_i}{r} \theta_i}{\sum_{i=1}^n \frac{r - r_i}{r}} \quad (50)$$

Where r_i is the distance from the centroid of element e to the centroid of the query element i . In effect, it grants greater proportionality to the orientation angles closer to element e .

3.2. Results

A set of examples will be presented showing the implementation of these methods. The optimal fiber orientations will be found and the methods will be compared based off their speed of convergence, converged compliance, and fiber continuity. The first example will be a plate clamped at one end with a shear load at the other. The second example will be a pin loaded plate with a bearing load. The last example will be a fighter jet wing loaded and bending due to aerodynamic pressure.

3.2.1. Plate loaded in shear

For this example, assume a rectangular plate in a state of plane-stress, clamped on one end and loaded in shear on the other, as shown in Fig. 3.2. This problem is presented as a benchmark example comparable to other results commonly found in the literature.

The width of the plate is 200mm and the height is 100mm. The plate has a 20x40 element QUAD4 mesh shown in Fig. 3.3. The material is a single-ply laminate with $E_1 = 137.9$ GPa, $E_2 = 10.34$ GPa, $G_{12} = 6.89$ GPa, and the Poisson's ratio is 0.29. The orientation of the lamina is open to design on each element. The lamina thickness is 0.002 mm and the applied force is 10 kN. The initialized structure has all the fiber orientations set 0 deg.

The initial compliance is 34.24 N·mm.

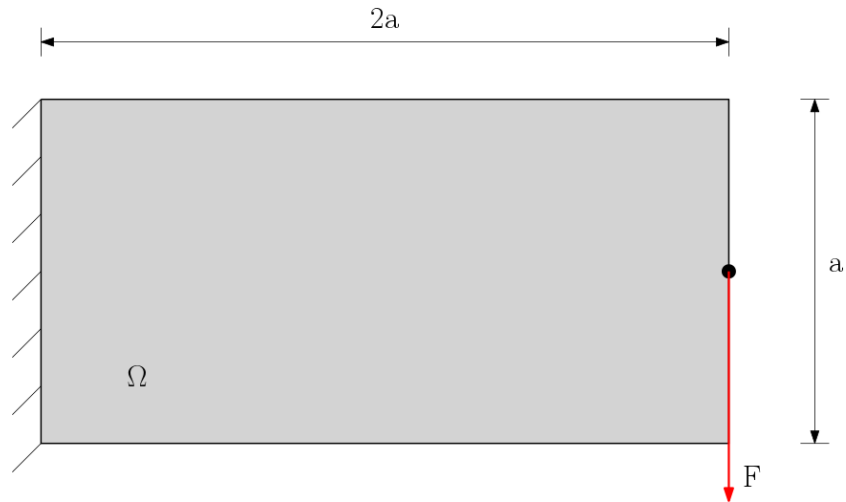


Fig. 3.2 Rectangular plate subjected to a shear load.

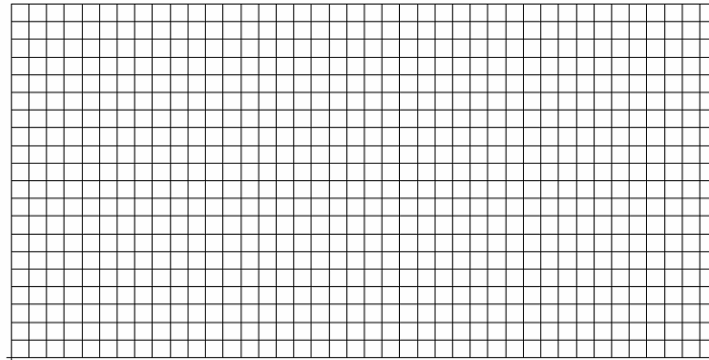


Fig. 3.3 A 20x40 element FEM mesh.

The five methods discussed (strain, stress, energy, dominant load path, and weighted) will be run for this problem. All solutions are run for 200 iterations with a maximum $\Delta\theta$ set to 3 deg. That limits the amount of orientation change for each element to aid in solution stability. Larger $\Delta\theta$ values can lead to unstable solutions that do not converge. Fig. 3.4 through Fig. 3.8 show the converged orientation solution with the fiber

angle mapped onto the centroid of each element of the structure. All methods produce fiber discontinuity in the top and bottom corners on the right-hand side of the plate; however, this is a lightly loaded area of the structure where fiber discontinuity is not a structural concern. The strain, stress, and weighted load path methods all produce similar fiber distributions. The energy method solution Fig. 3.6 produces a cross-thatched pattern in the interior of the plate, but it should be noted that for a single ply laminate the solution could not be manufactured. The cross-thatched pattern appears in areas where the shear stress is dominating the stress field and is reminiscent to the checkerboard instability found in topology optimization problems. The dominant load path method also produces a unique fiber distribution compared to the other solutions. Close inspection of Fig. 3.7 shows a distinct transition boundary from Ψ_x load paths to the Ψ_y load paths which can be attributed to the binary nature of Eq.(44).

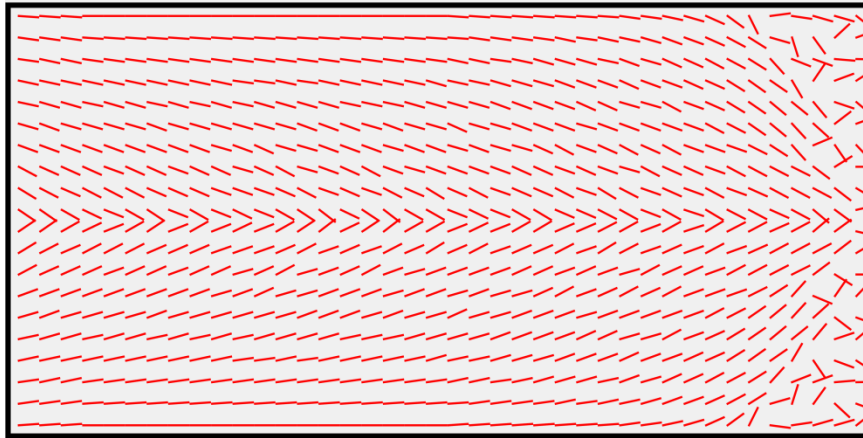


Fig. 3.4 Converged solution using the strain method.

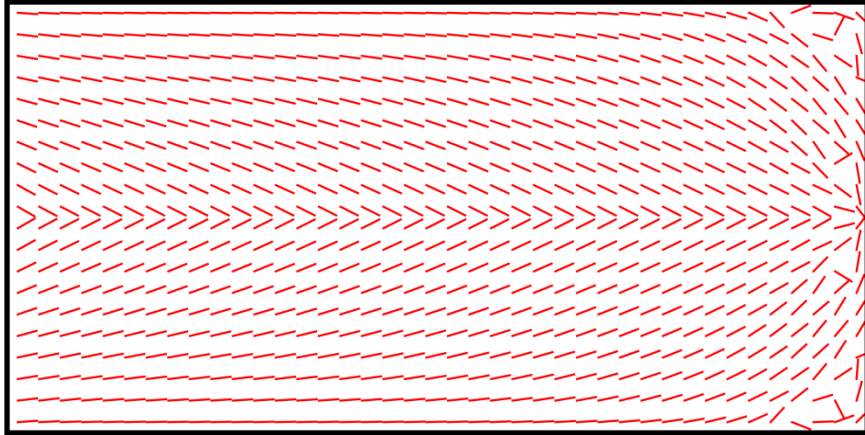


Fig. 3.5 Converged solution using the stress method.

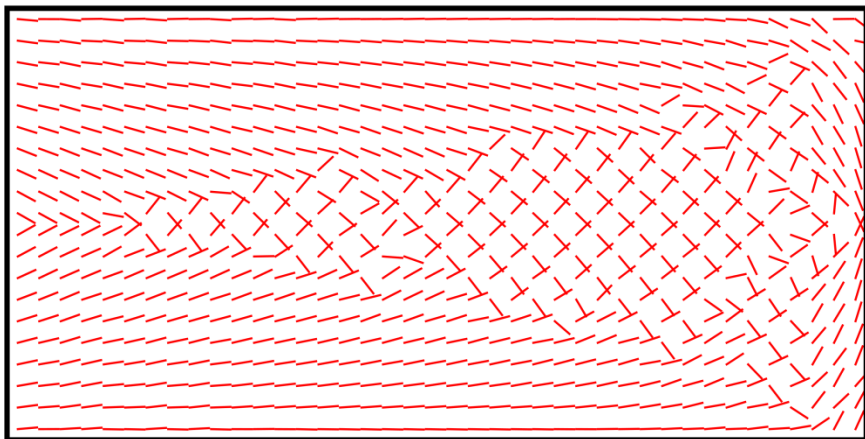


Fig. 3.6 Converged solution using the energy method.

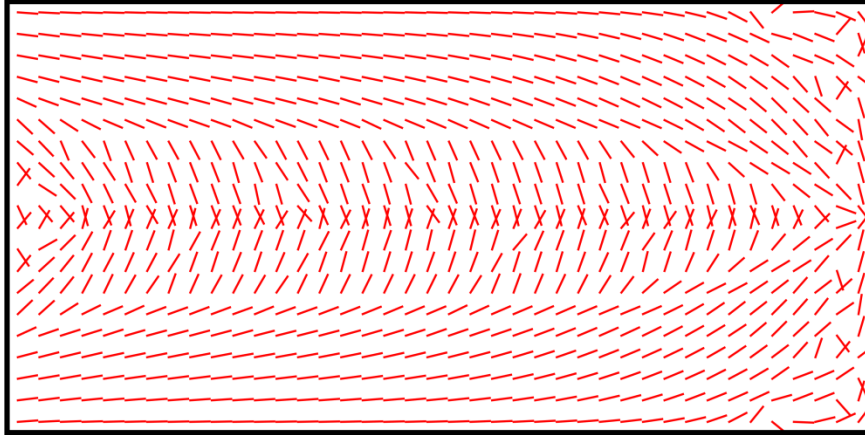


Fig. 3.7 Converged solution using the dominant load path method.

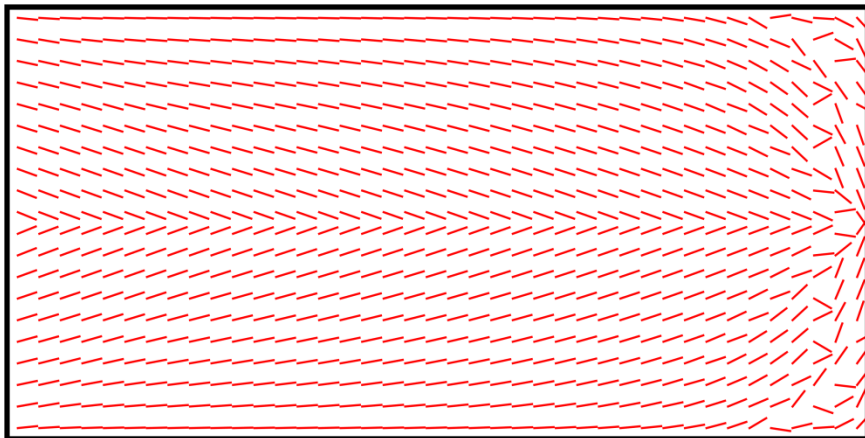


Fig. 3.8 Converged solution using the weighted load path method.

Fig. 3.9 shows the convergence history over 200 design iterations. The energy, stress, and weighted load path method converge to the lowest compliance, comparable to the optimized designs found in the literature (Brampton et al., 2015). The strain and dominant load path method do converge, but their converged compliance does not rank as well as the other methods. Table 3.1 shows the comparisons of the final converged compliance solution determined by each method which is compared to the initial,

straight-fiber design. For this structure and load, the energy method achieves a 53.55% reduction in compliance over the initial design. The stress method and weighted load path method record a 52.25% and 51.05% drop in compliance, respectively. Even though the stress and weighted load path methods do not score as well as the energy method, it is evident that the formers' fiber orientations are more desirable from a manufacturing point of view which must be taken into consideration during design.

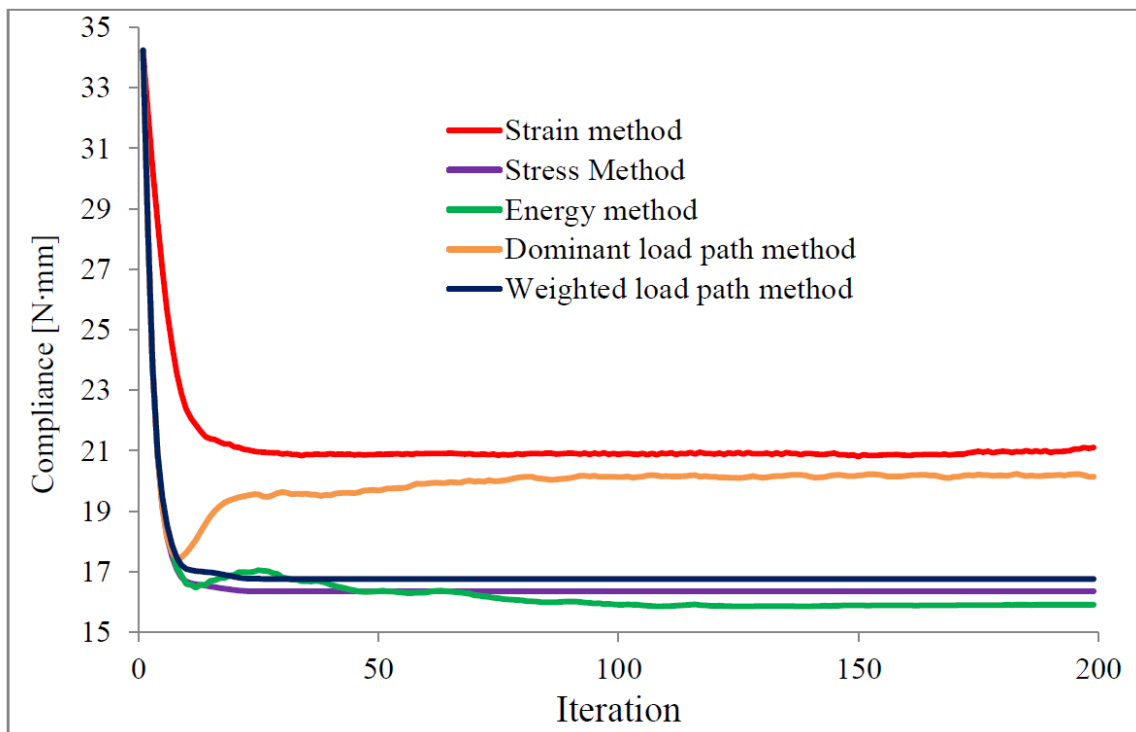


Fig. 3.9 Convergence history of each method through 200 design iterations

Table 3.1 Comparison of the overall compliance of the converged solutions.

Method	Compliance	Percent difference
Initial design (0 deg fiber)	34.24	
Strain	21.08	-38.41

Stress	16.35	-52.25
Energy	15.90	-53.55
Dominant load path	20.14	-41.16
Weighted load path	16.75	-51.05

Now, the fiber filtering methods will be demonstrated to produce fiber orientations more adequate for manufacturing and to aid in solution stability. The five solution methods were run again with direct averaging scheme described in Eq.(49) with a search radius of 10mm. The filtering was performed at the end of each design iteration. Fig. 3.10 through Fig. 3.14 show the converged fiber distributions after filtering.

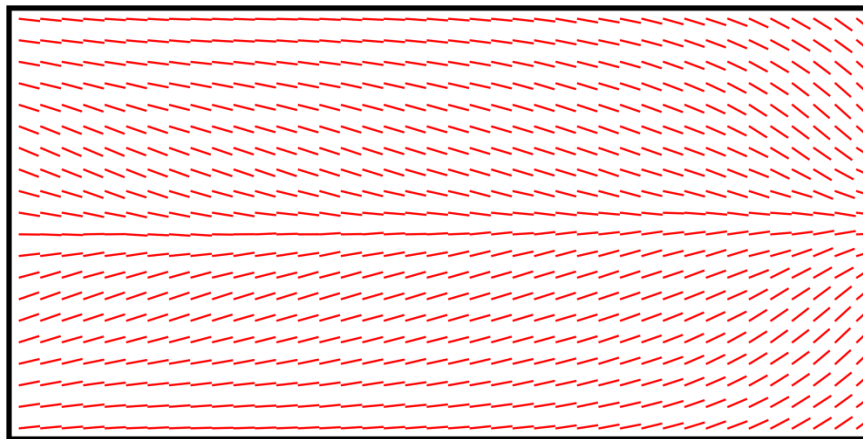


Fig. 3.10 Converged solution of the strain method using fiber filtering.

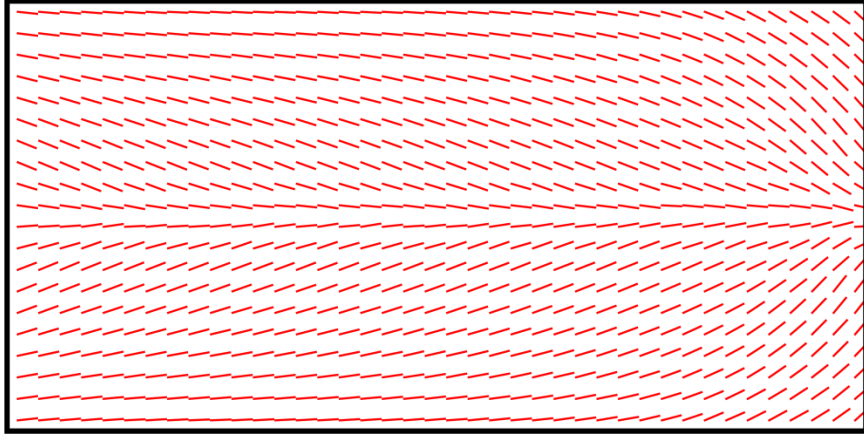


Fig. 3.11 Converged solution of the stress method using fiber filtering.

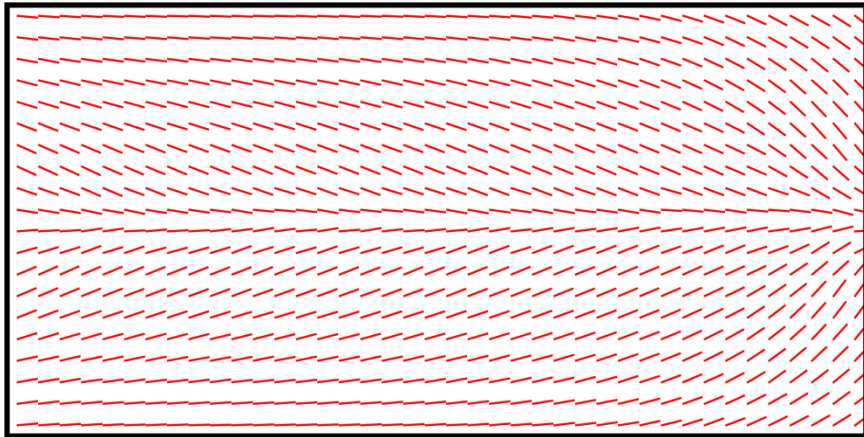


Fig. 3.12 Converged solution of the energy method using fiber filtering.

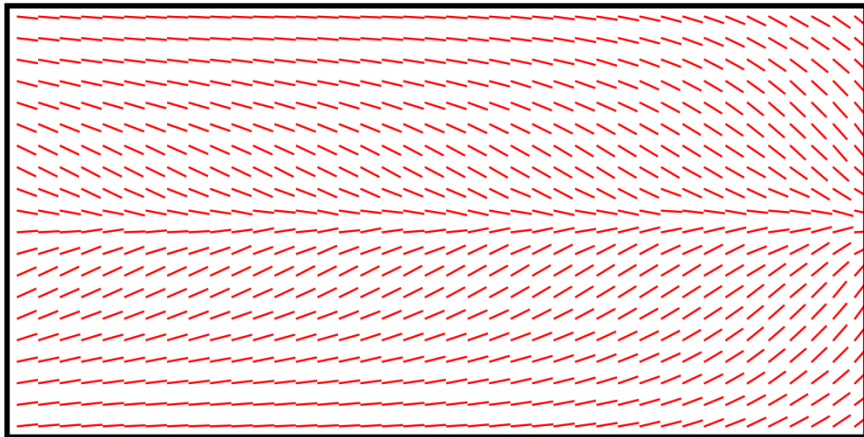


Fig. 3.13 Converged solution of the dominant load path method using fiber filtering.

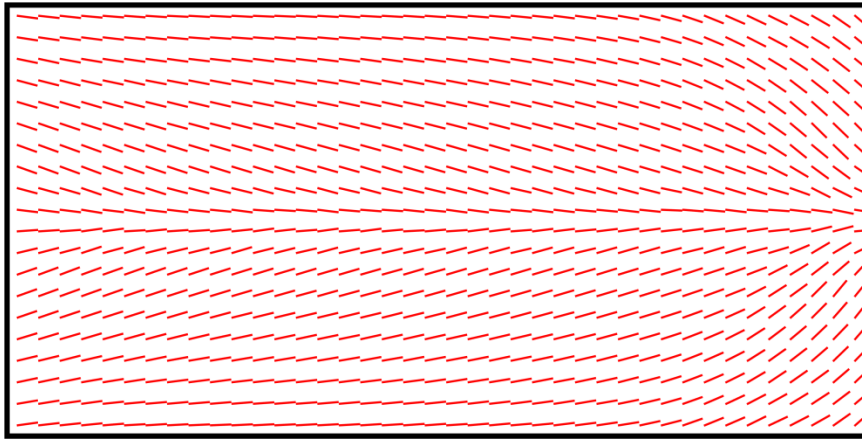


Fig. 3.14 Converged solution of the weighted load path method using fiber filtering.

The filtering scheme successfully dealt with fiber discontinuities in the corners. Additionally, problems with the previous designs, such as the cross-thatched pattern for the energy method and the transition boundary for the dominant load path method, are eliminated. The convergence history for the five methods, with fiber filtering applied, are shown in Fig. 3.15. The solutions all converge and stabilize much faster than the unfiltered designs. Table 3.2 compares the converged compliance for the filtered designs with the initial 0-deg fiber layout. The filtered designs of the strain and dominant load path method achieve overall compliances similar to their unfiltered designs (21.08 and 21.55 for the strain method, 20.14 and 20.89 for the dominant load path method), but with faster convergence and improved fiber smoothness and continuity. The stress, energy, and dominant load path methods all see improved convergence speed and smoothness but their overall compliance increases to 27.5%, 30.5%, and 32.2% respectively, compared to the initial baseline design.

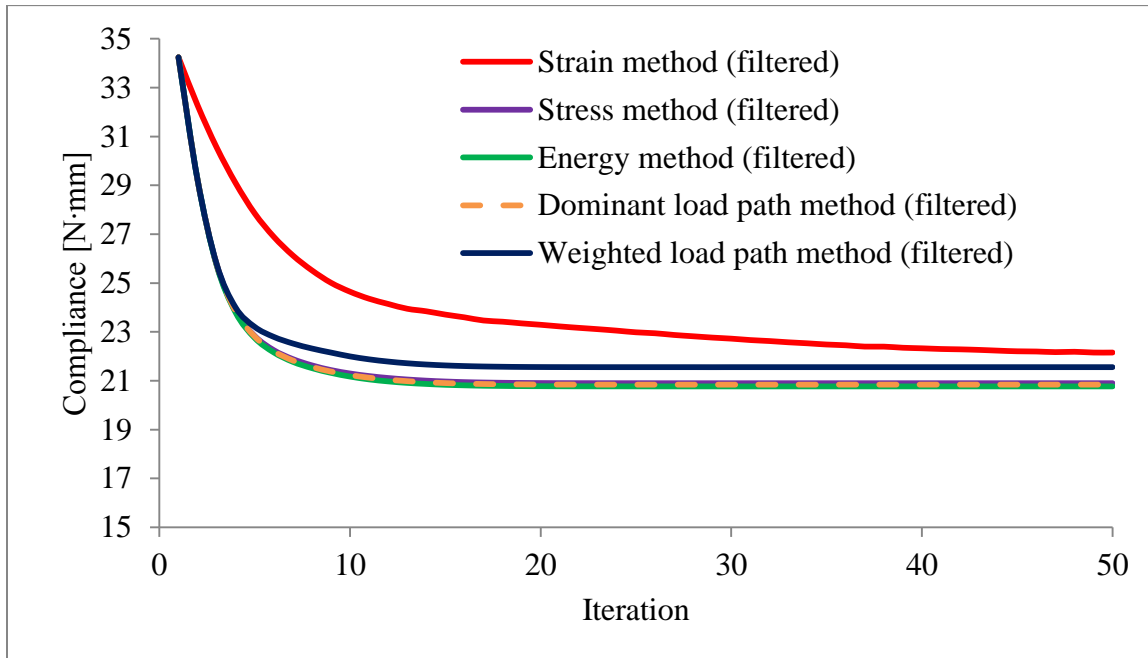


Fig. 3.15 Convergence history of the five methods using a filtering scheme.

Table 3.2 Comparison of the overall compliance of each solution using fiber filtering.

Method	Compliance	Percent Difference
Initial design (0 deg fiber)	34.24	
Strain (filtered)	21.55	-37.05
Stress (filtered)	20.84	-39.13
Energy (filtered)	20.76	-39.35
Dominant load path (filtered)	20.89	-38.97
Weighted load path (filtered)	22.15	-35.30

3.2.2. Pin-loaded plate

The next example is a pin loaded plate supporting a bearing load in plane-stress. Assume a rectangular plate with a hole, constrained on one end, and loaded on the interior edge of the hole in the opposite direction of the constraint (Fig. 3.16). The loading simulates the contact forces generated during a bearing load. The radial force

acting normal to the inside edge of the wall is represented as $F_r = F_0 \cos \theta$. The corresponding mesh is constructed manually using 2,128 QUAD4 elements (Fig. 3.17). The bearing load is applied to the nodes along the interior of the hole. The applied force, F_0 , is set at 100lb which produces a total x -dir load of 2,000 lb. The structure is modeled as a single lamina with the fiber angle open to design for each element. The orthotropic material selected has properties of $E_1 = 20 \times 10^6$ psi, $E_2 = 1.3 \times 10^6$ psi, $G_{12} = 0.6 \times 10^6$ psi, and a Poisson's ratio of 0.28. The lamina has a thickness of 0.125 in. The initialized design has all the fibers orientations aligned with the global x -dir. The initial compliance is measured at 8.694 lb·in.

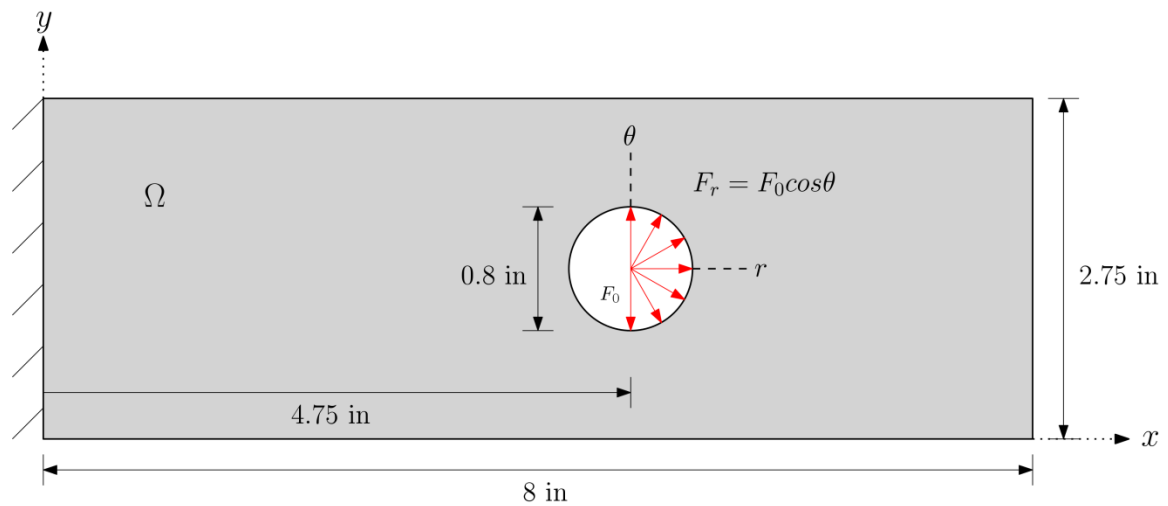


Fig. 3.16 Pin-loaded plate subjected to a bearing load on the interior edge of the hole.

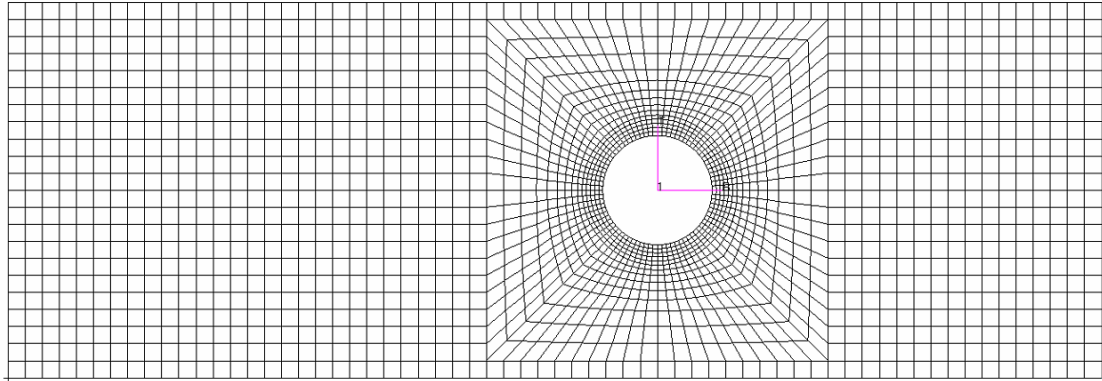


Fig. 3.17. FEM mesh consisting of 2,128 elements.

This example produces an interesting stress field that requires the structure to convert the applied force from compressive stress, to shear, then to tensile stress in order to support the loading. The elements adjacent to the bearing load (along the right side of the hole) experience large compressive stresses from the applied load. As the load transfers away from the hole, it transforms into shear stresses which allow the load flow to be turned back towards the constrained edge on the left-hand side. Once the load has been turned up and back over the hole, the stress field becomes tensile dominant as the load transits back to the constrained edge.

The five methods to determine fiber orientation are applied to this problem. The methods will be scored on their overall compliance, fiber smoothness, stability, and speed of convergence. Each method is run for 50 design iterations. Fig. 3.18 through Fig. 3.22 show the converged fiber orientations of the five methods.

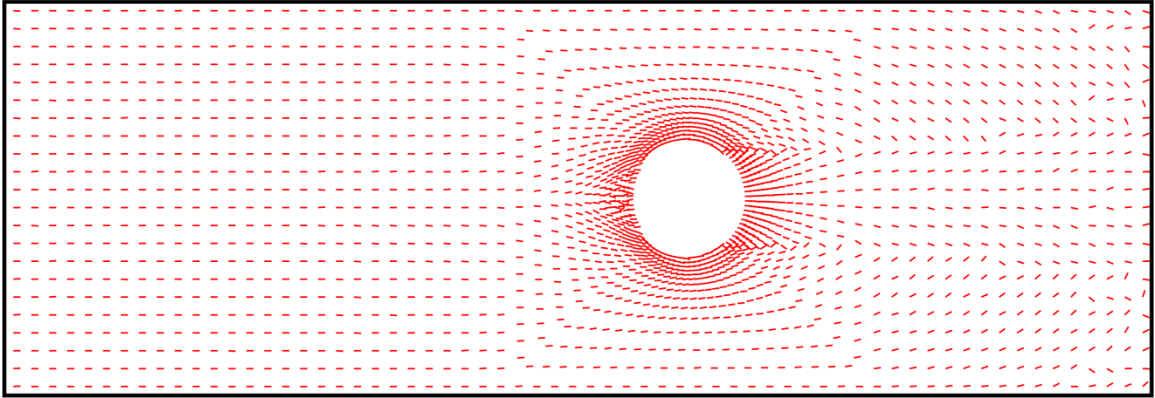


Fig. 3.18 Converged solution using the strain method.

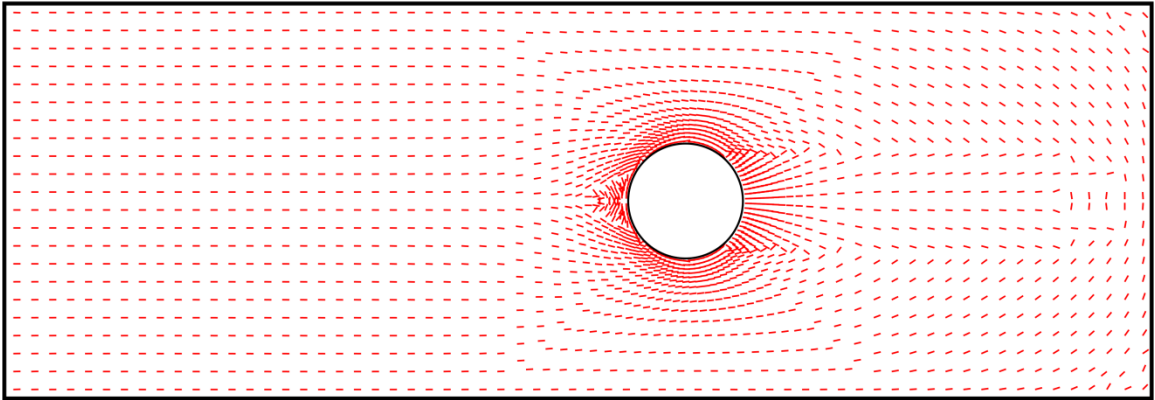


Fig. 3.19 Converged solution using the stress method.

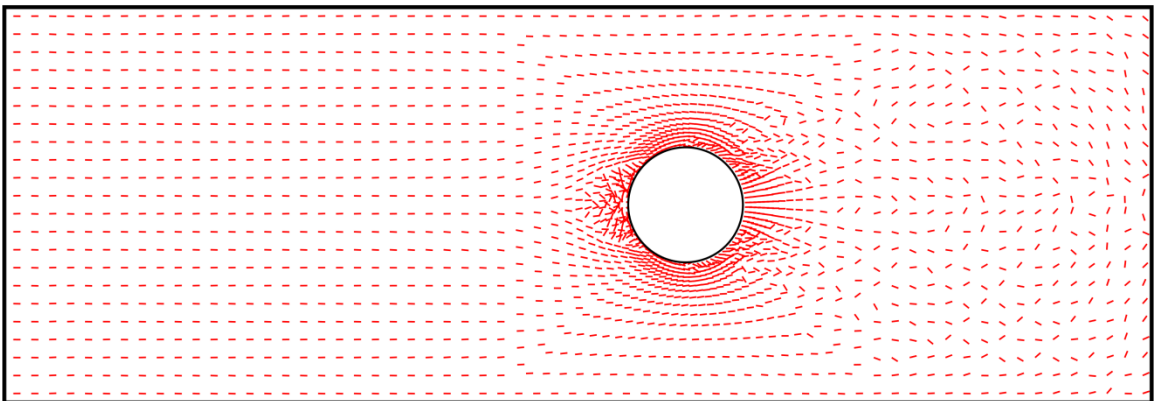


Fig. 3.20 Converged solution using the energy method.

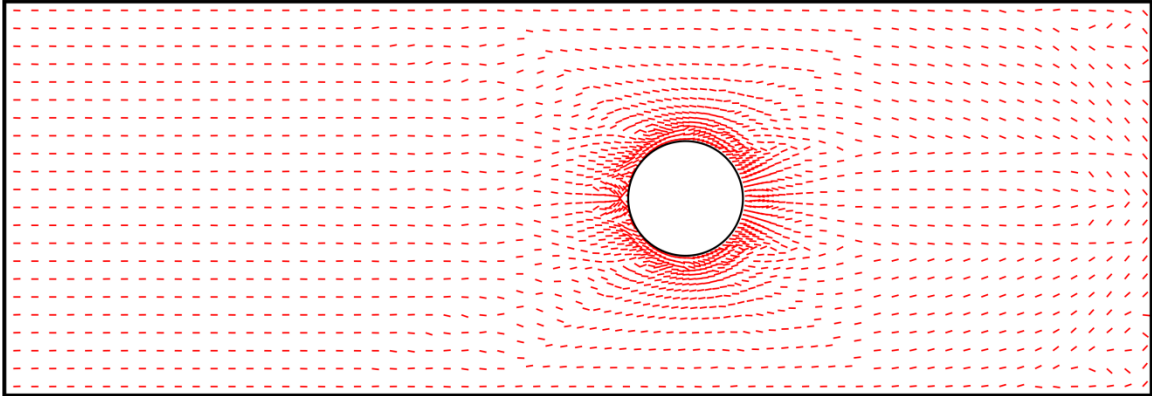


Fig. 3.21 Converged solution using the dominant load path method.

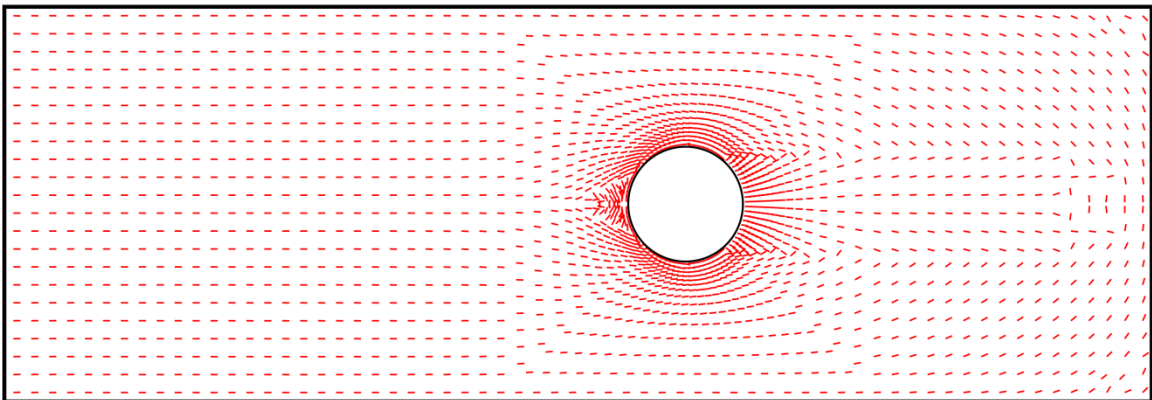


Fig. 3.22 Converged solution using the weighted load path method.

The examination of the fiber distributions of each method shows that the strain, stress, and dominant load path methods all produce stable solutions. The energy and weighted load path method show marginal convergence and their fiber distributions are unstable. Multiple attempts were made to stabilize the solution by adding fiber filters and by lowering the $\Delta\theta$, but the instability remained. The solutions for the strain, stress, and dominant load path methods were smooth and stable enough that the fiber trajectories could be plotted. Fig. 3.23 through Fig. 3.25 show the fiber paths of the three stable solutions. Fibers paths are initialized at the constrained edge on the left side of the plate.

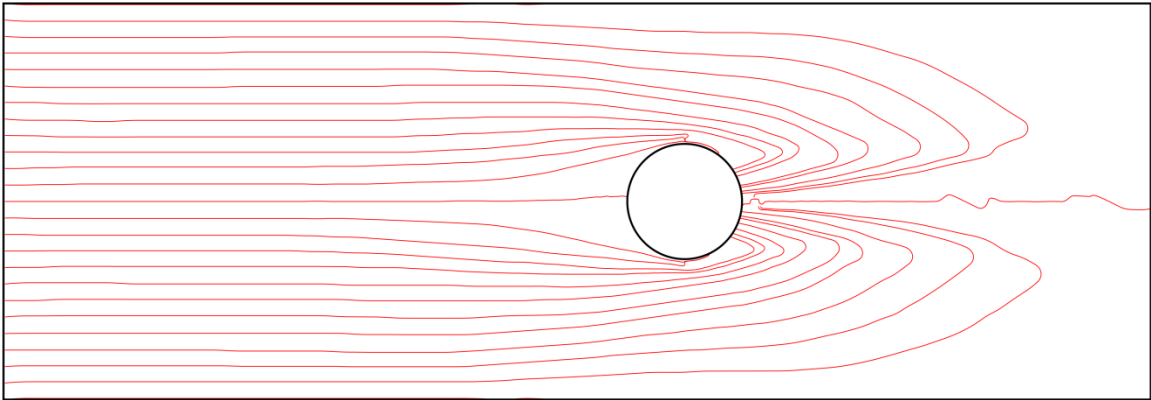


Fig. 3.23 Stable solution using the strain method showing the fiber trajectories.

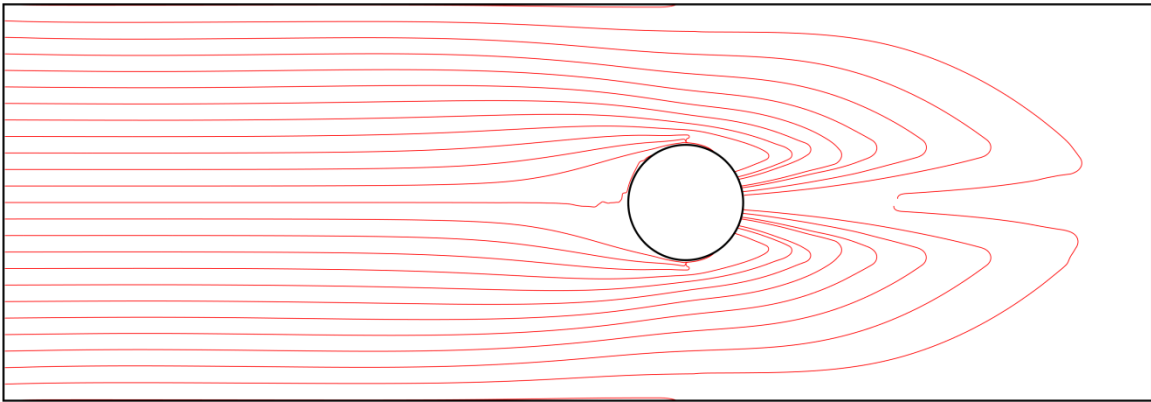


Fig. 3.24 Stable solution using the stress method showing the fiber trajectories.

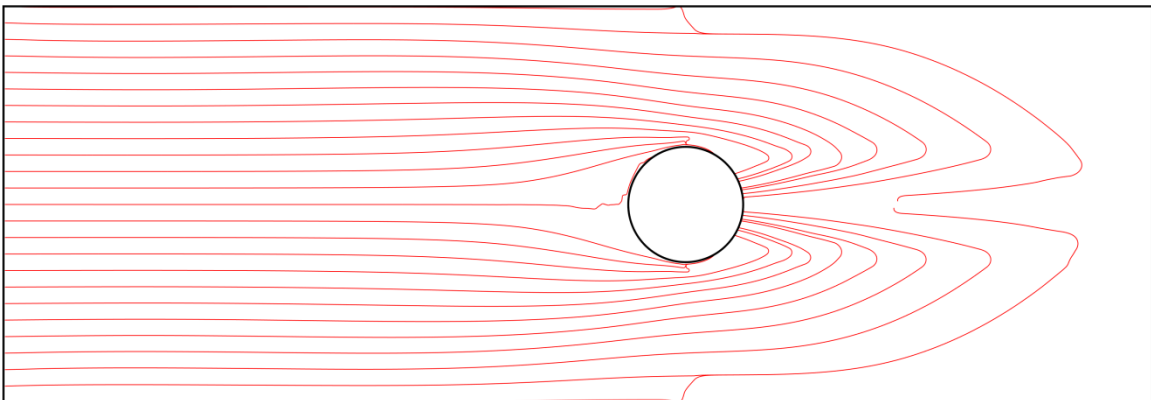


Fig. 3.25 Stable solution using the dominant load path method showing the fiber trajectories.

The convergence history for each method is presented in Fig. 3.26. The stress and dominant load path methods follow a similar convergence even though their converged orientations are different. The strain method converges at a slightly slower rate because the $\Delta\theta$ required for stability was smaller than the previous two methods. Table 3.3 shows the overall compliances of the converged solutions compared to the initial design. The stress and dominant load path methods record the highest reduction in compliance at 39.19% and 39.21%, respectively. The strain, stress, and dominant load path solutions all produce smooth and continuous fiber orientations without any filtering required.

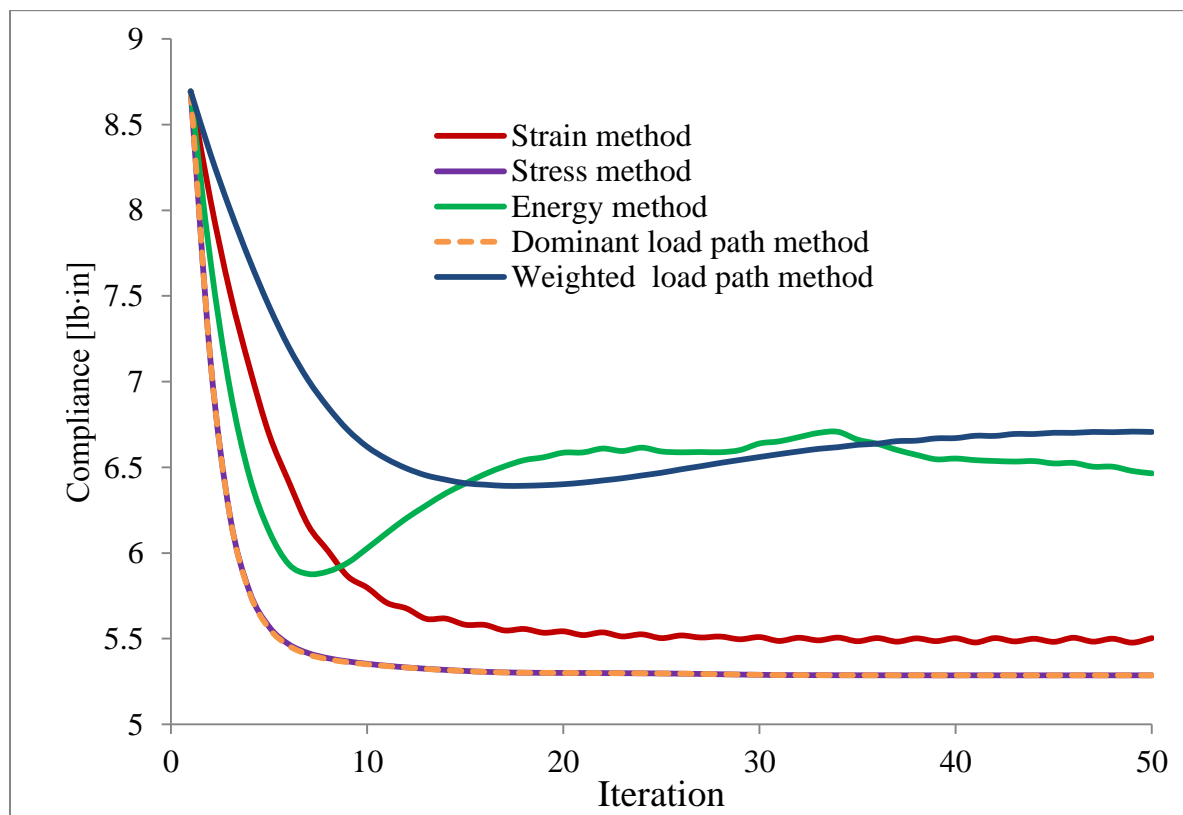


Fig. 3.26 Convergence history of the five solution methods.

Table 3.3 Comparison of the overall compliance of the converged solutions.

Method	Compliance	Percent Difference
Initial design	8.694	
Strain	5.503	-36.69
Stress	5.286	-39.19
Energy	6.465	-25.64
Dominant load path	5.286	-39.21
Weighted load path	6.706	-22.86

3.2.3. Fighter wing under aerodynamic load

The last example shows the application of Eq.(46) to a bending problem. The previous methods discussed cannot be applied to bending because the stress varies with thickness. However, by using the transverse shear force resultants, and solving for the z -direction load path function, Ψ_z , the fiber orientations can be determined. This requires solving Eq.(6) during each iteration.

Assume a generic low-aspect ratio fighter jet wing planform subjected to an aerodynamic pressure, C_p . Fig. 3.27 shows the dimensions on the wing planform which are consistent with an F-16 fighter aircraft. The wing root is assumed to be fully clamped to the aircraft's fuselage. Fig. 3.28 shows the aerodynamic pressure distribution found using the commercial vortex-lattice software, VLAERO. The aerodynamic solution is at an angle of attack, α , of 1 degree and at Mach number of 0.8. The airfoil used for analysis is a NACA 64A204 (Entsminger, Gallagher, & Graf, 2004).

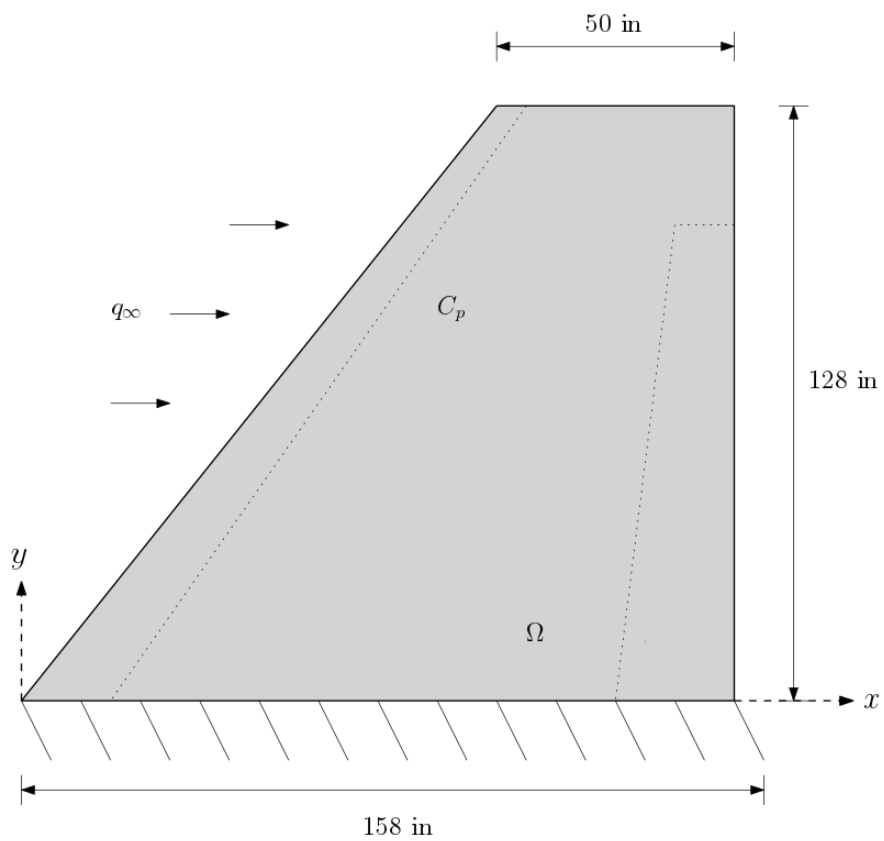


Fig. 3.27 Wing planform geometry and dimensions.

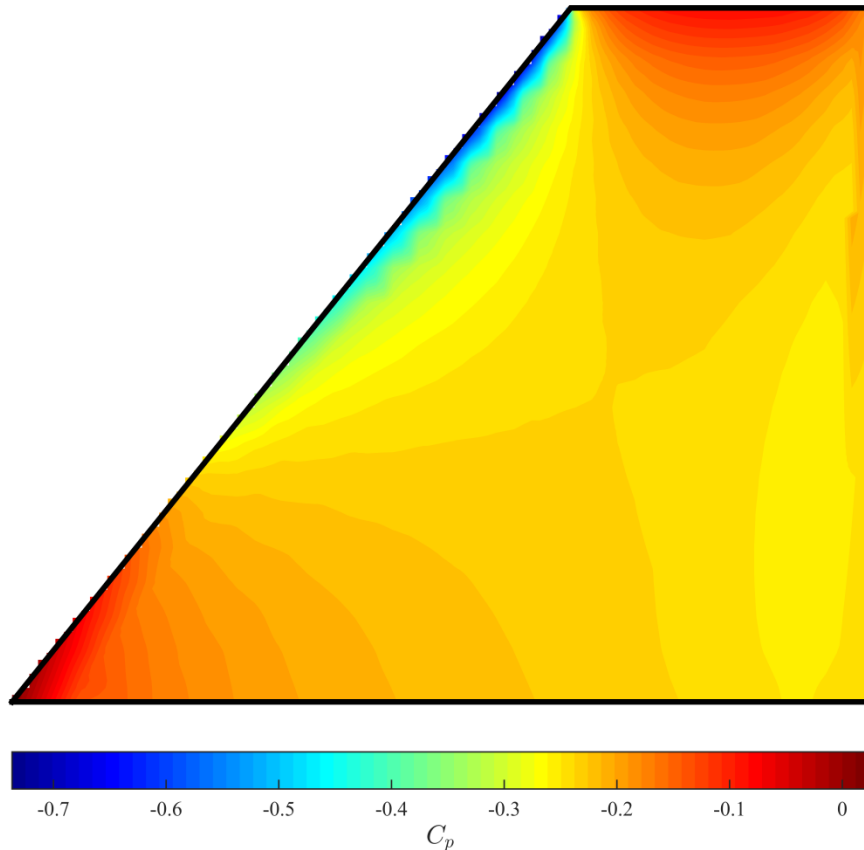


Fig. 3.28 Aerodynamic pressure distribution at $\alpha = 1$ deg and Mach 0.8.

Structurally, the wing is modeled as a flat plate, comprised of a single lamina of orthotropic material with a thickness of 0.5 in. Fig. 3.29 shows the FEM mesh using 2,194 QUAD4 elements. The orthotropic material selected has $E_1 = 20 \times 10^6$ psi, $E_2 = 1.3 \times 10^6$ psi, $G_{12} = 0.6 \times 10^6$ psi, and a Poisson's ratio of 0.28. The initialized design has all the fibers orientations aligned with the global y-dir. The compliance of the initial design is 30488 lb·in. Optimized fiber orientations are found using Eq.(46). Fig. 3.30 shows the initial fiber design, with all the fiber orientations in the global y-dir, and the contours of the corresponding load path function Ψ_z . Fig. 3.31 shows the fiber orientations after 50 design iterations with the corresponding load path function contours. A $\Delta\theta$ of 1 degree was selected and a fiber filter of 15in was applied to attempt solution

stability and convergence.

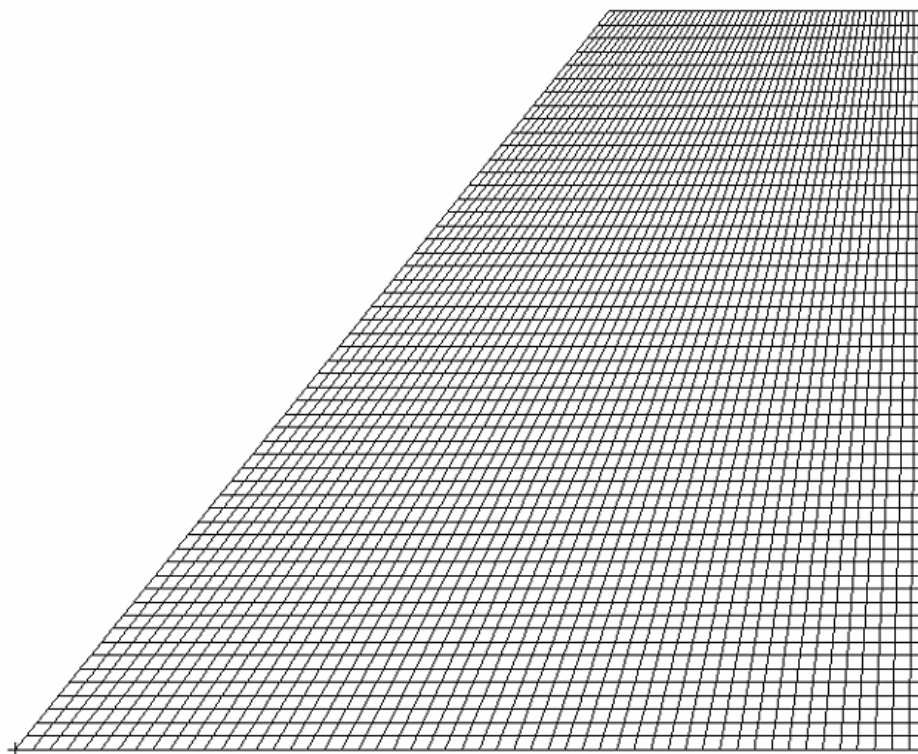


Fig. 3.29 FEM mesh comprised of 2,194 elements.

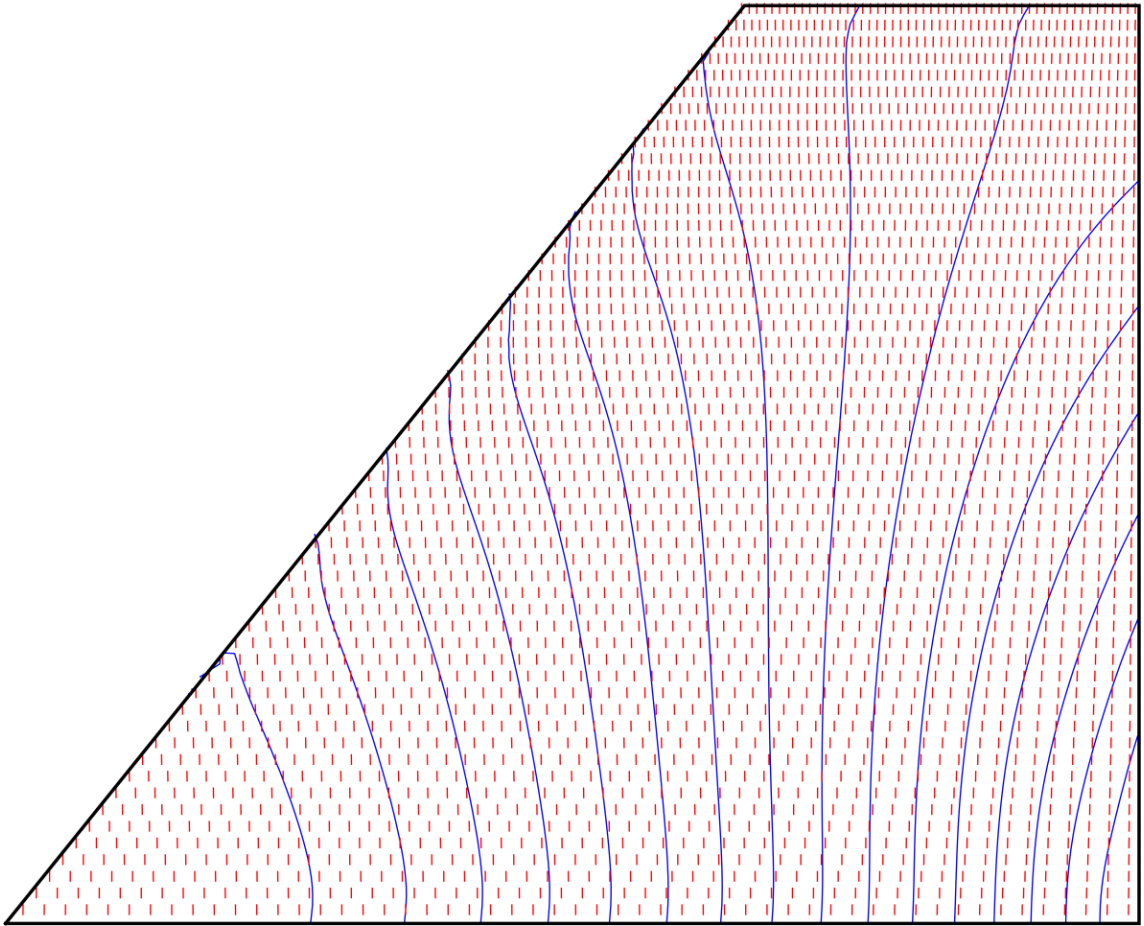


Fig. 3.30 Initial fiber design showing elemental fiber angles (red) and load function contours (blue).

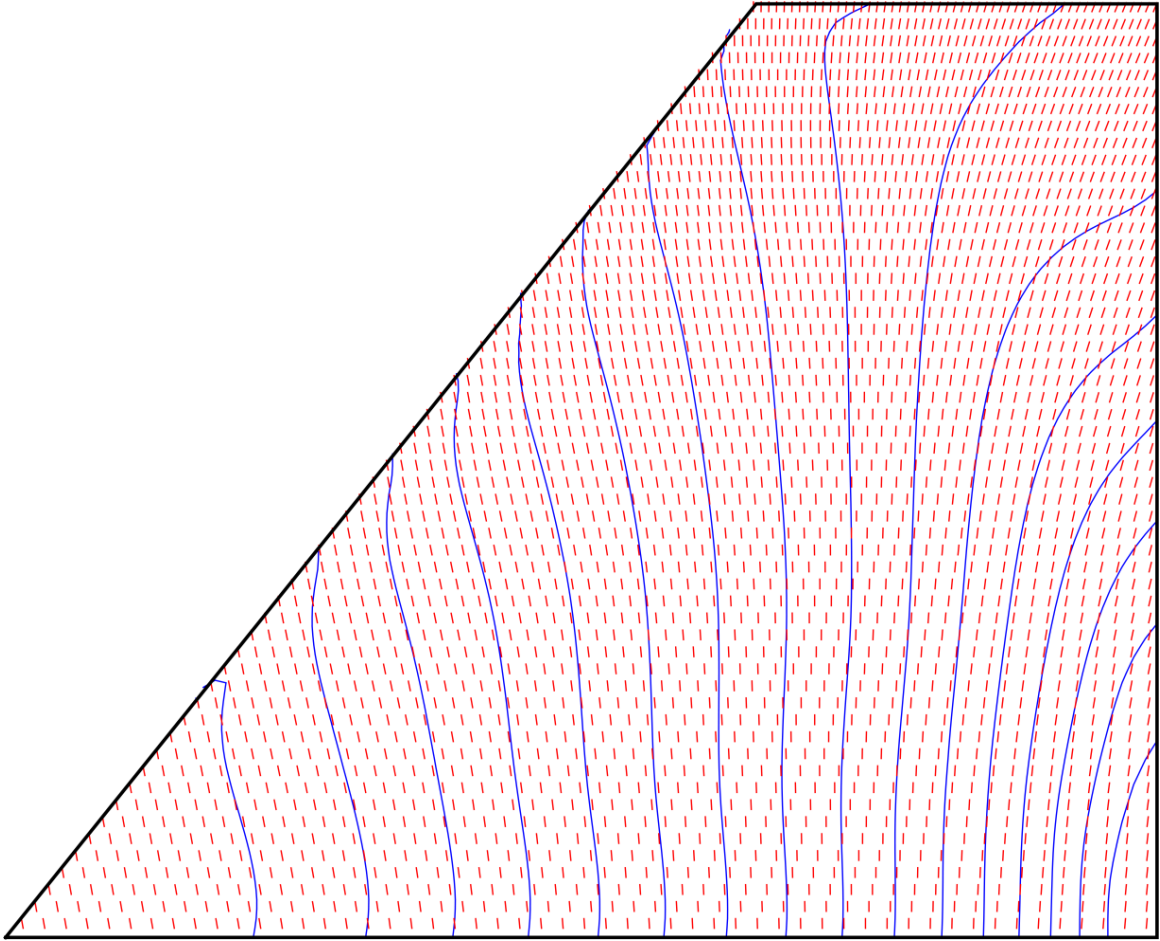


Fig. 3.31 Converged fiber design showing elemental fiber angles (red) and load function contours (blue).

The convergence history is shown in Fig. 3.32. A small $\Delta\theta$ and fiber filtering were implemented to aid stability and convergence due to the implicit nature between the load paths and the fiber orientations. Even with the mentioned implementations the convergence history demonstrates marginal solution stability. The converged design in Fig. 3.31 demonstrates how the fibers attempt to follow the z -dir load function contours. This is so that the stiffest direction of the orthotropic material is aligned with the direction of load transfer of the transverse shear forces. Table 3.4 shows the comparison between the initial design compliance and the optimized solution. Application of Eq.(46) to this design problem produces a 2.68% reduction (occurs at iteration 29) in overall compliance compared to using a constant-stiffness design.

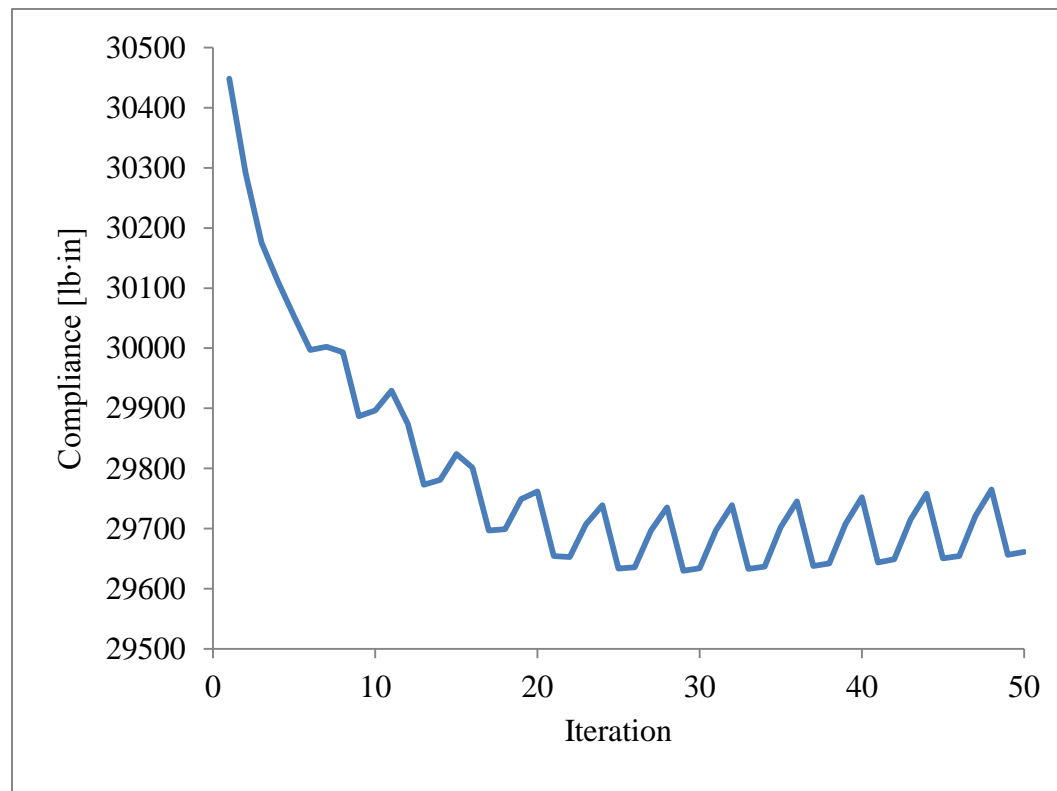


Fig. 3.32 Convergence history of the solution method showing marginal stability after 10 iterations.

Table 3.4 Comparing the compliance between the initial and final design.

Method	Compliance	Percent Difference
Initial design	30448	
Load path function method	29629	-2.68

3.3. Discussion

The purpose of this section is to investigate the problem of optimized orientations for orthotropic material. The strain method, stress method, and energy method are compared to the proposed load path methods to determine optimized orientations. Numerical analysis shows that for a plane-stress problem, no single method consistently produces superior results. The best designs for the shear-loaded plate were found using the energy, stress, and weighted load path method, in that order. The best designs for the pin-loaded plate were found using the stress method and the dominant load path method.

The classical methods use the stress and strains of each element to determine orientation. They are not applicable to bending problems where the stress and strain vary with thickness. Application of the load path function method to a bending problem successfully produces a reduction in overall compliance of the structure. However, this method can be unstable without proper fiber filtering. The minimal reduction in compliance for the bending example suggests that variable stiffness composites are more suitable for plane-stress applications where the reductions in compliance tend to be larger.

4. CONSIDERATIONS FOR 3D PRINTED COMPOSITES

Off-the-shelf CFRP printers, such as the MarkForged MKII printer, can combine the rapid prototyping capabilities of standard ABS plastic printers with the structural performance of CFRP composites. The printer can produce parts with a nylon matrix reinforced with either carbon, Kevlar®, or fiberglass fiber tows (MarkForged, 2016). The machine allows for continuous tows of fiber to be laid down along prescribed trajectories and geometries. In collaboration with University of New Mexico's (UNM) Advanced Structural and Energy Materials Lab (ASEMlab), the structural limitations of 3D printed composite parts were investigated. This includes material and failure testing (performed by ASEMlab) and FEM modeling performed at Embry-Riddle Aeronautical University's (ERAU) Structural Analysis and Design Laboratory (SAnD). The parts analyzed were standard ASTM D638-14/Type 1 and Type 4 printed specimens using concentric rings of fiber (Fig. 4.1). The findings were compared to the data published by the MarkForged company. This section will present the FEM framework used to model these structures and the failure comparisons to material testing.



Fig. 4.1 Part printed at ASTM D638-14 Type 4 standard used for tensile testing.

4.1. Modeling

The FEA model was based off the geometry and fiber layout given by the MarkForged software suite, shown in Fig. 4.2(a). In contrast to traditional, constant stiffness composites, where fibers are aligned in one direction, fibers in 3D printed parts can be curved. The MarkForged software, in particular, tends to print fibers in concentric rings, starting from the center and working to the perimeter of the part. Composites with curvilinear fibers can be difficult to model because the fiber angle varies from element to element; therefore, the material properties vary as function of position in the structure. Generating individual material and laminate properties for each element would be a laborious and time-consuming task for an individual to perform manually in a FEM graphical user interface. This led to the development of an automated modeling system using Matlab/Python and Patran.

A Matlab/Python script was written to model, mesh, and generate laminate properties for different sets of ASTM D638-14/Type 1 and Type 4 printed parts. Fig. 4.2(b) shows the finite element mesh used to describe the geometry of a Type 4 printed part. It was found from previous design iterations that variable stiffness composites are extremely sensitive to mesh smoothness. Therefore, the bands of curved fibers along the part's perimeter are meshed with their own smooth bands of elements. Two different material properties are introduced: the first describes the carbon reinforced composite used throughout the majority of the structure; the second is an isotropic material that describes the small pockets of nylon which are used by the 3D printer to fill in areas where the carbon fiber filaments cannot be easily placed. Fig. 4.2(c) depicts in red the regions of the model that use the nylon filler material.

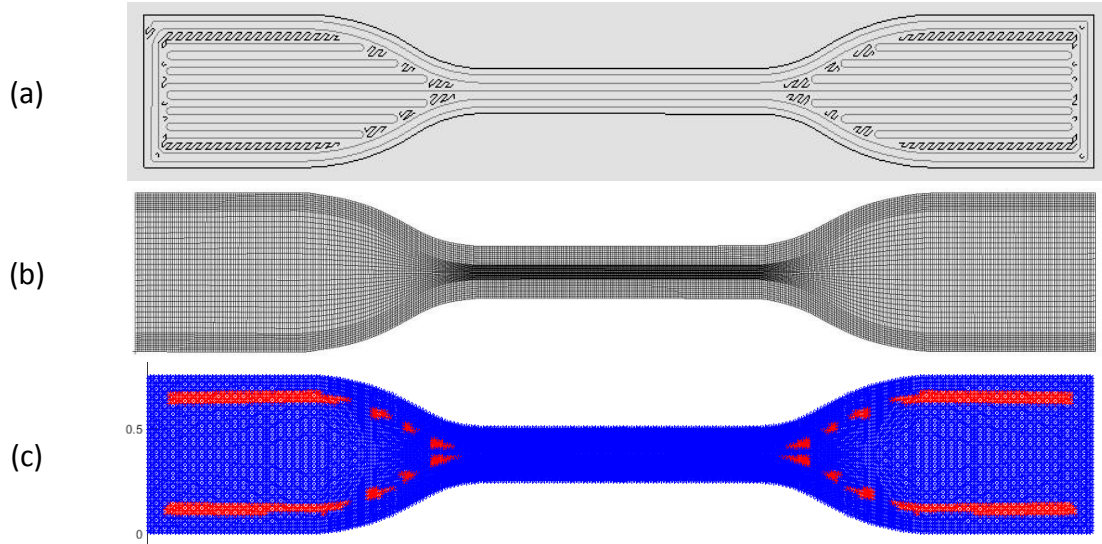


Fig. 4.2 a) Geometry and fiber layout of an ASTM D638-14/Type 4 3D printed part, b) Finite element mesh using CQUAD4 shell elements, c) The regions depicted in red specify areas of the part with only nylon filler material.

The printed specimens were tested in tension with grips attached to the wide flanges at the ends. Rigid Body Elements (RBE2) were used in FEM to simulate this load scenario by “clamping” the tabs at each end. Material properties for each element are derived from the local fiber angle of the printed part at each element’s location. By overlaying the element centroids over the digitized fiber data, the local material orientations for each element can be determined from interpolation. Fig. 4.3 shows the local fiber orientations mapped onto the centroid of each element. Additionally, the elements of the model that are located in the regions of the nylon filler material were assigned separate material properties and represented in the figure with black circles.

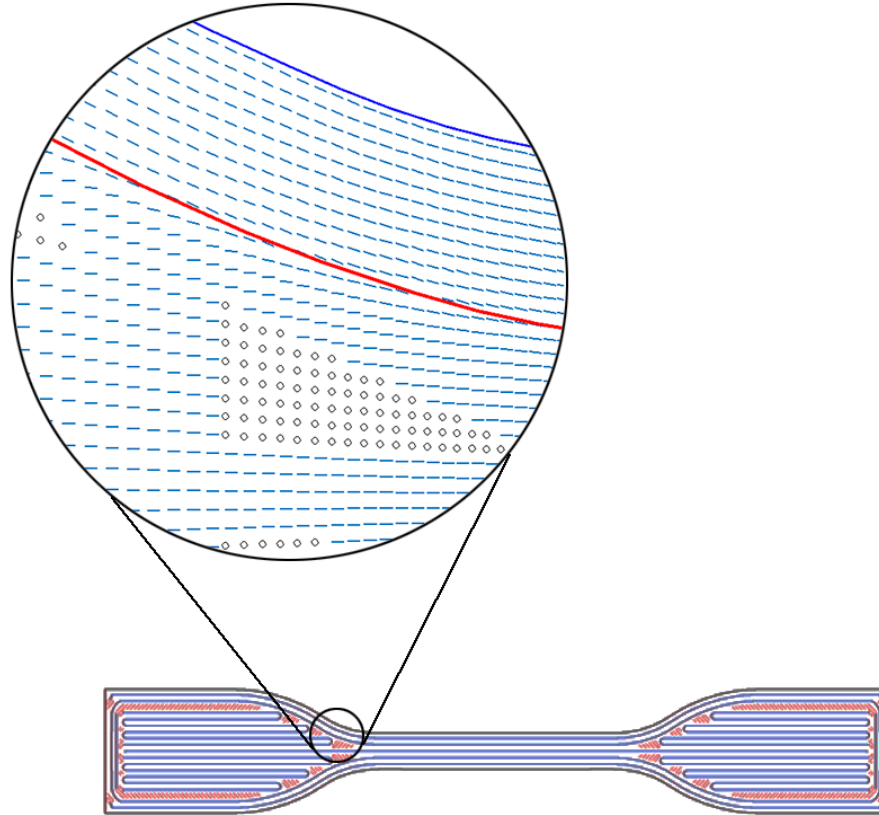


Fig. 4.3 The fiber orientation angles mapped onto the centroids of each element.

4.2. Results

The material stiffness and failure values were taken from the Markforged data sheet and are presented in Table 4.1. The material properties selected for the nylon filler regions follow the standard Nylon-6 material properties.

Table 4.1 Material data for the carbon fiber reinforced and nylon regions

	Carbon fiber composite	Nylon
E_1	50.0 GPa	0.94 GPa
E_2	4.0 GPa	0.94 GPa
G_{12}	2.0 GPa	0.34 GPa
ν_{12}	0.33	0.4
σ_1^T	700.0 MPa	53.8 MPa
σ_1^C	-320.0 MPa	-53.8 MPa
σ_2^T	48.0 MPa	53.8 MPa
σ_2^C	-100.0 MPa	-53.8 MPa
τ_{12}	73.0 MPa	68.9 MPa

The fiber direction normal stress for the ASTM D638-14/Type 4 sample at the failure load are shown in Fig. 4.4. Using Fig. 4.2(a) as a reference, it can be seen that the maximum normal stress occurs in the single band of fiber that runs through the center of part. Because the nylon is experiencing little stress at the neck, we can conclude that the load is being transferred solely through the fibers and bypassing the filler regions altogether. Fig. 4.5 shows the fiber direction shear stresses. The maximum shear stresses occur in the neck along the boundary between the nylon and composite regions.

The failure is predicted using Tsai-Wu failure theory. Fig. 4.6 shows the indices at failure for the part. The failure location is predicted in the neck region along the seam between the composite and nylon regions.

Table 4.2 shows the corresponding stresses at the failure location. The stresses at the failure location suggest failure due to a combination of high stresses perpendicular to the fiber direction and high shear stresses. This agrees with the tensile test results in Fig. 4.7 which shows failure in the same location. We can conclude from FEM that matrix failure was likely initiated due to an overload of shear stresses. Additionally, the σ_2

stresses in the same location led to disbonding of the composite from the nylon filler triggering a longitudinal crack along the axis of the part. At this failure load, the average normal stress at the gage is 223 MPa.

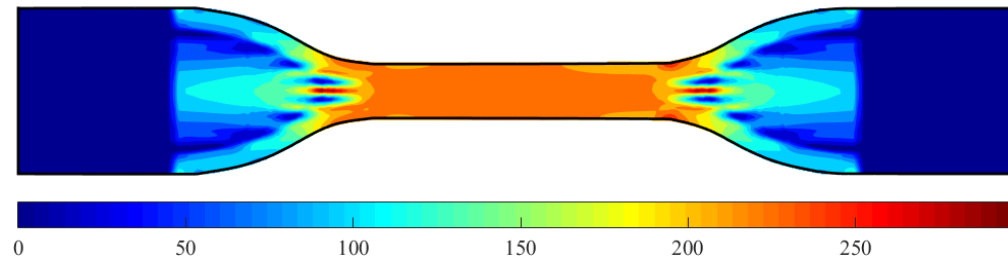


Fig. 4.4 σ_1 normal stress [MPa] at failure load

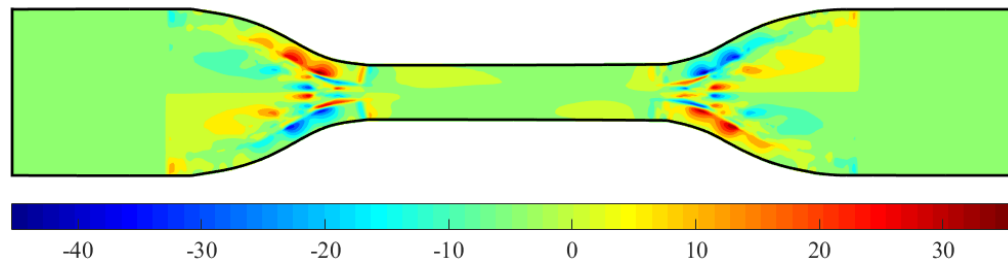


Fig. 4.5 τ_{12} shear stress [MPa] at failure load

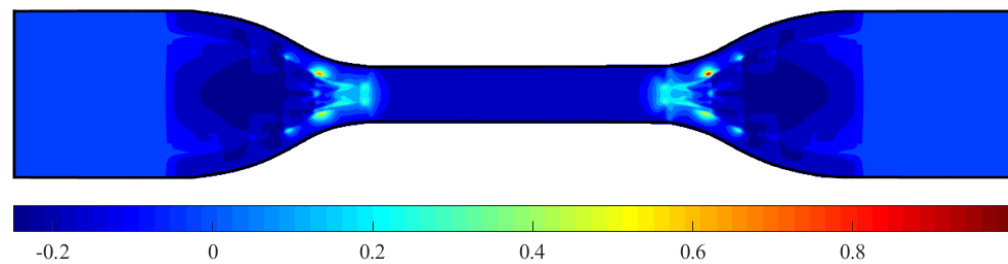


Fig. 4.6 Tsai-Wu failure indices for the Type 4 model at failure load.



Fig. 4.7 Fractured sample exhibiting matrix failure. Box contains longitudinal matrix crack and arrows point to crack initiation points.

Table 4.2 FEA failure stresses for the Type 4 model

FEA	Gage normal stress [MPa]		Failure location FEA stresses [MPa]		
	Experimental	% Difference	σ_1	σ_2	τ_{12}
226	223±9	1.3 ± 2.0 %	222	34.6	-37.8

Models of the ASTM D638 – 14 Type 1 specimens, with varying numbers of concentric rings, were also analyzed and compared with tensile testing. The total number of printed layers for all samples was 24 layers. All layers were reinforced with either 2, 3, 4, 5 or 6 rings of concentric fiber. Table 4.3 shows the relationship between the number of concentric rings and the total fiber volume fraction. The fiber direction normal stresses and shear stresses for the Type 1 model are shown in Fig. 4.8 and Fig. 4.9 at the resulting failure load. The largest normal stresses occur in the interior of the part at the transition between the neck and flange. The largest shear stresses occur in the same region, except slightly further inwards from the boundary between nylon and composite. The resulting Tsai-Wu failure indices are shown in Fig. 4.10. Inspection of the failure indices shows that failure is occurring within the structure, at the location of peak shear stress. The tensile strength in comparison with experimental testing is reported in Fig. 4.11.

Table 4.3. Relationship between number of concentric rings and total fiber volume fraction.

Number of concentric rings	Total fiber volume fraction
2	10
3	15
4	20
5	25
6	30

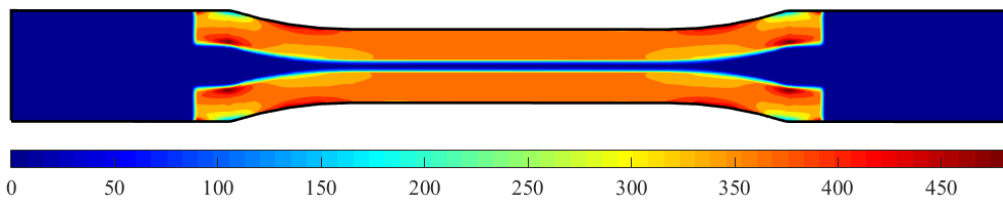


Fig. 4.8 σ_1 normal stress [MPa] at failure load for with 6 concentric rings ($V_f=0.3$)

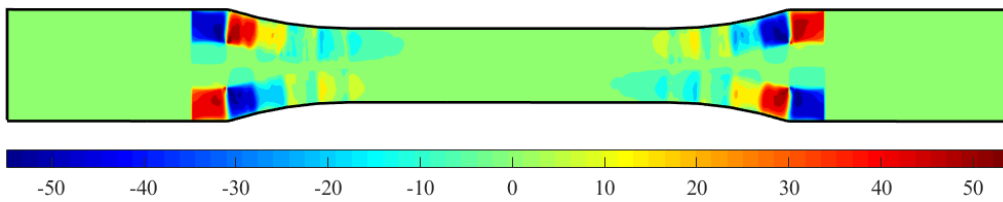


Fig. 4.9 τ_{12} shear stress [MPa] at failure load for with 6 concentric rings ($V_f=0.3$)

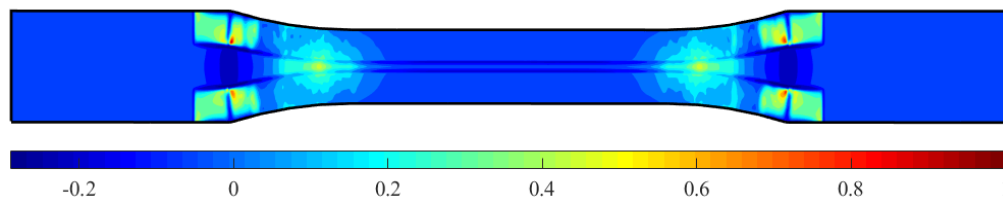


Fig. 4.10 Tsai-Wu failure indices for the Type 1 model at failure load.

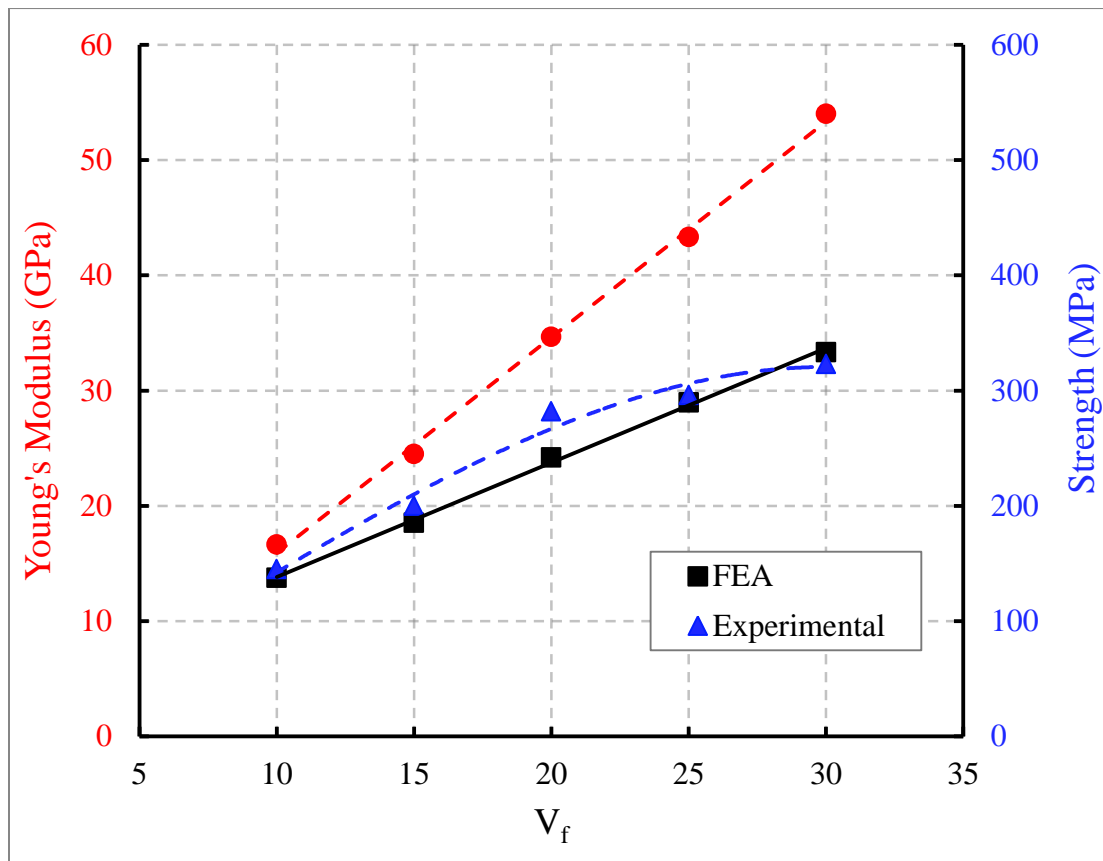


Fig. 4.11 Tensile elastic modulus and strength of specimens as a function of total carbon fiber volume fraction.

Individual analyses were performed for each set of concentric rings, which varied from two to six. The strength improved linearly as the amount of fiber increased. However, the normal and shear stresses varied. As the amount of fiber increased, the maximum shear stresses increased and the maximum normal stresses decreased, as described in Fig. 4.13. Models with five and six rings (corresponding to $V_f = 0.25$ and 0.3) have a much larger component of shear stress at the failure location than parts with less rings, which have a larger component of normal stress at the same location. A comparison of stress distributions between $V_f = 0.15$ and 0.3 , for the σ_1 normal stress and

the τ_{12} shear stress, is presented in Fig. 4.12. During tensile testing it was reported that all parts exhibited fiber failure, with the five and six ring parts showing a combination of fiber and matrix failure. The FEM partially confirms this result.

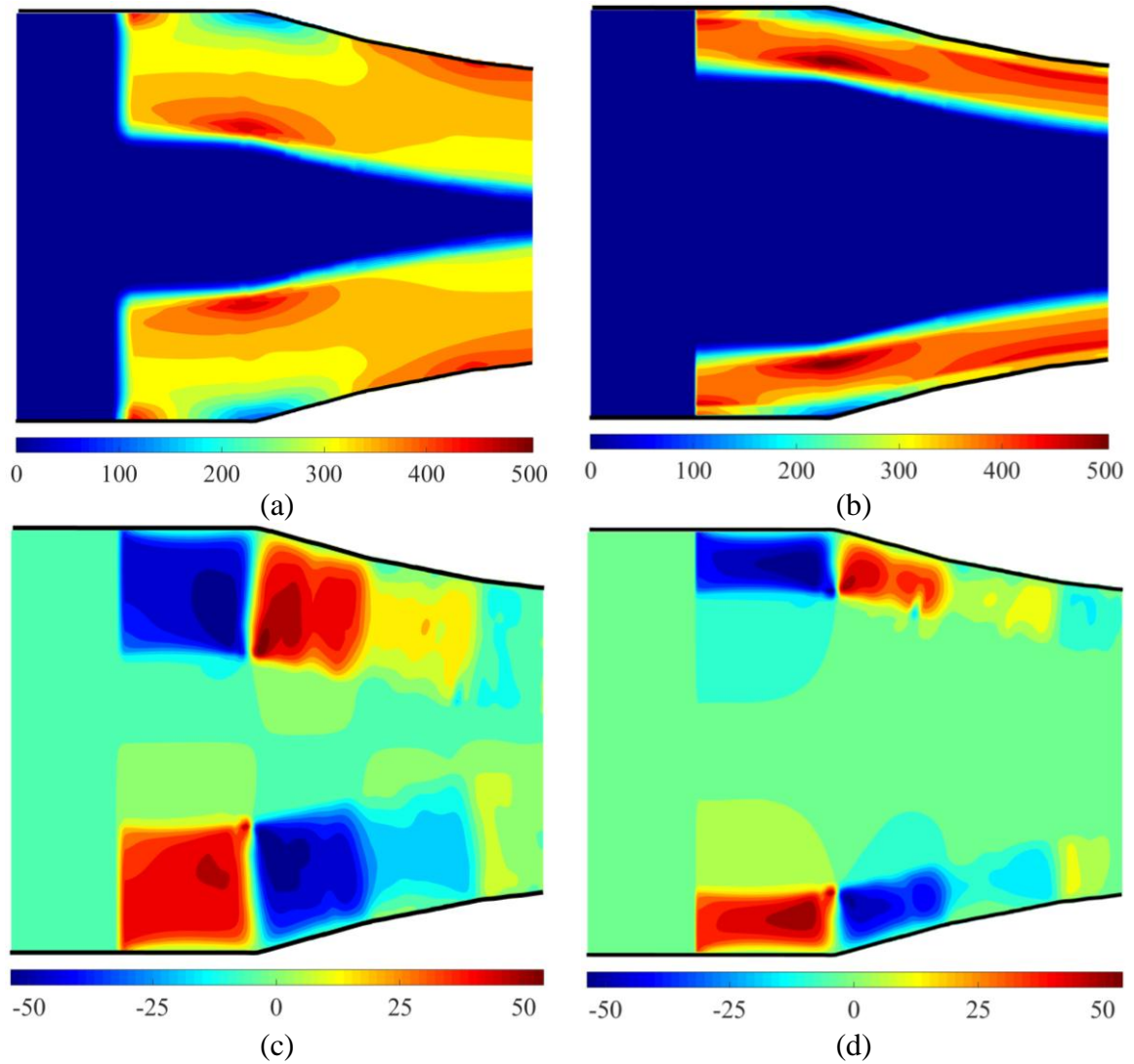


Fig. 4.12 Comparison of failure stresses at different fiber volume fraction, a) σ_1 [MPa] for $V_f=0.3$, b) σ_1 [MPa] for $V_f=0.15$, c) τ_{12} [MPa] for $V_f=0.3$, d) τ_{12} [MPa] for $V_f=$

0.15.

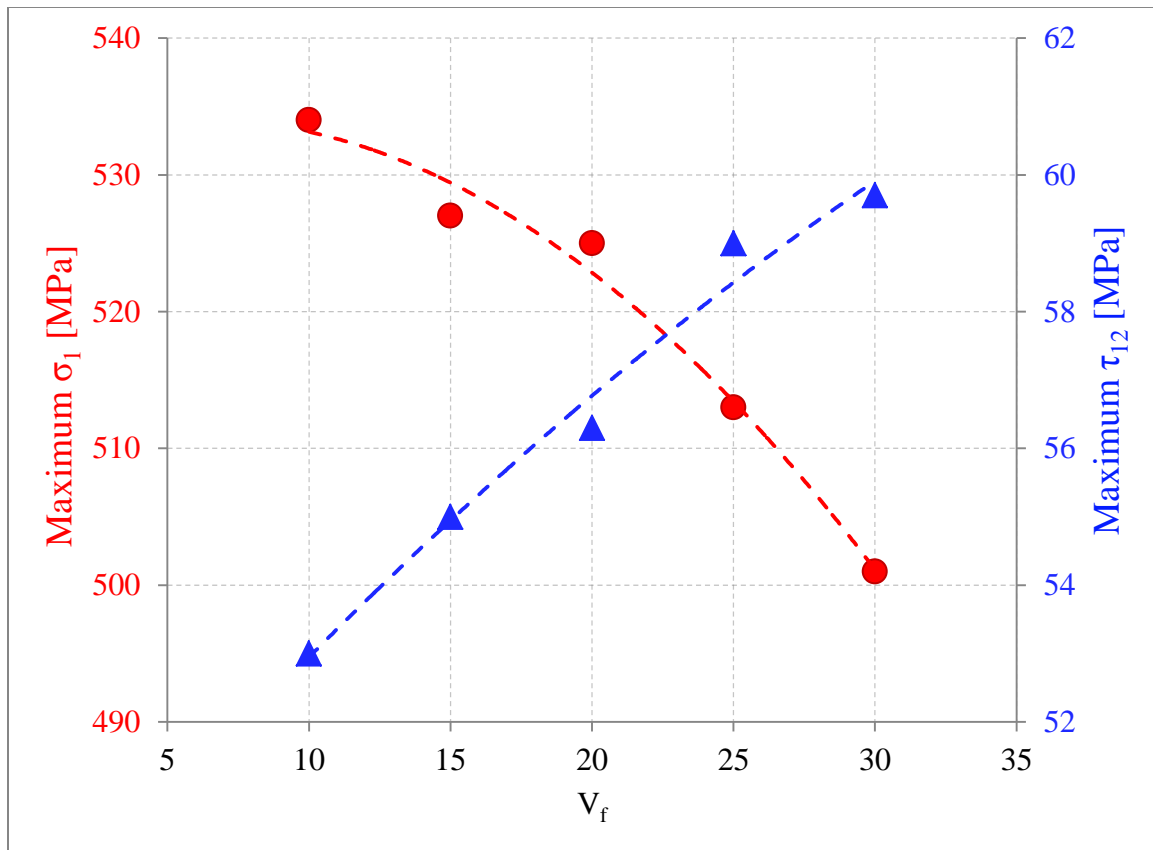


Fig. 4.13 The relationship between the maximum stresses at failure and the total fiber volume fraction.

4.3. Discussion

Regardless of the number of fiber rings, the failure location for all the Type 1 models occurred in the composite at the transition between the neck and flange, near the boundary between the nylon filler and the composite. This contrasts with the Type 4 model in three notable ways. First, the failure occurs far from the gage and closer to the point of load application at the grips where the part has a larger cross-sectional area. Second, the failure is occurring approximately 0.75mm outwards from the boundary between the composite and nylon, which suggests fiber failure. The Type 4 model failed directly along the seam between the two materials which resulted from matrix failure.

Third, for the Type 1 model, the σ_2 stress is minimal and contained inside the nylon filler regions. Therefore, the failure is dictated solely by the σ_1 and τ_{12} stress in the composite. This contrasts with the Type 4 model, which saw large multiaxial stresses in the composite at the failure location.

The FEA of the ASTM D638 – 14 Type 1 and Type 4 models exhibit the sensitive nature of 3D-printed, variable stiffness composites. With a constant stiffness composite, or an isotropic material, the geometry of the structure solely governs the location of the failure, which usually occurs at the outer edge of a geometric feature. It is shown from FEA that implementing variable stiffness composites, while using the same geometry, can lead to counter intuitive failure locations, including failures from within the part that propagate outward. This demonstrates the importance of including FEA in the design of any 3D printed composite that is being designed as a structural component. The observations from different tests and the numerical simulations confirmed that it is not possible to prepare sufficiently strong parts using the MarkForged 3D printer without prior knowledge of the effect of geometry over the failure modes which could only be obtained using FEM simulations.

5. CONCLUSION

The design, optimization, and analysis of variable stiffness composites were investigated. A new method to determine optimized fiber orientation of orthotropic material was derived based upon the theory of structural load paths. This methodology was compared against other classic methods using a set of bench mark examples.

The load path function method was expanded upon to include the capability to determine load paths when non-conservative body loads are acting on the structure. This was done by decomposing the stress field into two components, a self-equilibrated component and a body force component. The load path function was assumed to be a function of the self-equilibrated stress components only. Additionally, the load path function method was also expanded to shell and membrane structures using stress functions and shell projections. Examples of the method showed its possible applications.

Next, structural load path determination was used as a basis for variable stiffness composite design where the curl of the load path function is used to determine local fiber orientation. Optimized designs for plane-stress problems using the load path function methods were compared with classical methods found in the literature. While no particular method proved superior for any given problem, the load path function methods did exhibit the capability to reduce the overall compliance by as much as 35% to 50%. An example showing the application of the load path function to a bending problem produced a slight improvement in overall compliance, but only marginal solution stability.

Lastly, the design considerations and limitations of 3D printed composite parts were explored. Finite element analyses, in conjunction with material testing perform at

the University of New Mexico's ASEMLab, showed how sensitive the strength of 3D printed composites can be to changes in orientation and geometry. The importance of utilizing the finite element method for analysis is demonstrated by the counterintuitive stress concentrations and internal failure that can occur in a variable stiffness composite design.

This research demonstrated the performance increases that can be achieved by using variable stiffness composites; however, no clear design methodology has proven to be superior for determining the minimum compliant design. The two primary hindrances were solution stability and fiber smoothness to facilitate manufacturing. Additionally, the strength of additively manufactured composite parts is difficult to predict and requires a detailed stress analysis to ensure the structure is performing as intended.

6. SUGGESTIONS FOR FUTURE WORK

The next phase in the design of optimized orthotropic materials should explore an extension to three-dimensional membrane problems. Three-dimensional shell problems could also be addressed, but optimizing variable stiffness designs subjected to bending needs further investigation and understanding. Buckling stability of composite panels is a critical criterion in aerospace design; therefore, optimizing for buckling performance is the next logical step. However, the underlying problems with solution stability and fiber smoothness will linger and the implicit nature of the solution method must be addressed.

Using load paths as a basis for fiber trajectories and topology optimization shows promise and needs continued investigation. Hamiltonian load paths, which are determined using the concept of minimum potential energy, also need to be explored further.

Discovering a method to bypass the MarkForged software suite so that custom G-code commands could be given to the MKII printer must be discussed for future research. This would allow the manufacture of low-cost, self-tailored, 3D printed composites in a desktop platform.

REFERENCES

- Brampton, C. J., *et al.* (2015). New optimization method for steered fiber composites using the level set method. *Structural and Multidisciplinary Optimization*, 52(3), 493-505.
- Cutri, M. T. (2015). Pier Luigi Nervi e l'architettura strutturale. Retrieved from <http://www.archidiap.com/opera/palazzetto-dello-sport/>
- Diaz, A., & Bendsøe, M. (1992). Shape optimization of structures for multiple loading conditions using a homogenization method. *Structural and Multidisciplinary Optimization*, 4(1), 17-22.
- Entsminger, A., *et al.* (2004). *General Dynamics F-16 Fighting Falcon*. Department of Aerospace and Ocean Engineering. Virginia Polytechnic Institute and State University.
- Gea, H., & Luo, J. (2004). On the stress-based and strain-based methods for predicting optimal orientation of orthotropic materials. *Structural and Multidisciplinary Optimization*, 26(3), 229-234.
- Ghista, D. N., & Resnikoff, M. M. (1968). Development of Michell minimum weight structures.
- Harasaki, H., & Arora, J. S. (2001). New concepts of transferred and potential transferred forces in structures. *Computer methods in applied mechanics and engineering*, 191(3), 385-406.
- Hemp, W. S. (1958). *Theory of structural design*. Retrieved from
- Hoogenboom, P. C. J. b17_handout_1.pdf. Retrieved from http://homepage.tudelft.nl/p3r3s/b17_handout_1.pdf
- Kelly, D., & Elsley, M. (1995). A procedure for determining load paths in elastic continua. *Engineering Computations*, 12(5), 415-424.
- Kelly, D., *et al.* (2011). On interpreting load paths and identifying a load bearing topology from finite element analysis. *Finite Elements in Analysis and Design*, 47(8), 867-876. doi:10.1016/j.finel.2011.03.007
- Kelly, D. W., *et al.* (2011). An algorithm for defining load paths and a load bearing topology in finite element analysis. *Engineering Computations*, 28(2), 196-214.
- Kiyono, C., *et al.* (2017). A novel fiber optimization method based on normal distribution function with continuously varying fiber path. *Composite structures*, 160, 503-515.
- Legrand, X., *et al.* (2006). Optimisation of fibre steering in composite laminates using a genetic algorithm. *Composite structures*, 75(1), 524-531.
- Li, R., *et al.* (2006). Improving the efficiency of fiber steered composite joints using load path trajectories. *Journal of composite materials*, 40(18), 1645-1658.
- Luo, J., & Gea, H. (1998). Optimal orientation of orthotropic materials using an energy based method. *Structural and Multidisciplinary Optimization*, 15(3), 230-236.
- Marhadi, K., & Venkataraman, S. (2009). Comparison of quantitative and qualitative information provided by different structural load path definitions. *International Journal for Simulation and Multidisciplinary Design Optimization*, 3(3), 384-400.
- MarkForged (Producer). (2016). MarkForged MKII Material Data Sheet. Retrieved from <http://www.markforged.com>
- Mazumdar, S. (2001). *Composites manufacturing: materials, product, and process*

engineering: CrC press.

- Ning, F., *et al.* (2015). Additive manufacturing of carbon fiber reinforced thermoplastic composites using fused deposition modeling. *Composites Part B: Engineering*, 80, 369-378.
- Park, K. Y., *et al.* (1995). Delamination-free and high efficiency drilling of carbon fiber reinforced plastics. *Journal of composite materials*, 29(15), 1988-2002.
- Pedersen, P. (1989). On optimal orientation of orthotropic materials. *Structural and Multidisciplinary Optimization*, 1(2), 101-106.
- Sakurai, T., *et al.* (2007). Reduction of calculation time for load path U* analysis of structures. *Journal of Solid Mechanics and Materials Engineering*, 1(11), 1322-1330.
- Santer, M., & Pellegrino, S. (2009). Topological optimization of compliant adaptive wing structure. *AIAA journal*, 47(3), 523.
- Setoodeh, S., *et al.* (2009). Design of variable-stiffness composite panels for maximum buckling load. *Composite structures*, 87(1), 109-117.
- Takahashi, K. (2001). *Conditions for desirable structures based on a concept of load transfer courses*. Paper presented at the Proceedings of the First International Structural Engineering and Construction Conference.
- Tamijani, A., & Gharibi, K. (2016). *Load paths visualization in plane elasticity using load path function method*.
- Thomsen, J. (1991). Optimization of composite discs. *Structural and Multidisciplinary Optimization*, 3(2), 89-98.
- Tosh, M., & Kelly, D. (2000). On the design, manufacture and testing of trajectorial fibre steering for carbon fibre composite laminates. *Composites part A: applied science and manufacturing*, 31(10), 1047-1060.
- Ugural, A. C. (2009). *Stresses in Beams, Plates, and Shells, Third Edition*: CRC Press.
- Venkataraman, S., *et al.* (2009). *Investigating Alternate Load Paths and Damage Tolerance of Structures Optimized for Multiple Load Cases*. Paper presented at the 50th AIAA/ASME/ASCE/AHS/ASC Structures, Structural Dynamics, and Materials Conference 17th AIAA/ASME/AHS Adaptive Structures Conference 11th AIAA No.
- Waldman, W., *et al.* (2002). Advances in two-dimensional structural loadflow visualisation. *Engineering Computations*, 19(3), 305-326.
- Wu, K. C. (2008). Design and analysis of tow-steered composite shells using fiber placement.

APPENDIX A: MICHELL TRUSS STRUCTURES

a. Introduction

The goal of this research is to gain a competent understanding of Michell's theory for optimum truss layout. This began with a review of Michell's original paper published in 1904, a groundbreaking publication in the subject of structural optimization and layout theory. Michell's truss designs were exact solutions of least-volume truss structures. An example structure is created using an analytical solution to Michell's optimality criteria.

b. Analytical solution to the ground structure

Michell's theory states that for a given design domain, Ω , and a given set of external forces, a truss structure that satisfies Michell's optimality criteria will have a volume, V^* , which is less than or equal to any other truss design, V .

$$V^* \leq V \tag{a}$$

Michell's presented the criteria that must be satisfied for a layout to be considered optimized to its least-volume design. First, the stress constraint must be applied to all members of the framework such that:

$$-\sigma_C \leq \sigma \leq \sigma_T \tag{b}$$

Where σ_C and σ_T are the maximum permissible stresses in compression and tension respectfully. Through sizing optimization, it is assumed that all truss members will be stressed to the maximum permissible amount. Once all members are stressed to their maximum limits, the total truss volume can be expressed using the primal formula

presented by Maxwell (1864).

$$V^* = \sum_T \frac{l^T N^T}{\sigma_T} - \sum_C \frac{l^C N^C}{\sigma_C} \quad (c)$$

Where l is the length of the member and N is the internal force carried by the member. More importantly, the Michell optimality criteria states that if an infinitesimally small test deformation is applied, all members (tension and compression) should have a constant strain value, e .

$$\bar{\epsilon} = e \quad (d)$$

Where the sign of e is equal to the sign of the internal force of the member. These criteria can be satisfied two different ways. Solution one: all members are loaded in either tension or compression, such as a system of solely struts or ties. However, for a framework to support more complicate loads a structure would need to be a combination of both. If a framework of both tension and compression members is needed to carry the load, the members must meet at nodal locations with equal but opposite virtual strains. This is only satisfied if members meet orthogonally to each other along lines of lines of constant major and minor principle strain.

The greatest difficulty in designing Michell structures is determining a system of curves that define the lines of constant principle strain. Three approaches can be taken: analytical solutions, numerical solutions, and graphical solutions. Once the ground structure is defined, the structure is discretized into elements and a sizing optimization is performed on the cross-sectional areas to create a least-volume structure. These truss structures are all called Michell structures.

An example problem was performed using an analytical solution to Michell's

strain criteria. Assume a cantilever design domain that carries a concentrated bending load, as shown in Fig. A1.



Fig. A1 Design domain of a cantilever structure.

Assume a new curvilinear coordinate system defined as:

$$x = x(\alpha, \beta) \quad (e)$$

$$y = y(\alpha, \beta) \quad (f)$$

For a curvilinear plane stress element, the equation of compatibility of the first order of strain is (Hemp, 1958),

$$\begin{aligned} \frac{\partial}{\partial \alpha} \left(\frac{B}{A} \frac{\partial e_{\beta\beta}}{\partial \alpha} \right) + \frac{\partial}{\partial \beta} \left(\frac{A}{B} \frac{\partial e_{\alpha\alpha}}{\partial \beta} \right) - 2 \frac{\partial^2 e_{\alpha\beta}}{\partial \alpha \partial \beta} - \frac{\partial}{\partial \alpha} \left[\frac{1}{A} \frac{\partial B}{\partial \alpha} (e_{\alpha\alpha} - e_{\beta\beta}) \right] \\ + \frac{\partial}{\partial \beta} \left[\frac{1}{A} \frac{\partial A}{\partial \beta} (e_{\alpha\alpha} - e_{\beta\beta}) \right] - 2 \frac{\partial}{\partial \alpha} \left(\frac{1}{A} \frac{\partial A}{\partial B} e_{\alpha\beta} \right) - 2 \frac{\partial}{\partial \beta} \left(\frac{1}{B} \frac{\partial B}{\partial \alpha} e_{\alpha\beta} \right) \quad (g) \\ = 0 \end{aligned}$$

Where A and B are functions that are introduced that will satisfy the compatibility equation. By applying Michell's optimality criteria, the strains become,

$$e_{\alpha\alpha} = e \quad (\text{h})$$

$$e_{\beta\beta} = -e \quad (\text{i})$$

$$e_{\alpha\beta} = 0 \quad (\text{j})$$

This simplifies the compatibility equation to,

$$\frac{\partial}{\partial\alpha} \left(\frac{1}{A} \frac{\partial B}{\partial\alpha} \right) - \frac{\partial}{\partial\beta} \left(\frac{1}{B} \frac{\partial A}{\partial\beta} \right) = 0 \quad (\text{k})$$

Functions $A = A(\alpha, \beta)$ and $B = B(\alpha, \beta)$ must be selected to satisfy the previous equation. The design domain and the type of problem dictate the type of functions that must be used. Once a set of functions has been found, they must be transformed into curves in Cartesian coordinates. Many sets of functions can be found to satisfy the compatibility equation but few can be converted into the Cartesian (x, y) system of coordinates. Many authors have presented solutions to solve for the curves numerically. Following the work of (Ghista & Resnikoff, 1968), the functions of A and B are selected as,

$$A = 4 \cos(\alpha + \beta) \quad (\text{l})$$

$$B = 4 \sin(\alpha + \beta) \quad (\text{m})$$

Using the following relationships and identities,

$$\cos(\alpha + \beta) = \frac{1}{A} \frac{\partial x}{\partial \alpha} \quad (\text{n})$$

$$\sin(\alpha + \beta) = \frac{1}{A} \frac{\partial y}{\partial \alpha} \quad (\text{o})$$

$$\cos(\alpha + \beta) = \frac{1}{B} \frac{\partial x}{\partial \beta} \quad (\text{p})$$

$$\sin(\alpha + \beta) = \frac{1}{B} \frac{\partial y}{\partial \beta} \quad (\text{q})$$

The following two equations determine which denote lines of constant α and β .

They represent a field of principle strains that satisfy Michell's optimality criterion.

Every intersection of the two curves occurs orthogonally.

$$x = 4\alpha - \cos^{-1}(y) + \sqrt{1 - y^2} \quad (\text{r})$$

$$x = -4\beta + \cos^{-1}(-y) + \sqrt{1 - y^2} \quad (\text{s})$$

The following sets of curves (Fig. A2) can be generated and used as a ground structure by assuming the design domain is bounded by $\alpha = \frac{\pi}{4}$, $\beta = 0$, and $x = 0$.

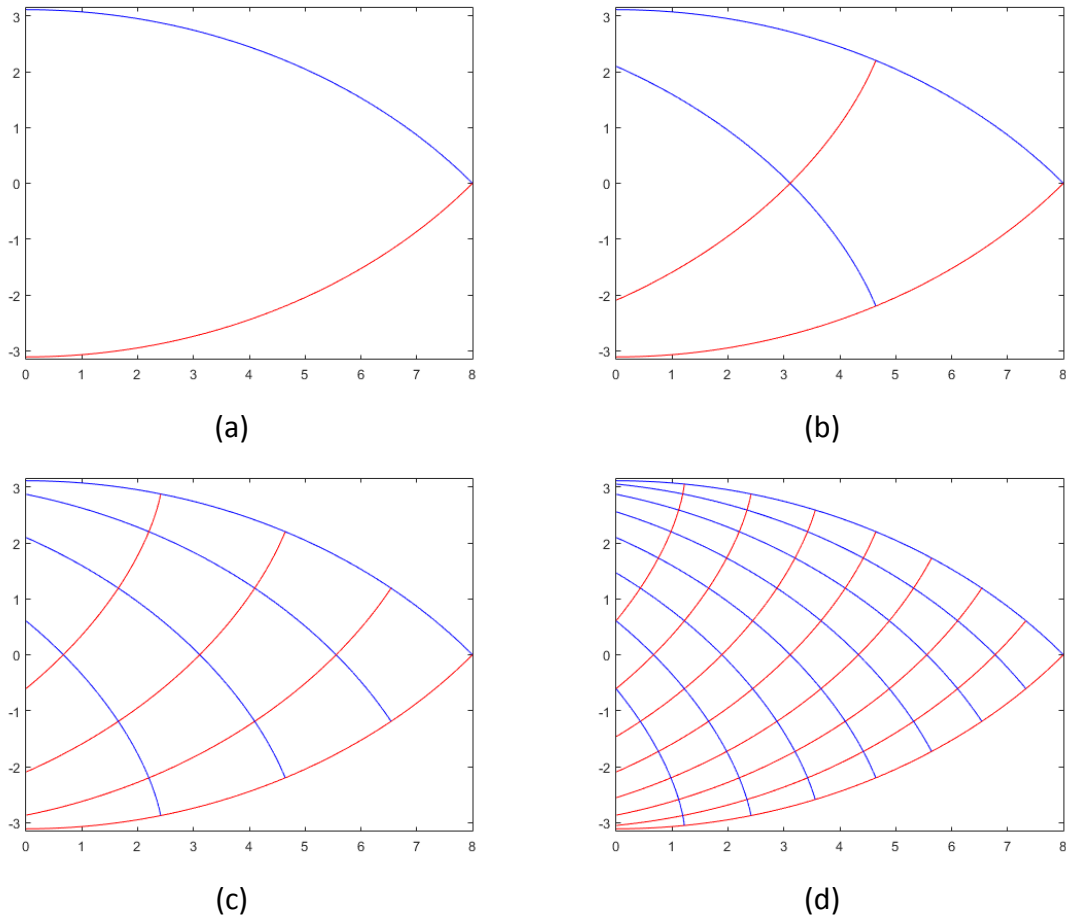


Fig. A2 Ground structures for a cantilever beam generated analytically using Michell's optimality criteria.

c. Structural solution and sizing optimization

The ground structure is discretized into individual bar elements. Nodes along the wall are pinned. A transverse load of 100 is applied at the tip. The maximum permissible stress in tension and compression is ± 100 . A code was written to perform the FEA and implement the sizing optimization of the individual elements. Fig. A3 shows the discretized structure and the resulting deformations. Fig. A4 shows the results of the sizing optimization such that every member is stressed to their maximum permissible

stress. Table A1 shows the percent change of the volume as the number of members is increased.

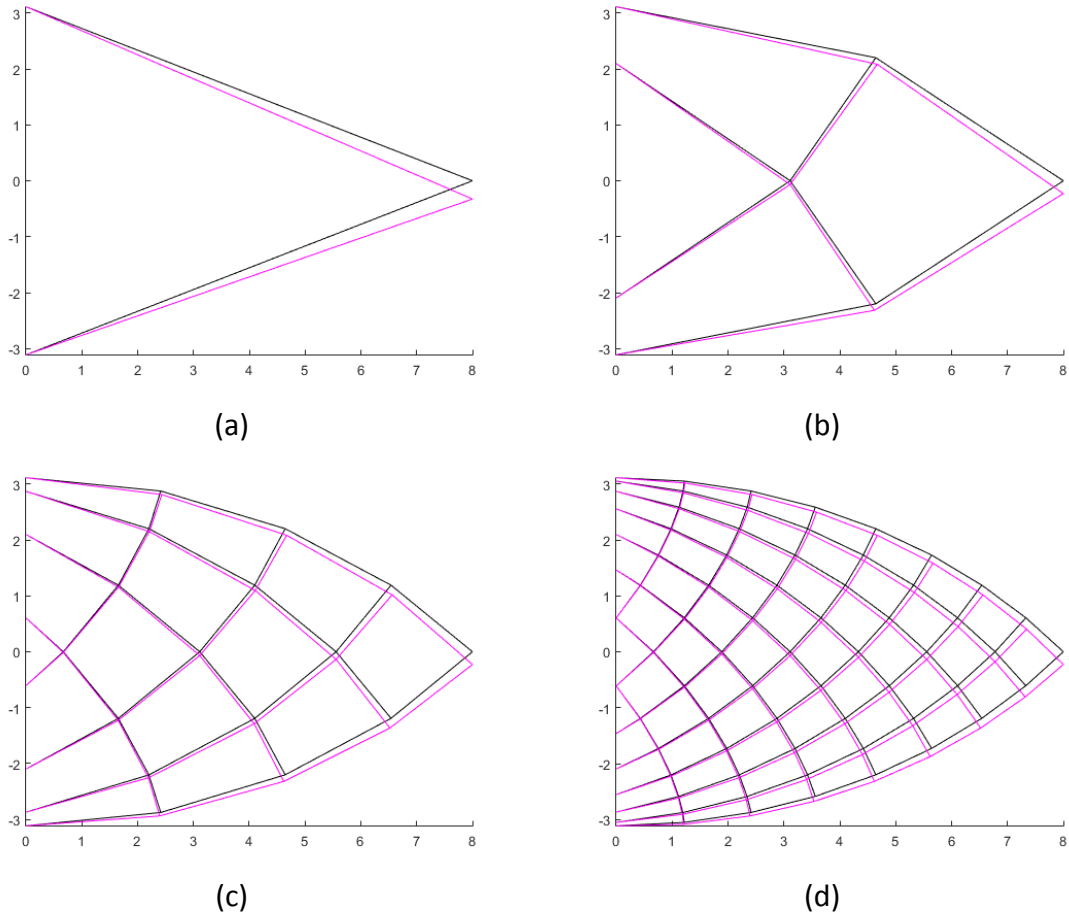


Fig. A3 FEA model of the ground structure (black) showing deflections (red) of the trusses after sizing optimization.

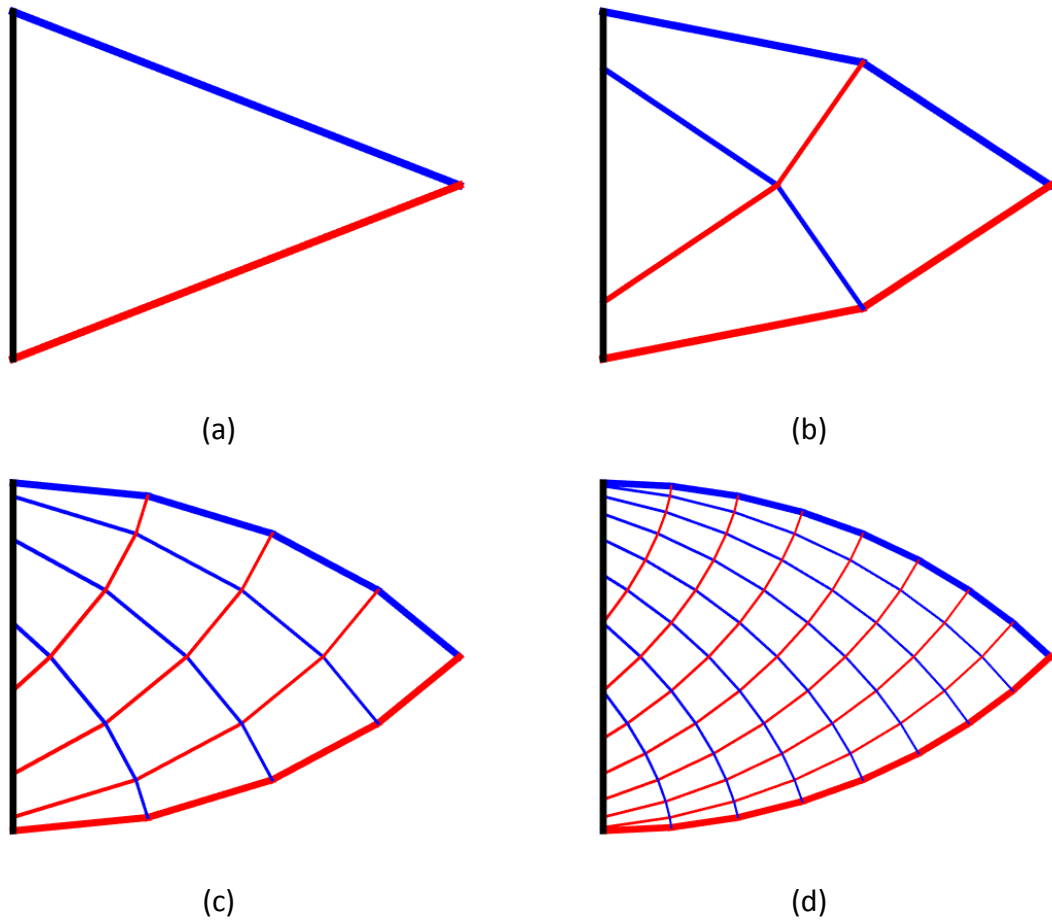


Fig. A4 Results of the sizing optimization.

Table A1 Comparison of primal volumes for each layout order.

Layout Order	V (primal formula)	% difference
1	23.67	
2	22.89	-3.29
4	22.83	-3.54
8	22.81	-3.63

Michell truss structures are characterized as truss-like continua because the structure is assumed to have an infinite amount of trusses. However, we can see in Table A1 that the primal volume is rapidly converging at an order 8 structure (64 truss

members), showing that increasing the number of members past 64 would have a minimal effect on dropping the primal volume of the structure.